

Manganese-based cathode materials for Li-ion batteries

Von der Fakultät Chemie der Universität Stuttgart
zur Erlangung der Würde eines Doktors der Naturwissenschaften
(Dr. rer. nat.) genehmigte Abhandlung

Vorgelegt von
Yuri Surace
aus Cinquefrondi (RC), Italien

Hauptberichter: Frau Professor Dr. Anke Weidenkaff
Mitberichter: Herr Professor Dr. Joachim Bill
Prüfungsausschussvorsitzender: Herr Professor Dr. Thomas Schleid

Tag der mündlichen Prüfung: 29.10.2015

Institut für Materialwissenschaft der Universität Stuttgart

2015

*Alla mia famiglia
Luigino, Maria Teresa e Luca*

Declaration

The work described in this thesis was carried out by the author in the Laboratory of Solid State Chemistry and Catalysis at Swiss Federal Laboratories for Materials Science and Technology (EMPA) in Dübendorf, under the supervision of Prof. Dr. Anke Weidenkaff from September 2012 to October 2015. The content is the original work of the author except where indicated otherwise and has not been previously submitted for any other degree or qualification at any academic institution.

Dübendorf, 07/08/2015

Yuri Surace

Erklärung

Die vorliegende Doktorarbeit wurde vom Autor selbst in der Abteilung Festkörperchemie und Katalyse an der Eidgenössische Materialprüfungs- und Forschungsanstalt (EMPA) in Dübendorf, unter der Leitung von Prof. Dr. Anke Weidenkaff im Zeitraum von September 2012 bis März 2013 angefertigt. Der Inhalt ist die eigene Arbeit des Autors, Ausnahmen sind gekennzeichnet, und wurde noch nicht zur Erlangung einer Qualifizierung oder eines Titels an einer akademischen Institution eingereicht.

Dübendorf, 07/08/2015

Yuri Surace

Contents

Acknowledgements	5
Abstract	6
Zusammenfassung	8
Sommario	10
Chapter 1	12
1. Introduction	12
1.1 Energy and batteries	12
1.2 Electrochemical cells and redox reactions	13
1.3 Definitions and concepts	17
1.4 Li-ion batteries	20
1.5 Components of Li-ion batteries	23
1.5.1 Cathode materials	23
1.5.2 Anode materials	27
1.5.3 Electrolyte	28
1.5.4 Current collector	30
1.5.5 Separator	30
1.6 Mn-based cathode materials	30
1.6.1 Advantages of Mn-based cathode materials	30
1.6.2 Crystal Field Theory (CFT) in Mn-based cathode materials	31
Chapter 2	35
2. Materials synthesis and characterization methods	35
2.1 Materials	35
2.1.1 Synthesis of μ -Ca ₂ MnO ₄ and n-Ca ₂ MnO ₄	35
2.1.2 Activation of μ -Ca ₂ MnO ₄ and n-Ca ₂ MnO ₄	36
2.1.3 Synthesis of SSR-Li ₃ MnO ₄ (solid state route)	36
2.1.4 Synthesis of FDR-Li ₃ MnO ₄ (freeze drying route)	37
2.1.5 Preparation of Li ₃ MnO ₄ cycled electrodes	37
2.1.6 Incorporation of vanadium in Li ₃ MnO ₄	37
2.1.7 Synthesis of FDR-LiMnBO ₃	38
2.1.8 Synthesis of FDR-LiMnBO ₃ /rGO	38
2.2 Physico-chemical characterization	39
2.2.1 X-ray diffraction (XRD)	39
2.2.2 Thermogravimetric analysis (TGA)	40
2.2.3 Scanning electron microscopy (SEM)	40
2.2.4 Transmission electron microscopy (TEM)	41
2.2.5 X-ray photoelectron spectroscopy (XPS)	41

2.2.6 Raman spectroscopy	42
2.2.7 Surface area determination	42
2.2.8 Particle size determination	42
2.3 Electrochemical characterization.....	43
2.3.1 The equipment used for electrochemical measurements	43
2.3.2 Electrode preparation	44
Chapter 3	45
3. Manganese in octahedral coordination: activation of Ca_2MnO_4 for Li intercalation	45
3.1 Introduction	45
3.2 Acid treatment of $\mu\text{-Ca}_2\text{MnO}_4$ and characterization.....	46
3.3 Acid treatment of $n\text{-Ca}_2\text{MnO}_4$: influence of the particle size and comparison with $\mu\text{-Ca}_2\text{MnO}_4$	58
Chapter 4	65
4. Manganese in tetrahedral coordination: Li_3MnO_4 as cathode material.	65
4.1 Introduction	65
4.2 Characterization of Li_3MnO_4 synthesized by FD	66
4.3 Capacity fading in Li_3MnO_4	79
4.4 Vanadium incorporation in Li_3MnO_4	89
Chapter 5	98
5. Manganese in square pyramidal coordination: $h\text{-LiMnBO}_3$	98
5.1 Introduction	98
5.2 FD synthesis of LiMnBO_3 and $\text{LiMnBO}_3/\text{rGO}$ composite	100
Concluding remarks	107
References	109
Additional declaration	115
Curriculum Vitae.....	116

Acknowledgements

At the end of this three-year long path, there are many people I would like to thank.

First of all, Prof. Dr. Anke Weidenkaff for accepting me as PhD student in her group, for her always creative ideas, and useful and constructive feedbacks.

Dr. Simone Pokrant for her guidance, supervision and trust in me during these years. She was a mentor for me regarding scientific and management issues.

Dr. Mario Simoes for his extremely helpful scientific support regarding electrochemistry and batteries.

Both Mario and Simone contributed to my personal and professional growth, making me become a better person and a better scientist.

Dr. James Eilertsen for his introduction concerning synthesis and XRD during the first months of my PhD and also for being a great advisor with the English language.

Dr. Lassi Karvonen for the very interesting discussions about solid state chemistry and his support with TGA measurements.

Dr. Songhak Yoon for the help with XRD and Dr. Santhosh Matam for the introduction in Raman Spectroscopy.

Mr. Matthias Trottmann and Mr. Oliver Brunko for solving all technical issues in an excellent manner.

Ms. Stephanie Looser for her always present administrative contribution.

I would like to thank all old members of the Solid State Chemistry and Catalysis Lab and all new members of the Laboratory Materials for Energy Conversion.

Dr. Ulrich Muller and Dr. Roland Hauert for the introduction and the assistance in XPS measurements.

Dr. Cedric Pitteloud, Dr. Yoann Mettan and Dr. Jose Antonio Gonzalez Martinez from Beleunos Clean Holding for the financial contribution and the wise advices regarding battery materials during the FAMSADI meetings.

Prof. Dr. Joachim Bill for taking on the task of co-examiner and Prof. Dr. Thomas Schleid for being the Chairman of the examination committee.

My girlfriend Monica for the precious chemistry-related advices, and her every day love.

In the end, my deepest thanks go to my family, who supported me with enthusiasm, happiness and love to whom I dedicate this thesis.

Abstract

Li-ion batteries are one of the most commercialized solutions to store electrochemical energy, but until now their broad use is limited to small electronic devices. Higher specific energy and longer cycle life are needed to open the way to a broader range of applications (i.e. electric vehicles or stationary batteries). The specific energy of Li-ion batteries is a function of the anode and cathode capacity for lithium intercalation and the cell voltage. However, capacity and voltage of current state-of-the-art cathode materials are the main specific energy-limiting factors of Li-ion batteries. For this reason, much of the attention during the past few years focused on cathode materials with either high voltage or high capacity or in the best of all cases both, coupled with high stability.

Manganese is one of the most common transition metals used in battery materials due to its multiple (and at least partially accessible) oxidation states, its low toxicity and its high availability. Mn-based cathode materials benefit from the $\text{Mn}^{3+}/\text{Mn}^{2+}$ or $\text{Mn}^{4+}/\text{Mn}^{3+}$ redox couples which allow obtaining a potential range between 3.0 V and 4.2 V vs Li^+/Li depending on the crystal structure and the chemical composition.

The aim of this work was to study unexplored and scarcely explored Mn-based cathode materials and to improve their electrochemical performances through structural, morphological and chemical modifications.

In the initial part of the thesis, a study of calcium manganite Ruddlesden-Popper phases Ca_2MnO_4 was carried out. Although the pristine material was not electrochemically active, Ca_2MnO_4 was activated for Li intercalation by Ca extraction using a novel and simple treatment with sulphuric acid. The influence of the amount of Ca extracted, and of the particle size were studied and correlated with the electrochemical properties. It was proposed that the acid treated materials had a bi-functional crystalline-amorphous structure, composed by a Ca_2MnO_4 crystalline bulk phase for the stability and an amorphous $\text{MnO}_2 \cdot x\text{H}_2\text{O}$ surface for the electrochemical response. For each 25at% of calcium extracted, capacities of 40 Ah/kg and 55Ah/kg were obtained for micron-sized particles and for nano-sized particles, respectively. A stability improvement of a factor of 10 was reached in comparison to bare amorphous hydrated manganese oxide.

The work focused then on Li_3MnO_4 , a lithium rich phase containing manganese (V). Developing a novel freeze drying (FD) synthesis-route, the micro- and nanostructure of the material

were modified with relevant consequences on the electrochemical properties. Smaller particles size in conjunction with smaller grains size allowed obtaining a first discharge capacity of 290 Ah/kg with an improvement of up to 31%, in comparison to Li_3MnO_4 synthesized by the solid state route. Moreover, measurements carried out at different cycling rates showed improvements in rate capability. In addition, this new route allowed reducing the reaction temperature and time. However, considerable modifications in the Li_3MnO_4 structure occurred during the first cycle and the capacity improvement vanished after a few cycles due to structural instability of this material under cycling. To gain deeper insight into the reason of the capacity fading of this material, a post mortem analysis was carried out which allowed to create a model for the degradation mechanism. Briefly, the lithium extraction or insertion in the structure caused the amorphization of the material with conversion to the more stable amorphous manganese oxide.

In the last part of this thesis, preliminary studies on lithium manganese borate LiMnBO_3 were carried out. It was shown in a proof of concept study that the FD synthesis was applicable for this material as well. Nanocrystalline material was obtained with electrochemical performance comparable to the state of the art by gaining in synthesis simplicity.

Zusammenfassung

Li-Ionen Batterien sind die am stärksten kommerzialisierte Lösung zur Energiespeicherung. Aber bis heute ist ihr flächendeckender Einsatz auf kleine elektronische Geräte beschränkt. Höhere spezifische Energien und länger Lebenszeiten sind nötig, um den Weg für eine breitere Anwendungspalette zu öffnen, wie zum Beispiel elektrische Fahrzeuge oder stationäre Energiespeicher. Die spezifische Energie von Li-Ionen Batterien ist eine Funktion der Anoden- und Kathodenkapazität für Li-Interkalation und der Zellspannung. Insbesondere die Kapazität und die Spannung von dem heutigen Stand der Technik entsprechenden Kathodenmaterialien begrenzen die spezifische Energie von Li-Ionen Batterien. Aus diesem Grund wurde in den letzten Jahren verstärkt nach Kathodenmaterialien geforscht, die entweder hohe Spannungen oder hohe Kapazitäten oder am besten beides besitzen, gekoppelt mit hoher Stabilität. Mangan ist eines der häufigsten Übergangmetalle, das in Batterien benutzt wird wegen seiner multiplen und zumindest teilweise zugänglichen Oxidationszustände, seiner niedrigen Giftigkeit und seines hohen Vorkommens. Mn-haltige Kathoden profitieren von $\text{Mn}^{3+}/\text{Mn}^{2+}$ oder $\text{Mn}^{4+}/\text{Mn}^{3+}$ Redoxpaaren, die es erlauben, Zellspannungen zwischen 3.0 V und 4.2 V gegen Li^+/Li zu erhalten, abhängig von der Kristallstruktur und der chemischen Verbindung.

Das Ziel dieser Arbeit war es, nicht oder nur wenig erforschte Mn-haltige Kathodenmaterialien zu untersuchen und ihre elektrochemische Leistung durch strukturelle, morphologische und chemische Modifikationen zu verbessern.

Im Anfangsteil dieser Doktorarbeit wurde eine Untersuchung an der Ruddlesden-Popper Phase Ca_2MnO_4 durchgeführt. Obwohl das reine Material nicht elektrochemisch aktiv ist, konnte Ca_2MnO_4 durch die Extraktion von Ca für die Li-Interkalation aktiviert werden mit Hilfe einer neuartigen und einfachen Behandlung mit verdünnter Schwefelsäure. Die elektrochemischen Eigenschaften wurden in Abhängigkeit von der extrahierten Kalziummenge und der Teilchengröße untersucht. Darauf aufbauend wurde ein Modell entwickelt, nämlich dass die säurebehandelten Materialien eine bifunktionale kristallin-amorphe Struktur besitzen, die aus einem kristallinen Ca_2MnO_4 haltigen Festkörperkern bestehen zur Stabilisierung und aus amorphen $\text{MnO}_2 \cdot x\text{H}_2\text{O}$ Oberflächen, die für die elektrochemische Funktionalität zuständig sind. Für jeweils 25% extrahiertem Ca wurden einerseits Kapazitäten von 40 Ah/kg für mikrometergrosse und andererseits 55 Ah/kg für nanometergrosse Teilchen gemessen. Eine Stabilitätsverbesserung um einen Faktor 10 wurde erreicht im Vergleich zu amorphen hydrierten Manganoxid.

Die Arbeit konzentrierte sich dann auf Li_3MnO_4 , eine Li-reiche Phase, die Mn (V) enthält. Indem eine neuartige Syntheseroute über Gefriertrocknen entwickelt wurde, konnte sowohl die Mikro- als auch die Nanostruktur des Materials modifiziert werden mit relevanten Konsequenzen für die elektrochemischen Eigenschaften. Kleinere Partikelgrößen kombiniert mit kleineren Kristallitgrößen erlaubten es, Kapazitäten von 290 Ah/kg für die erste Entladung zu erhalten, was einer Verbesserung von bis zu 31% im Vergleich zu Li_3MnO_4 synthetisiert über traditionelle festkörperchemische Methoden entspricht. Darüber hinaus zeigten Messungen bei verschiedenen Ladegeschwindigkeiten eine Verbesserung in der Geschwindigkeitsfähigkeit. Zusätzlich erlaubte die neue Syntheseroute die Reaktionstemperatur und die Reaktionszeit zu verringern. Allerdings fanden gewichtige Modifikationen der Li_3MnO_4 Struktur während des ersten Zyklus statt und die Verbesserung in der Kapazität verschwand nach einigen Ladungs-/Entladungszyklen wegen der strukturellen Instabilität dieses Materials unter Belastung. Um den Grund für den Kapazitätsschwund dieses Materials zu verstehen, wurde eine Post-Mortem Studie durchgeführt, die es erlaubte ein Model für den Degradationsmechanismus zu entwickeln. Die Li-Extraktion oder Insertion führte zu einer Amorphisierung des Materials mit einer Umwandlung zum stabileren amorphen Manganoxid.

Im letzten Teil dieser Doktorarbeit wurde eine vorläufige Studie an LiMnBO_3 durchgeführt. Es wurde gezeigt, dass die Syntheseroute via Gefriertrocknen auch für dieses Material anwendbar ist. Es konnte dadurch nanokristallines Material erhalten werden, das in seinen elektrochemischen Eigenschaften vergleichbar zum Stand der Forschung ist bei einem gleichzeitigen Gewinn an Einfachheit in der Synthese.

Sommario

Le batterie agli ioni di litio costituiscono una delle principali soluzioni presenti in commercio per immagazzinare energia elettrochimica e finora il loro uso è stato limitato a piccoli apparecchi elettronici. Per il loro utilizzo in una più vasta gamma di applicazioni (es. veicoli elettrici o batterie stazionarie) sono necessari una maggiore energia specifica e un ciclo di vita più lungo. L'energia specifica dipende dalla capacità del catodo e dell'anodo d'intercalare ioni litio e dal voltaggio della cella. Tuttavia, allo stato dell'arte, essa è limitata dalla capacità e dal voltaggio dei materiali catodici. Per questo motivo, negli ultimi anni si è posta molta attenzione sui materiali catodici che abbiano sia un alto voltaggio che un'alta capacità, o nel migliore dei casi entrambi, in congiunzione con una maggiore stabilità.

Il manganese è uno metalli di transizione più comunemente usato nei materiali per batterie a causa dei suoi multipli (e parzialmente accessibili) stati di ossidazione, la sua bassa tossicità e l'alta accessibilità. Materiali catodici basati sul manganese beneficiano delle coppie redox $\text{Mn}^{3+}/\text{Mn}^{2+}$ or $\text{Mn}^{4+}/\text{Mn}^{3+}$ originando un voltaggio fra 3.0 V e 4.2 V vs Li^+/Li , il quale dipende a sua volta dalla struttura cristallina e dalla composizione chimica del materiale.

Lo scopo di questo lavoro è stato quello di studiare dei materiali catodici sconosciuti o poco conosciuti basati sul manganese e migliorare le loro prestazioni elettrochimiche attraverso delle modifiche strutturali, morfologiche e chimiche.

Nella parte iniziale di questa tesi è stato effettuato uno studio sul Ruddlesden-Popper calcio manganite Ca_2MnO_4 . Nonostante il materiale di partenza non fosse elettrochimicamente attivo, Ca_2MnO_4 è stato attivato per intercalare ioni litio attraverso l'estrazione di calcio usando un nuovo e semplice trattamento con acido solforico. E' stata studiata quindi l'influenza della quantità di calcio estratta e della dimensione delle particelle e la loro correlazione con le proprietà elettrochimiche. E' stato proposto che i materiali trattati con l'acido abbiano una struttura bi-funzionale cristallina-amorfa, in cui il bulk è composto da Ca_2MnO_4 cristallino per migliorare la stabilità e la superficie è composta da $\text{MnO}_2 \cdot x\text{H}_2\text{O}$ amorfo il quale dà origine alla risposta elettrochimica. Per ogni 25 at% di calcio estratto, sono state ottenute capacità di 40 Ah/kg e 55 Ah/kg per particelle di dimensioni micrometriche e nanometriche, rispettivamente. Un miglioramento della stabilità di un fattore 10 è stato raggiunto in confronto con il materiale composto da solo ossido di manganese idrato amorfo.

Lo studio si è concentrato quindi su Li_3MnO_4 , una fase ricca in litio e contenente manganese nello stato di ossidazione (V). Attraverso lo sviluppo di una nuova strategia di sintesi basata

sul freeze-drying (FD), sono state modificate la micro- e nanostruttura del materiale con importanti conseguenze sulle proprietà elettrochimiche. Particelle di dimensioni minori in congiunzione con una minore dimensione dei cristalliti ha permesso di ottenere una capacità durante la prima scarica di 290 Ah/kg con un miglioramento del 31 % in confronto con Li_3MnO_4 sintetizzato attraverso una reazione in stato solido. Una maggiore capacità è stata anche registrata testando il materiale a differenti velocità di ciclaggio. Inoltre, questa nuova strategia di sintesi ha permesso di ridurre la temperatura e il tempo di reazione. Tuttavia, la struttura di Li_3MnO_4 subisce notevoli modifiche durante il primo ciclo e il miglioramento sparisce dopo alcuni cicli a causa dell'instabilità strutturale del materiale durante il ciclaggio. Per capire la causa della diminuzione della capacità di questo materiale è stata effettuata un'analisi *post-mortem* che ha permesso di creare un modello per il meccanismo di degradazione. Brevemente, l'inserzione e la de-inserzione di ioni litio nella struttura causano un'amorfizzazione del materiale ed esso converte nel più stabile ossido di manganese amorfo.

Nella parte finale della tesi, sono stati effettuati degli studi preliminari su litio manganese borato LiMnBO_3 . E' stato dimostrato che la sintesi via FD può essere utilizzata anche per questo materiale. E' stato ottenuto un materiale nanocristallino con delle performance elettrochimiche confrontabili con lo stato dell'arte e, al tempo stesso, guadagnando anche in semplicità di sintesi.

Chapter 1

1. Introduction

1.1 Energy and batteries

Nearly all developed countries depend on fossil fuels (coal, oil, natural gas) as a primary energy source. Heavy consumption of these limited resources, mainly for electrical-energy production and transportation, produces greenhouse gas emissions that lead to global climate change. Therefore, it is imperative that alternative, renewable and sustainable energy technologies must be further developed in order to reduce the dependence on fossil fuels and decrease greenhouse gas emissions [1].

In the last few years, the steady increase in the global energy demand triggered a considerable progress in several renewable energy technologies as solar energy, wind power, biofuels and hydropower. This resulted in a growth of the total renewable power capacity by a factor of 7 (the most significant has been in photovoltaics by a factor of 70). By 2013, 19% of the world's final energy consumption was supplied by renewables sources [2].

However, renewable energies production is not demand-oriented and variable over time. Therefore stationary energy storage solutions are needed as essential components to guarantee the reliability of future energy systems [3]. Batteries are the most discussed component of stationary applications. Indeed, electrical energy needs to be stored in batteries during times when production exceeds the consumption, and batteries have to supply electrical energy when consumption exceeds the production. In this way the electricity production could be maintained at more constant levels and the cost could be lower [4].

Another field of interest where batteries play a primary role is mobility. A contribution to a greener world can be obtained only if vehicles driven by internal combustion engines (ICEs) are phased-out. An alternative are electric vehicles (EV) powered by batteries. The progress which has been made during the last decade lowered the battery cost. In parallel the infrastructure dedicated to electric vehicles (EVs) was increased. This is expected to result in an

83% increase of EVs sale in the next 10 years [5] with a positive impact on the global environment.

In addition, batteries are also extremely important in everyday life since they are one of the most commercialized power sources for portable applications such as mobile phones, laptops, etc.

For all the above mentioned applications batteries are the key factor. Higher gravimetric energy, higher volumetric energy and longer cycle life are compulsory to go beyond the state of the art. This would open the way for the conception of new energy technologies and the development of the existing one with their wide-spreading all over the world. For example, more efficient energy storage solutions would allow using the full potential of renewable energy sources and they could enable countries to run on 100% renewable energy in the next future [6]. Consequently, this thesis was focused on the study of materials for battery applications.

1.2 Electrochemical cells and redox reactions

An electrochemical cell is a device capable of producing electrical energy from spontaneous chemical reactions or inducing non-spontaneous chemical reactions through the consumption of electrical energy. In the first case the cell is called *galvanic cell* and in the second case *electrolytic cell* [7].

An electrochemical cell consists of two electrodes immersed in an electrolyte solution. The electrodes are electronic conductors, while the electrolyte solution is an ionic conductor. At the interface between electrodes and electrolyte occurs an oxidation-reduction reaction (*redox* reaction) which produces electrical current. The electrode where the oxidation occurs is called anode. The electrode where the reduction occurs is called cathode.

A *redox* reaction is a chemical reaction which involves the transfer of electrons between chemical species. The species involved in a redox reaction have to be able to change their oxidation states. In a common reaction two species are usually involved: the reductant (or reducing agent) and the oxidant (or oxidizing agent). The reductant transfers electrons to the oxidant. Thus, during the reaction, the reductant or *reducing agent* loses electrons and is oxidized (increasing its oxidation number), and the oxidant or *oxidizing agent* gains electrons and is reduced (decreasing its oxidation number). Redox reaction of a specific element are expressed as half reaction and, by convention, listed as reductions. A reduced and an oxidized species of

a specific element form a **redox couple** (Table 1). Each of these half-reactions can be associated with a *standard electrode potential*, E^0 . However, since half-reaction potentials cannot be measured in an absolute sense, every half reaction has to be coupled with a standard reference electrode. The standard hydrogen electrode (SHE) is used as reference electrode and its potential is set to 0.0 V. The SHE electrode is constituted of a platinated platinum electrode flushed with hydrogen in a 1 mol/l HCl water solution ($T = 25\text{ }^\circ\text{C}$, $p = 1\text{ bar}$, all active species at unity activity) [8].

Table 1: Standard electrode potential for some redox couples.

Half-reaction	Redox couple	Standard Electrode Potential (V) vs SHE
$\text{Cu}^{2+} + 2\text{e}^- \leftrightarrow \text{Cu}$	Cu^{2+}/Cu	0.52
$2\text{H}^+ + 2\text{e}^- \leftrightarrow \text{H}_2$	H^+/H_2	0.0
$\text{Zn}^{2+} + 2\text{e}^- \leftrightarrow \text{Zn}$	Zn^{2+}/Zn	-0.76
$\text{Mn}^{2+} + 2\text{e}^- \leftrightarrow \text{Mn}$	Mn^{2+}/Mn	-1.18
$\text{Al}^{3+} + 3\text{e}^- \leftrightarrow \text{Al}$	Al^{3+}/Al	-1.66
$\text{Na}^+ + \text{e}^- \leftrightarrow \text{Na}$	Na^+/Na	-2.71
$\text{Li}^+ + \text{e}^- \leftrightarrow \text{Li}$	Li^+/Li	-3.04

For non-standard conditions the Nernst equation is used to determine the potential of the half-reaction at equilibrium [8] Eq.1.1:

$$E = E^0 + \frac{RT}{nF} \ln \prod_i a_i^{v_i} \quad \text{Eq. 1.1}$$

Where:

E : electrode potential [V]

E^0 : Standard electrode potential [V]

R : ideal gas constant [$\text{J K}^{-1} \text{mol}^{-1}$]

T : absolute temperature [K]

n : number of electron exchanged

F : Faraday constant [C mol^{-1}]

a_i : activity of species i

v_i : stoichiometric coefficient species i .

The cell voltage of an electrochemical cell is calculated from the electrode potentials (reduction potentials) of the half-reactions. The overall theoretical cell voltage ΔE of an electrochemical cell is obtained by the difference between the half-cell potential of the reduction (cathode) and the half-cell potential of the oxidation (anode):

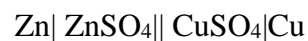
$$\Delta E = E^{\text{red}} - E^{\text{ox}} = E^{\text{cat}} - E^{\text{an}} \quad \text{Eq. 1.2}$$

The first example of galvanic cell was the “Volta cell”. The electrodes were made of a Zn metal piece and a Cu metal piece immersed in an electrolyte solution of sulphuric acid which can be represented as follow:

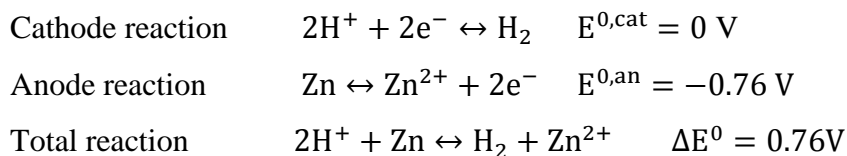


By convention each interface is represented by a vertical stroke and if the electrochemical chain includes several successive electrolyte media, then the abbreviated notation $||$ is often used to denote the separation zone between two electrolytes.

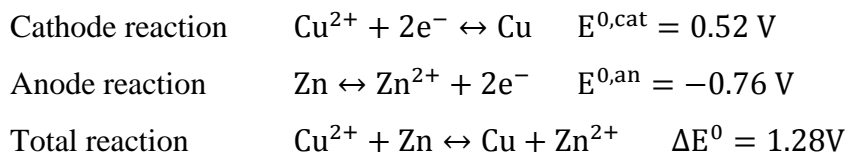
Another simple example of galvanic cell is the “Daniel Cell”. It includes two compartments containing respectively a ZnSO_4 aqueous solution in contact with zinc metal and a CuSO_4 aqueous solution in contact with copper metal. These two compartments are electrically connected by a third aqueous solution, e.g., a concentrated KNO_3 solution, which is called a salt bridge.



In the case of the Volta cell the reactions are:



In the case of Daniel cell the reactions are:

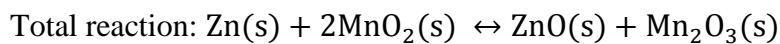
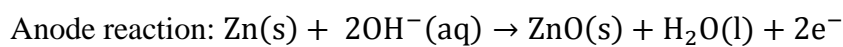
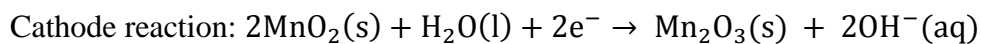


Nowadays, galvanic cells, more commonly called batteries, are divided in primary batteries and secondary batteries. Primary batteries are based on irreversible electrochemical reactions; they produce energy for a limited period of time and after discharge they have to be disposed

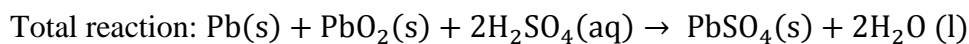
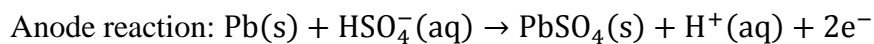
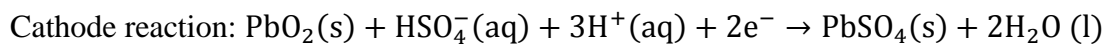
(e.g. Alkaline). Secondary batteries are based on reversible electrochemical reactions and they can be recharged, converting electrical energy in chemical energy during the charge process (e.g. Lead-acid, Ni-Cd, Li-ion) [7].

Since the discovery of the “Volta cell”, batteries based on different chemistries have been developed over the years (Fig.1). The most common commercial batteries with their voltage, specific energy and redox reaction are listed below, and a comparison of the volumetric and specific energy is shown also in Fig.1.1:

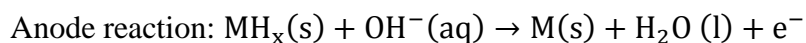
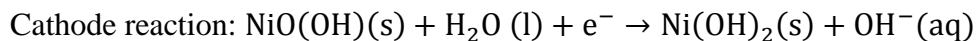
Alkaline (1.4 V, 120 Wh/kg)



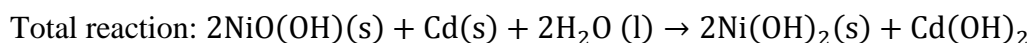
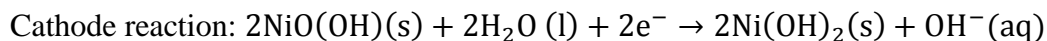
Lead-Acid (2.0 V, 40 Wh/kg)



Ni-MH (1.2 V – 100 Wh/kg)



Ni-Cd (1.2 V – 60 Wh/kg)



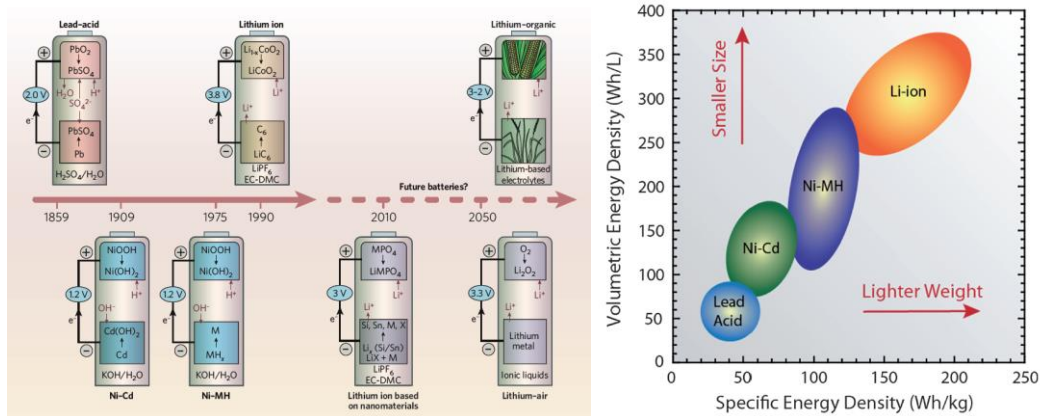


Figure 1.1: Battery chemistry over the years (left) [9] and comparison between different batteries technologies (right) [10]

1.3 Definitions and concepts

The performances of an electrochemical cell are expressed using theoretical values or practical values. Theoretical values are calculated from the thermodynamics of the electrochemical cell reaction and are thus independent of a particular cell design. Practical values are related to the total mass of the full battery, including the mass of electrodes, electrolyte, separator, current collectors, terminals and cell housing. They depend strongly on the cell design and on the conditions of discharge [11]. In Li-ion batteries, electrodes are usually composites made of electroactive material (EAM), carbon and binder, therefore the redox reaction involves only the EAM which act as reactant. In this work, the specific charge always refers to the weight of the EAM only.

Cell voltage

The cell voltage can be calculated from the Gibbs free energy of the corresponding chemical reaction:

$$U^0 = \Delta E^0 = \frac{-\Delta G^0}{nF} \quad \text{Eq. 1.3}$$

where:

ΔE^0 : Standard cell potential

ΔG^0 : Standard Gibbs Free Energy

n: number of electron exchanged

F: Faraday constant

Current density

The current density j is calculated by dividing the total current I flowing through an electrode by the electrode area A . The normal case is that the geometrical area is used:

$$j = \frac{I}{A} \quad \left[\frac{\text{A}}{\text{m}^2} \right] \quad \text{Eq. 1.4}$$

Capacity

The capacity Q is the total amount of charge obtainable from a cell:

$$Q = \int_{t_1}^{t_2} I \cdot dt \quad [\text{A} \cdot \text{h}] \quad \text{Eq. 1.5}$$

Theoretical Specific Charge

The theoretical specific charge, q_{th} , is the amount of charge per kg of reactant. It is usually based on the molecular weight of the active materials and the number of electrons transferred in the electrochemical process [12]. It can be calculated via Faraday's law.

$$q_{\text{th}} = \frac{nF \cdot 1000}{W \cdot 3600} \quad \left[\frac{\text{A} \cdot \text{h}}{\text{kg}} \right] \quad \text{Eq.1.6}$$

Where:

n : number of electron exchanged

F : Faraday constant 96485.34 [C mol⁻¹]

W : molecular weight of the substance [mol g⁻¹]

Very often in the battery community this quantity is called also capacity.

Practical specific charge

The (practical) specific charge is the total charge obtainable under specified discharge conditions from a practical cell in one discharge cycle divided by the total mass of the cell (m_c).

$$q = \left| \frac{Q}{m_c} \right| \quad \left[\frac{\text{A} \cdot \text{h}}{\text{kg}} \right] \quad \text{Eq.1.7}$$

Theoretical and practical charge density

The theoretical charge density ($Q_{V,th}$) is the amount of charge divided by the volume of the reactant. The practical charge density (Q_V) represents the total charge obtainable from a practical cell divided by the volume of the cell. The unit measure is very often Ah/l.

Theoretical specific energy

The theoretical specific energy, w_{th} , can be calculated from the Gibbs energy change ΔG^0 of the electrochemical cell reaction divided by the sum of the stoichiometric masses of the reactants (m_R).

$$w_{th} = \left| \frac{\Delta G^0}{\sum_i m_{R,i}} \right| = \frac{nF\Delta E^0}{\sum_i m_{R,i}} \quad \left[\frac{W \cdot h}{kg} \right] \quad \text{Eq. 1.8}$$

Practical specific energy

The (practical) specific energy is the total electrical energy (W_c) obtainable from a practical cell in one discharge cycle divided by the mass of the respective cell (m_c).

$$w = \frac{W_c}{m_c} \quad \text{where } W_c = \int_0^t U(t)I(t)dt \quad \left[\frac{W \cdot h}{kg} \right] \quad \text{Eq. 1.9}$$

Theoretical and practical energy density

The theoretical energy density, $W_{V,th}$, can be calculated from the Gibbs energy change ΔG^0 of the electrochemical cell reaction divided by the sum of the volumes of the reactants.

The practical energy density, W_V , is the total electrical energy obtainable from a practical cell under specified discharge conditions divided by the volume of the cell. The unit measure is Wh/l.

Specific power

The specific power is the capability to deliver power per mass of a primary or secondary battery. The specific power of a cell depends on the discharge current and decreases during discharge. The unit measure is W/kg.

Power density

The power density is the power divided by the volume of the cell. The unit measure is W/l.

Coulombic efficiency

For secondary cells, the Coulombic efficiency (CE) represents the ratio of charge released during the discharge Q_{dis} to the charge necessary for charging the battery Q_{ch} .

$$\Phi_Q = \frac{Q_{\text{dis}}}{Q_{\text{ch}}} \quad \text{Eq. 1.10}$$

Both Q_{dis} and Q_{ch} are obtained by integrating the respective currents over the charging and discharging time, respectively. They depend on the conditions for charging and discharge.

Values of CE lower than 100% are directly related to an irreversible capacity as results of side reactions inside the cell.

In scientific literature on batteries, one frequently encounters the term C-rate, which describes the current required to charge or discharge a cell in 1h. Using twice the amount of currents (i.e., at 2C-rate) the cell is completely charged or discharged in half an hour. The amount of current at certain C-rate is closely related to the specific charge of the material. For example, for a material with 200Ah/kg theoretical specific charge, 1C would mean to charge or discharge the material at 200A/kg [12].

1.4 Li-ion batteries

The need for batteries with higher specific and volumetric energy boosted the development of new battery technologies like lithium ion batteries.

The use of lithium in a battery seemed very attractive because lithium is the lightest metal on earth (m.w. = 6.941 g mol⁻¹, density = 0.534 g/cm³, $q_{\text{th}}=3861$ Ah/kg) and it has also the lowest absolute electrochemical potential ($E^0 = -3.04$ V vs. SHE). The first paper on metallic lithium as electrode was reported by Lewis in 1913 [13] but it is only in the early 70s that primary Li-ion batteries were introduced into the market. These batteries were based on lithium metal anode and manganese dioxide (MnO₂), sulfur dioxide SO₂, or polycarbon monofluoride ((CF_x)_n) as cathodes in an organic electrolyte as propylene carbonate [14].

However, issues regarding the stability of metallic lithium in organic electrolyte became soon evident. Due to its high reducing power, lithium decomposes the electrolyte creating a film

made of electrolyte decomposition products on the surface of the electrode [15]. If, on one side, the formation of this film, called solid electrolyte interface (SEI), can give rise to some advantages, since it is permeable to Li ions and prevents lithium to further corrode; on the other side lithium deposition and dissolution can give rise to dendrite formation [16] (Fig.1.2a).

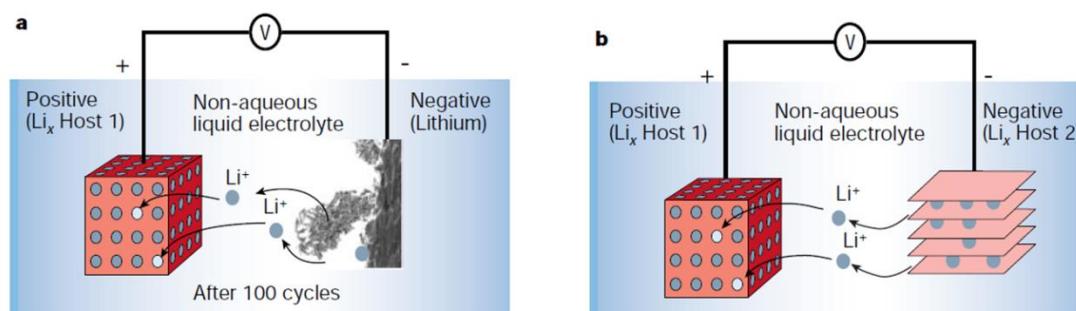


Figure 1.2: (a) Rechargeable Li-metal battery with lithium metal anode and (b) rechargeable Li-ion battery with intercalation cathode. [17]

The growing of dendrites becomes a problem, when they perforate the separator placed between anode and cathode, shortcircuiting the cell. Then all stored energy of the cell is instantaneously transformed into heat. Explosions and fires are possible, due to the low melting point (ca. 180°C) and the high reactivity of lithium [14].

For these safety reasons, in the early 80s lithium intercalation materials with an electrochemical potential close to that of Li were proposed as anode for lithium-ion batteries (Fig.1.2b). The development of such low-voltage intercalation materials was successful. A well-known example is lithiated graphite Li_xC₆ [18, 19]. In the same time period, the “intercalation” concept was also applied to cathode materials. Layered di- and trichalcogenides first, and layered transition metal oxides [20] later, were largely studied as positive electrodes.

This new system, the so called “rocking chair system” [21], because lithium ions travel back and forth between cathode and anode intercalation materials, set the foundation to today’s Li-ion commercial batteries.

The term “lithium-ion cell” refers to the working mechanism based on the highly reversible electrochemical reaction, usually called a “lithium insertion” or “lithium intercalation” process, which may be described as the insertion/extraction of mobile lithium ions into a host structure (Fig.1.3).

The basic setup of a Li-ion battery is composed of three main components: a positive electrode, a negative electrode and an organic electrolyte between them assuring Li^+ conductivity (not electronic conductor). The positive and negative electrodes are referred to as the cathode and anode during discharge, and vice versa during charge. During the discharge process lithium ions are extracted from the anode which is oxidized and inserted in the cathode which is reduced. The process is reversed during the charge [22].

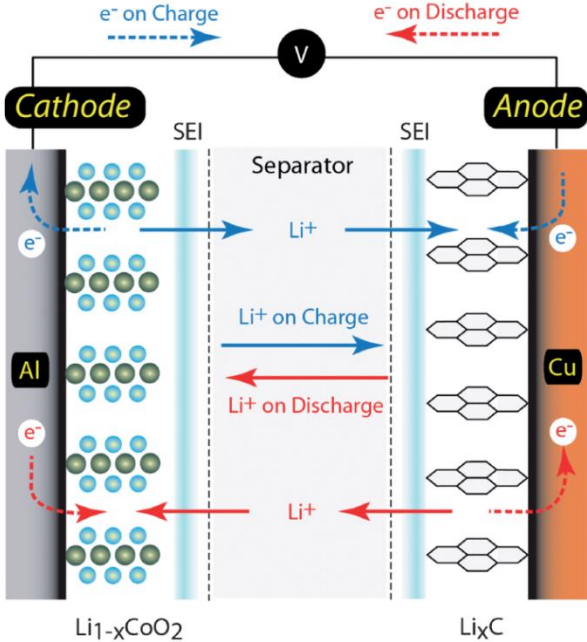
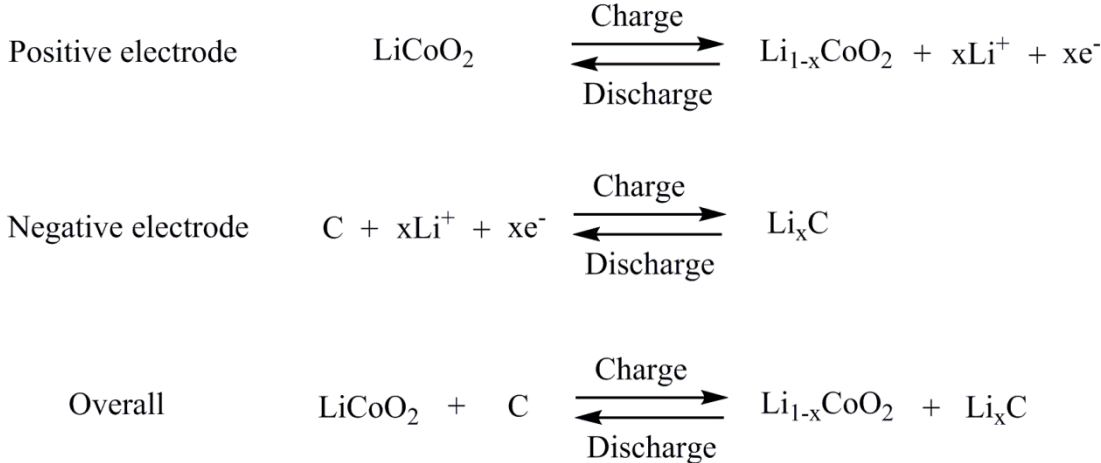


Figure 1.3: Schematic representation of a Li-ion battery during charge/discharge. The right side shows the graphite sheets and the left side the layered structure of LiCoO_2 [10].

The charging/discharging process for a Li-ion battery with lithium cobalt oxide as the positive electrode and graphite as the negative electrode material is illustrated in Scheme 1.1.



Scheme 1.1: Reactions occurring at electrodes during charge and discharge in Li-ion battery with graphite as anode and LiCoO_2 as cathode.

1.5 Components of Li-ion batteries

1.5.1 Cathode materials

The positive electrode of a lithium ion battery has to fulfill some basic requirements proposed by Whittingham [20]:

- 1) The material contains a readily reducible/oxidizable ion; for example a transition metal ion.
- 2) The material reacts with lithium in a reversible manner and the lithium host structure does not charge during intercalation.
- 3) The material reacts with lithium with a high free energy of reaction (high capacity, preferably at least one lithium atom per transition metal atom and high voltage, preferably around 4 V vs Li^+/Li). This leads to high energy density.
- 4) The material reacts with lithium very rapidly on both insertion and removal, this leads to high power density.
- 5) The material is a good electronic conductor. This allows for reaction at all contact points between the cathode active material and the electrolyte rather than at ternary contact points between the cathode active material, the electrolyte, and the electronic conductor i.e. carbon black.
- 6) The material is stable, i.e. does not change structure or otherwise degrade, to overdischarge and over charge.
- 7) The material is inexpensive and environmentally benign.

Three main cathode families have been extensively studied over the years: layered oxides LiMO_2 ($M=\text{Co}, \text{Ni}, \text{Mn}, \text{etc}$), spinels LiM_2O_4 ($M=\text{Mn}, \text{Ni}, \text{etc}$), and olivines LiMPO_4 ($M=\text{Fe}, \text{Co}, \text{Ni}, \text{Mn}, \text{etc}$) [23].

LiMO_2 oxides have $\alpha\text{-NaFeO}_2$ layered structure. In a *ccp* oxygen array Li^+ and M^{3+} are distributed in the octahedral interstitial sites in such a way that MO_2 layers are formed consisting of edge-sharing $[\text{MO}_6]$ octahedral. In between these layers lithium resides in octahedral $[\text{LiO}_6]$ coordination, leading to alternating (111) planes of the cubic rock-salt structure [24].

Due to strong M-O bonds the MO_2 layers are relatively inert against electrochemical reduction/oxidation. On the other hand, the weak interlayer bonding interaction (comprised of an interplay of electrostatic repulsion and attraction among negatively charged MO_2 layers and

positively charged Li^+ cations together with a weak van der Waals interaction between the MO_2 layers) allows a reversible insertion/extraction of lithium in between the MO_2 layers [25].

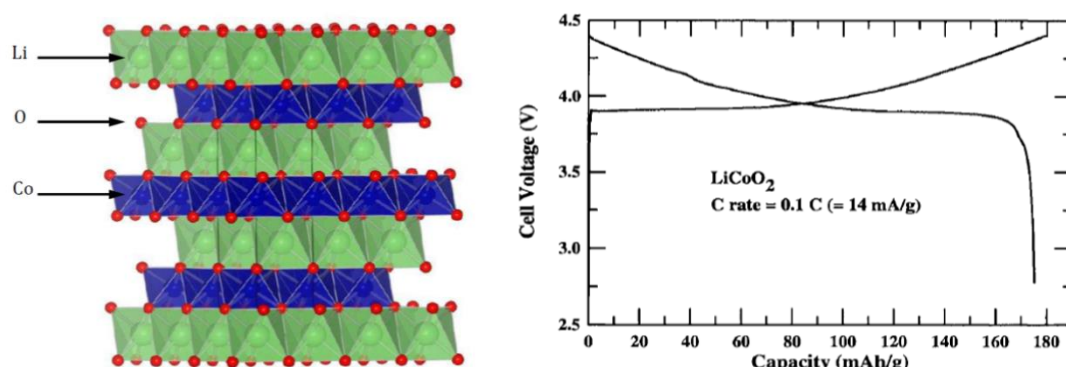


Figure 1.4: Crystal structure of LiCoO_2 (left) (adapted from [26]) and voltage profile of LiCoO_2 (right)(adapted from [25]).

LiCoO_2 (Fig.1.4) was first published by Goodenough [27]. This was at the origin of the commercial success of the high energy Li-ion batteries, mainly due to its cycling stability over thousand cycles. Lithium cobalt oxide exhibits a redox potential of 3.9 V- 4.1 V and a capacity of 140 Ah/kg [28]. This is due to the extraction/insertion of only 0.5 lithium equivalent in a reversible manner. The extraction of $\text{Li} > 0.5$ equivalents above 4.2 V lead to higher capacity (170Ah/kg) but also to structural distortion and capacity fading [25] . However, the cost, toxicity, and safety of cobalt based batteries led to the need for its replacement. Efforts to reduce the amount of cobalt by substitution with other transition metals, e.g. Mn and Ni, have resulted in a solid solution between LiCoO_2 , LiNiO_2 and LiMnO_2 to form $\text{LiCo}_{1/3}\text{Ni}_{1/3}\text{Mn}_{1/3}\text{O}_2$ (NMC) [29] with improved performance compared to LiCoO_2 . Its higher specific charge more than 200 Ah/kg, its broad redox potential between 3.6 V-4.4 V and its excellent rate capability allowed its use in commercial batteries (Fig.1.5).

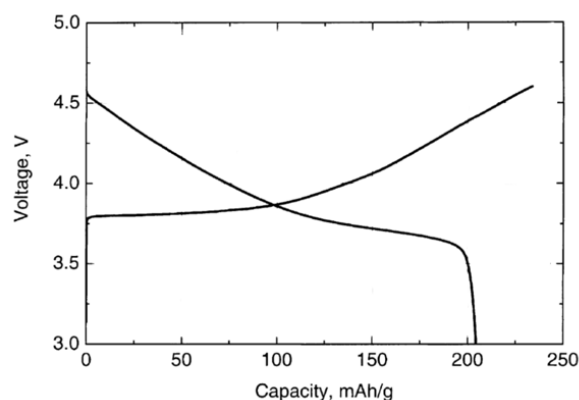


Figure 1.5: Voltage profile of NMC (adapted from [29]).

Another important novel material is the so-called integrated layered-layered cathode $0.5\text{Li}_2\text{MnO}_3\text{-}0.5\text{LiMn}_{1/3}\text{Ni}_{1/3}\text{Co}_{1/3}\text{O}_2$ that shows the composite structure of the two phases with a mixing at the atomic level. The Li_2MnO_3 is initially an inactive component so that the composite electrodes comprising these materials, which are cycled at a potential below 4.5 V vs Li^+/Li , only demonstrate the electrochemical activity of the LiMO_2 component. Upon activation of these materials, on the first cycle at potentials higher than 4.7 V vs. Li^+/Li , a pronounced irreversible structural change occurs that includes delithiation and partial loss of oxygen[30]. This irreversible process activates the Li_2MnO_3 components and forms a new active material which exhibits a broad redox potential window of 3.0 V - 4.5 V, thermal stability at elevates temperatures and capacities higher than 250 Ah/kg [31] (Fig.1.6).

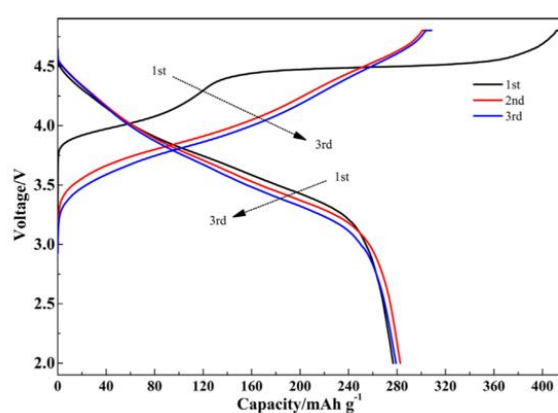


Figure 1.6: voltage profile of $0.5\text{Li}_2\text{MnO}_3\text{-}0.5\text{LiMn}_{1/3}\text{Ni}_{1/3}\text{Co}_{1/3}\text{O}_2$ (adapted from [32])

LiM_2O_4 oxides have MgAl_2O_4 spinel-type structure. In a *ccp* array of oxygen atoms, Li^+ occupies 1/8 of the tetrahedral sites and $\text{M}^{3+/4+}$ occupied 1/2 of the octahedral sites. A strong edge-shared octahedral $[\text{M}_2]\text{O}_4$ array permits a reversible extraction of the Li^+ ions from the tetrahedral sites without provoking a collapse of the 3-dimensional $[\text{M}_2]\text{O}_4$ spinel framework [25].

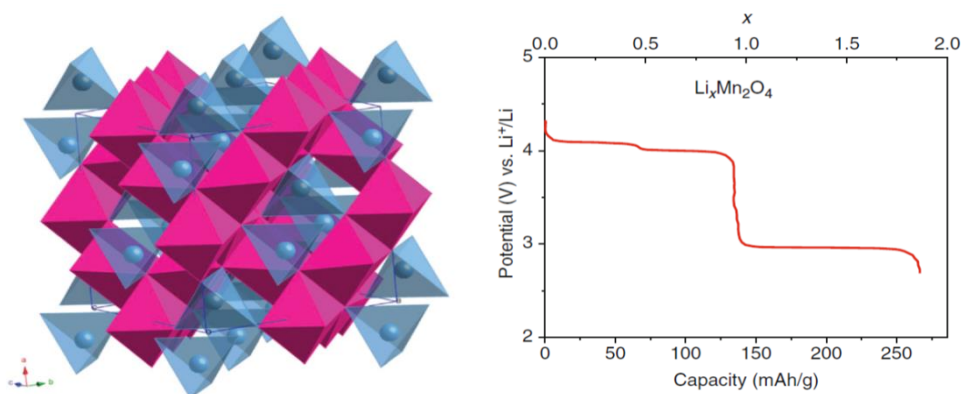


Figure 1.7: Crystal structure of LiMn_2O_4 (adapted from [33]) and voltage profile of LiMn_2O_4 (adapted from [34]).

The LiMn_2O_4 spinel [35] has a redox potential around 4.0 V and a capacity around 120 Ah/kg due to extraction/insertion of lithium ions from/into tetrahedral sites transforming LiMn_2O_4 in $\lambda\text{-MnO}_2$. When one additional lithium equivalent is inserted into the structure a flat plateau around 3.0 V occurs (Fig.1.7). This is the result of the transition from cubic $\text{Li}[\text{Mn}_2]\text{O}_4$ to tetragonal $\text{Li}_2[\text{Mn}_2]\text{O}_4$ caused by the Jahn-teller effect of the Mn^{3+} ion [25]. Although the insertion of two lithium equivalents increases the capacity up to 250Ah/kg, the 3V region limits the cyclability of LiMn_2O_4 . In recent years Mn has been partially substituted by Ni to improve this type of spinel. $\text{LiMn}_{1.5}\text{Ni}_{0.5}\text{O}_4$ has higher redox potential around 4.7-4.8V and a higher capacity of 140 Ah/kg [36] (Fig.1.8).

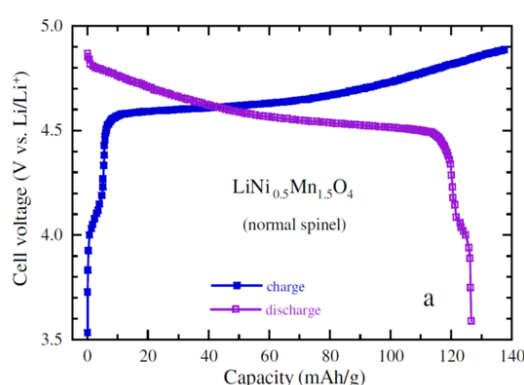


Figure 1.8: voltage profile of $\text{LiMn}_{1.5}\text{Ni}_{0.5}\text{O}_4$ (adapted from [37]).

LiMPO_4 oxides have an Mg_2SiO_4 olivine-type structure. In an *hcp* array of oxygen atoms Li^+ and Fe^{2+} occupy $1/2$ of octahedral sites and P^{5+} occupies $1/8$ of tetrahedral sites. Corner-shared MO_6 octahedra are linked together in the *bc*-plane, while LiO_6 octahedra form edge-sharing chains along the *b*-axis building up the channel from where the lithium ions can be removed. The tetrahedral PO_4 groups bridge neighboring layers of MO_6 octahedra by sharing a common edge with one MO_6 octahedra and two edges with LiO_6 octahedra [38] (Fig.1.9).

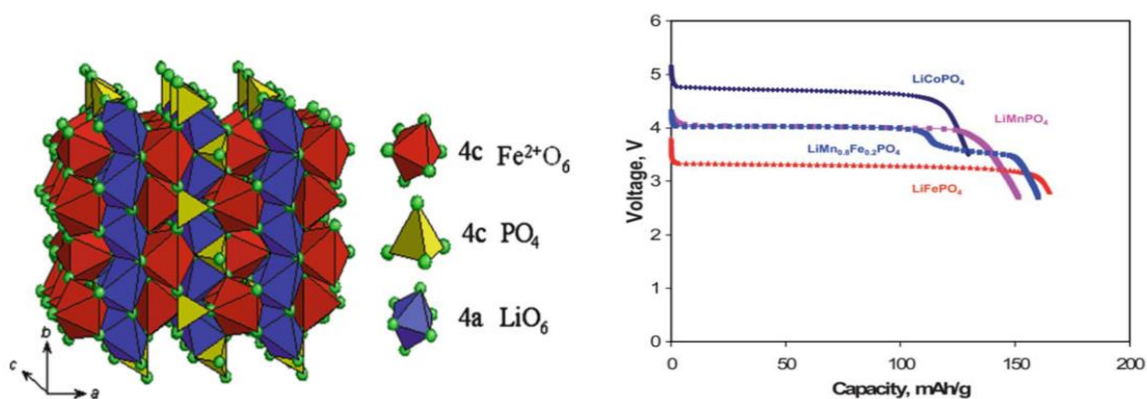


Figure 1.9: Crystal structure of LiFePO_4 (adapted from [38]) and voltage profile of different olivine cathode materials (adapted from [39]).

Within this family, the compounds where M is Fe, Mn, and Co exhibit the following redox potential vs Li^+/Li : 3.5 V, 4.1 V and 4.8 V respectively (Fig 9). The advantage of these materials in comparison with other cathode materials is that lithium insertion/extraction occurs with a very flat plateau due to two-phase process during lithiation/delithiation. However, the electronic conductivity has to be improved by carbon coating [40]. The low surface reactivity of the olivine gives the possibility to create nano- LiMPO_4 particles to improve Li intercalation/deintercalation. LiFePO_4 [41] reaches a capacity of 160 Ah/kg, it is cheap and has a good cyclability but due to its low redox potential, researchers in this field have turned their attention to the Mn-containing analog with higher voltage and a capacity of 140 Ah/kg [42].

1.5.2 Anode materials

It is generally accepted by the battery community that graphite electrode is the most suitable material due to its unique characteristics in terms of safety, high capacity (372 Ah/kg), cyclability and low voltage range (0.25-0.05V vs Li^+/Li) for the lithium insertion/extraction reaction [40].

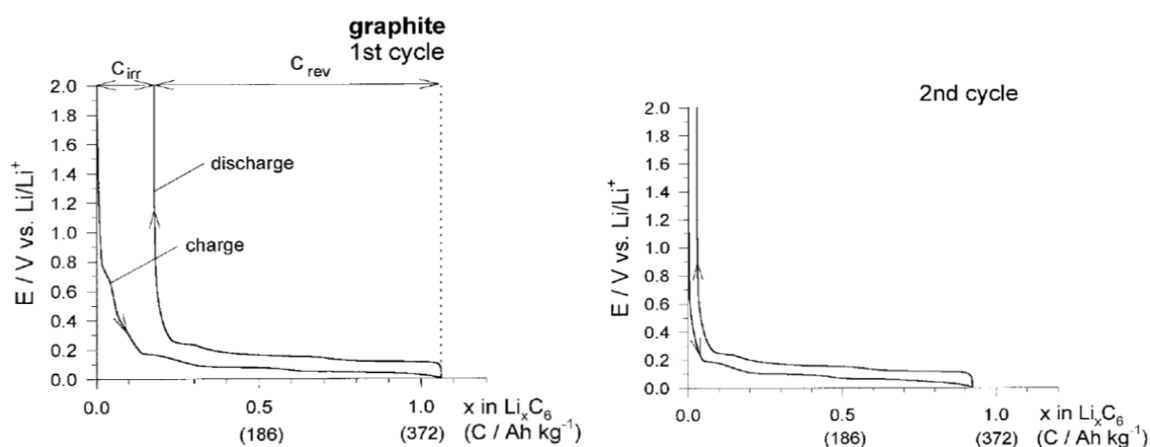


Figure 1.10: 1st and 2nd cycle of graphite (adapted from [24]).

Graphite can be reduced to LiC_6 (Scheme 1.1) upon lithium intercalation. The reversibility of this reaction was initially compromised by the choice of the electrolyte, in fact, the use of propylene carbonate (PC) –based electrolytes leads to the intercalation of solvent molecules between graphite layers with consequent exfoliation and poor cyclability. Since 90s the use of ethylene carbonate (EC) and dimethyl carbonate (DMC)-based electrolyte allowed a reversible intercalation of lithium ions in the graphite[24].

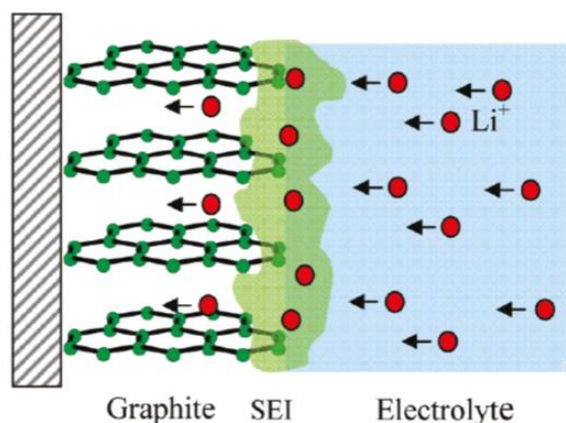


Figure 1.11: Schematic presentation of the formation of the SEI layer by decomposition of EC-based electrolytes [43].

During the first charge the capacity exceeds the theoretical one because of the SEI formation. EC reduction forms a passivation layer on the external graphite surface in the early stage of reduction, this film prevents excessive solvent co-intercalation. In the second cycle 85-90% of the theoretical capacity is recovered (Fig 1.10 and 1.11).

New materials based on Sn or Si alloy have been investigated recently. Tin and silicon behave similarly upon alloying with Li, with similar stoichiometries and >300% changes in volume [40]. Between them, the Si is more promising because it is more abundant and can reach higher capacity ($\text{Li}_{4.4}\text{Si}$: 4200 mAhg^{-1} vs $\text{Li}_{4.4}\text{Sn}$: 900 mAhg^{-1}). It was found that the use of nanowires of Si or Sn improves in the accommodation of the mechanical strain that occurs during the volume changes [44].

Metal oxide with low voltage vs Li^+/Li are also being studied as anode materials as for example $\text{Li}_4\text{Ti}_5\text{O}_{12}$ and Li_3VO_4 . The former, with a redox potential of 1.5 V vs Li^+/Li and a capacity of 160 Ah/kg [45] was recently overtaken by the latter which has a redox potential of 1.0 V vs Li^+/Li and a capacity of 300 Ah/kg [46].

1.5.3 Electrolyte

Conventional electrolytes for lithium-ion batteries consists of an inorganic salt dissolved in organic solvents with a large electrochemical stability window (1.3 V- 5.0 V vs Li^+/Li) (Fig 1.12). The electrochemical window is defined by the energy separation E_g between HOMO and LUMO of the solvent; To prevent oxidation and/or reduction of the electrolyte, E_g has to be larger than the difference in electrochemical potential between anode and cathode [43]. A suitable electrolyte should have high ionic conductivity ($> 10^{-4} \text{ S/cm}$) and low electronic con-

ductivity ($<10^{-10}$ S/cm), high chemical stability, low cost and assure safety. Solvents with low melting points, high boiling points and low vapor pressures are highly desirable. The best choice was found to be a mixture of alkyl carbonates like ethylene carbonate (EC) and either dimethyl carbonate (DMC) or ethyl methyl carbonate (EMC) with a Li salt like LiPF_6 . Lithium hexafluorophosphate LiPF_6 is, at present, the electrolyte salt for most commercial lithium-ion batteries because it is highly soluble in alkyl carbonates solvents forming a high Li^+ conducting solution. However, it is expensive to produce in the high purity needed and it is also prone to hydrolysis, forming the highly toxic hydrofluoric acid (HF) [39].

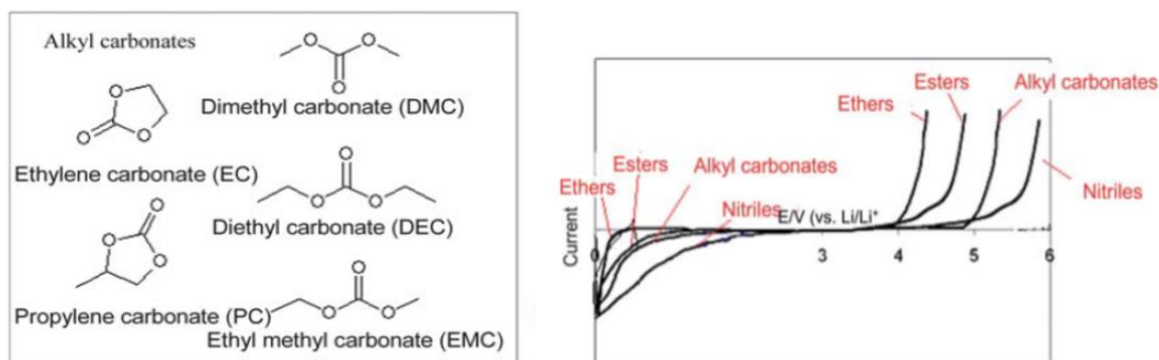


Figure 1.12: Organic solvent commonly used as electrolytes in Li-ion batteries (left). Schematic presentation of the electrochemical window of various solvent families with Li salt (right) (adapted from [39]).

Room temperature ionic liquids (RTIL), have been proposed and investigated as safe solvents of Li-ion battery electrolytes. They are composed of an organic cation (i.e. imidazolium cations (RRIm^+), pyridinium cations (RRPy^+), tetraalkylammonium cations (RRRRN^+)) combined with a variety of large anions having a delocalized charge (PF_6^- , BF_4^- , $\text{N}(\text{F}_2\text{SO}_2)_2^-$). The main advantages over organic electrolytes are 1) higher oxidation potential ~ 5.3 V vs Li^+/Li , 2) safety features (non-flammability and non-volatility) but the main drawbacks are high viscosity and low ionic conductivity at low temperatures. The final electrolyte is usually composed by an IL and a lithium salt which in most of the case include the anion composing the electrolyte [47].

Recently, solid electrolytes are also being studied due to their very wide electrochemical window (0.0 V – 5/6 V vs Li^+/Li) and safety. The most important families are: 1) perovskite – type structure like lithium lanthanum titanate (LLTO) $\text{Li}_{3x}\text{La}_{(2/3-x)}\text{Ti}_{(1/3-2x)}\text{TiO}_3$ ($0 < x < 0.16$), 2) NASICON- type $\text{LiGe}_2(\text{PO}_4)_3$ or $\text{Li}_{1.3}\text{Al}_{0.3}\text{Ti}_{1.7}(\text{PO}_4)_3$, and 3) garnet-type structure like LLZO ($\text{Li}_7\text{La}_3\text{Zr}_2\text{O}_{12}$) electrolyte. The first two have Li^+ conductivity around 10^{-3} S/cm and the last one around 10^{-4} S/cm [48].

1.5.4 Current collector

The positive electrode and the negative electrode are usually casted on aluminum and copper current collectors, respectively. Aluminum is used for the positive electrode because it is stable at high voltages vs Li^+/Li , has a high electronic conductivity, is cheap and light [49]. In the same way copper is used for negative electrodes due to its stability at low voltages vs Li^+/Li [50].

1.5.5 Separator

The separator is placed between the positive electrode and the negative electrode to prevent physical contact of the electrodes while enabling free ionic transport and isolating electronic flow. It is a microporous layer consisting of either a polymeric membrane (Polyethylene – PE or Polypropylene –PP), a non-woven fabric mat (fiber of natural cellulose or polymer like PVDF or PVF) or an inorganic composite ($\text{Al}_2\text{O}_3/\text{SiO}_2$). It must be chemically and electrochemically stable in the presence of the electrolyte and electrode materials, and must be mechanically strong to withstand the high tension during the battery assembly operation. The separator should have sufficient porosity to absorb liquid electrolyte for high ionic conductivity. Therefore, the selection of an appropriate separator is critical to the battery performance, including energy density, power density, cycle life and safety [51].

1.6 Mn-based cathode materials

1.6.1 Advantages of Mn-based cathode materials

Manganese is one of the most common transition metals used in battery materials due to its peculiar characteristics:

- 1) It has multiple (and at least partially accessible) oxidation states leading to the possibility to intercalate more than one lithium atom per transition metal atom (requisite 3 for cathode materials).
- 2) It benefits of redox couples which allow obtaining a potential range between 3.0 V and 4.2 V vs Li^+/Li depending on the crystal structure and the chemical composition. The most common redox couple are $\text{Mn}^{2+}/\text{Mn}^{3+}$ or $\text{Mn}^{3+}/\text{Mn}^{4+}$ [42, 52-58].
- 3) It is not toxic and highly available.

However, Mn-based cathode materials suffer of stability problems due to Mn^{2+} dissolution in the electrolyte [59] and the Jahn-Teller effect of the Mn^{3+} ion [60] which limits their cycle

life. Many solutions have been proposed to achieve better stability like doping [61] or surface coating [62]. In this work, Ca_2MnO_4 , Li_3MnO_4 and LiMnBO_3 Mn-based cathode materials were studied to improve their electrochemical performances through structural, morphological and chemical modifications.

1.6.2 Crystal Field Theory (CFT) in Mn-based cathode materials

The Crystal Field Theory describes the origins and consequences on the orbital energy levels of a transition metal ion caused by the electrostatic interactions between negatively charged ligands and positively charged transition metal ions. The changes induced on the d level splitting of the central transition metal ion depend on the type, positions and symmetry of the surrounding ligands [63].

Although a model based on purely electrostatic interaction has its own limitations, CFT is quite successful to interpret materials properties as crystal structure, color and redox potential. In order to understand clearly the interactions that are responsible for the crystal field effect in transition metal complexes, it is necessary to briefly describe the geometry of the d orbitals.

The five d orbitals which occur in each shell with principal quantum number 3 or higher are described by five wave functions designated with d_{xy} , d_{yz} , d_{xz} , $d_{x^2-y^2}$ and d_z^2 . Three of the orbitals d_{xy} , d_{yz} , d_{xz} have lobes projecting between the cartesian axes. The other two orbitals, $d_{x^2-y^2}$ and d_z^2 have lobes directed along the cartesian axes as shown in Fig.1.13 [63]. The energy levels of these five orbitals are degenerated in a free metal ion.

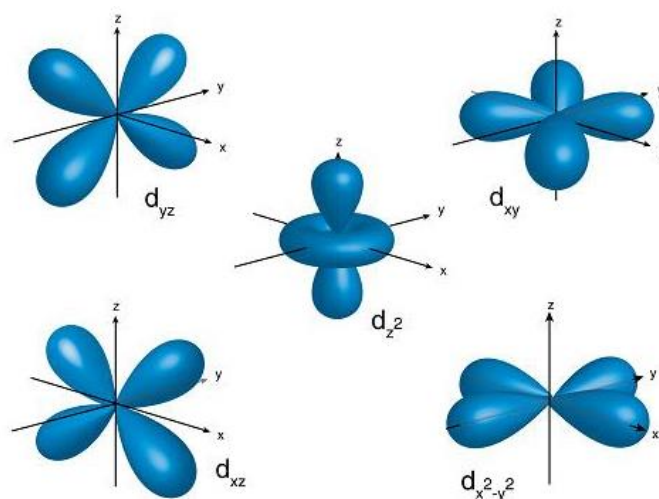


Figure 1.13: Spatial arrangement of the d orbitals.

The interaction between a central metal ion with six ligands in octahedral symmetry along the x, y and z axes lead to the removal of degeneration. The orbitals lying along these axes will

interact to higher extent with the ligands, increasing in energy in comparison with the orbitals lying between the axes which will decrease in energy. This give rise to the splitting of d orbitals energy levels in two groups: t_{2g} (d_{xy} , d_{yz} , d_{xz}) and e_g ($d_{x^2-y^2}$ and d_z^2) with t_{2g} orbitals having lower energy than e_g . The extent of the separation is called crystal field splitting and is labeled with Δ_0 [64].

In this model, the splitting of the 3d orbital energy levels is assumed to obey a 'center of gravity' rule. As a result, the three t_{2g} orbitals are lowered by $0.4 \Delta_0$ below, and the two e_g orbitals raised by $0.6 \Delta_0$ above, the barycenter. This follows from a simple algebraic argument that the energy of six electrons in the three t_{2g} orbitals is compensated by the energy of four electrons in the two e_g orbitals. Each electron in a t_{2g} orbital thus stabilizes a transition metal ion by $0.4 \Delta_0$, whereas every electron in an e_g orbital diminishes the stability by $0.6 \Delta_0$. The resultant net stabilization energy is called the crystal field stabilization energy and is designated by CFSE [63].

In the same way, the interaction between the central metal ion and four ligands in tetrahedral symmetry or five ligands in square based pyramidal symmetry will split the energy levels of the 3d orbitals by a different extent (Fig.1.14)

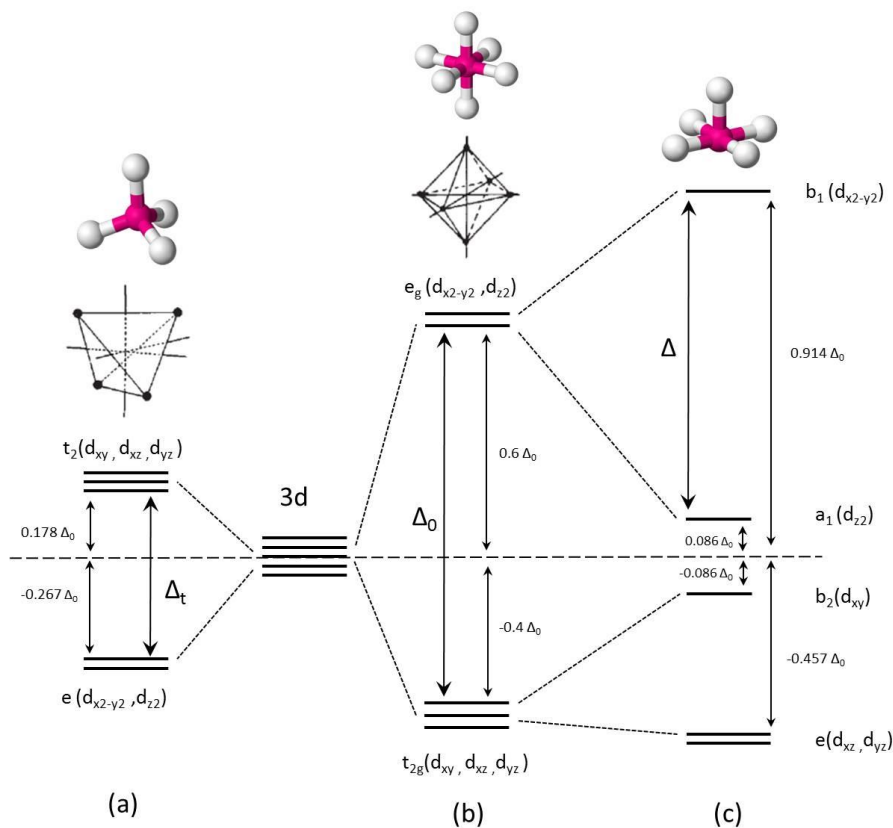


Figure 1.14: Crystal field splitting of transition metal 3d orbitals in (a) tetrahedral, (b) octahedral and (c) square pyramidal symmetry. For convenience, the energy barycenter is depicted as the same, although it may not be for the three types of coordination.

The considerations showed above can be applied to cathode materials to predict, at least theoretically, which redox couple may be active in a Li-ion battery. Because our study was focused on three Mn-based compounds: Ca_2MnO_4 , Li_3MnO_4 and LiMnBO_3 with oxidation state (IV), (V) and (II) in octahedral, tetrahedral and square pyramidal coordination, respectively; a comparison between the redox couples which should give rise to electrochemical activity in these compounds is shown in Fig. 1.15.

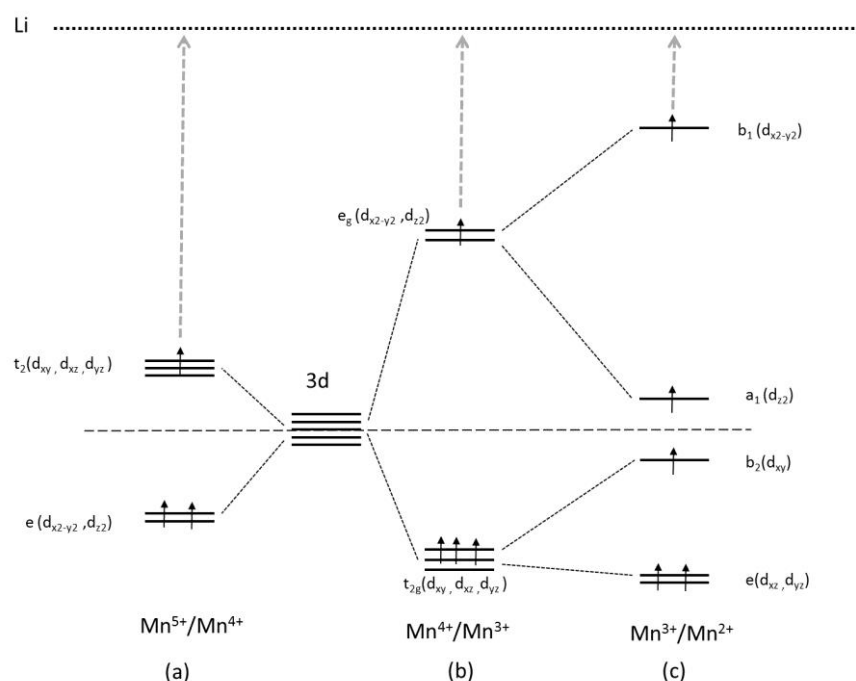


Figure 1.15: Electron occupancy of the d-orbitals and redox couples: a) $\text{Mn}^{5+}/\text{Mn}^{4+}$ in tetrahedral coordination, b) $\text{Mn}^{4+}/\text{Mn}^{3+}$ in octahedral coordination and c) $\text{Mn}^{3+}/\text{Mn}^{2+}$ in square-based pyramidal coordination [64, 68, 70]. For convenience, the energy barycenter is depicted as the same, although it may not be for the three types of coordination. The horizontal dotted line displays the hypothetical Li potential.

In octahedral coordination the oxidation of Mn^{3+} to Mn^{4+} is the result of the extraction of one electron from the e_g orbitals. This is one of the most common redox couple for Mn-based cathode materials as LiMn_2O_4 , LiMnO_2 etc. The potential of this redox couple was found to be around 4.0 V if Li ions are extracted from tetrahedral sites, and around 3.0 V if Li ions are extracted from octahedral sites [35, 65, 66]. The further oxidation of Mn^{4+} to Mn^{5+} in O_h coordination needs the extraction of one electron from the low energy lying t_{2g} orbitals. The expected voltage of this oxidation step ($\text{Mn}^{5+}/\text{Mn}^{4+}$, O_h) would be much higher than the 4V of the $\text{Mn}^{4+}/\text{Mn}^{3+}$ redox couple and it is not feasible in any known electrolyte. However, if we consider the tetrahedral coordination, the oxidation of Mn^{4+} to Mn^{5+} should be feasible, be-

cause this process removes an electron from the high-lying t_2 orbitals. Furthermore, since all the orbitals remain close in energy due to the relatively weak splitting caused by tetrahedral ligands, even oxidation states above Mn^{5+} , which draw electrons from the lower e levels, are expected to be relatively close in potential to the Mn^{4+}/Mn^{3+} in O_h coordination [67].

Square pyramidal coordination is quite rare for manganese-based oxides and no literature is present about the electronic configuration in this coordination. However, studies have shown that Mn^{2+} has high spin electronic configuration in O_h coordination due to very high exchange splitting energy [68]. It is proposed that the Mn^{2+} to Mn^{3+} oxidation in this coordination occurs because of the extraction of one electron from the high lying b_1 orbitals which takes place at a potential around 3.0 V [69].

In conclusion, depending on the geometry around the central metal ion and its oxidation state, the manganese gives the possibility to exploit a higher number of redox couples which are not possible to be exploited with other transition metal elements. This is extremely important for the design of new materials for Li-ion batteries.

Chapter 2

2. Materials synthesis and characterization methods

2.1 Materials

2.1.1 Synthesis of μ -Ca₂MnO₄ and n-Ca₂MnO₄

Ruddlesden-Popper (RP)-type μ -Ca₂MnO₄ calcium manganates were prepared by a soft chemistry method [71-74] using analytical grade citric acid (CA) (Sigma-Aldrich 99%), Ca(NO₃)₂·4H₂O (Sigma-Aldrich >99%) and Mn(NO₃)₂·4H₂O (Sigma-Aldrich 98%) with a CA:Ca:Mn ratio of 8:2:1. The precursors were dissolved in a round bottom flask containing 50 mL of high purity water. The solution was subjected to a reflux for 4h, then poured into a borosilicate glass bowl and heated in an oven according to the following temperature program: the furnace was heated to 100 °C with a heating rate of 20 °C/min, and held for 12h, and then the temperature was increased to 300 °C with a heating rate of 20 °C/min and held for 4 h. During the first step, the solution dried sufficiently to form a gel. During the second step, the decomposition of the precursor nitrates created a solid foam. The solid foam was ground in an agate mortar, and loaded into an alumina crucible and calcined to remove residual organics: the sample was heated at a rate of 30 °C/min to 800 °C and held for 12 h. The resulting powder was ground, pressed into a pellet, and annealed at 1000 °C for 18h and again at 1100 °C for 12 h to obtain pristine Ca₂MnO₄.

Nano Ca₂MnO₄ (n-Ca₂MnO₄) was prepared by a soft chemistry method [72] using analytical grade citric acid (CA) (Sigma-Aldrich 99%), ethylene glycol (EG) (VWR 98%), Ca(NO₃)₂·4H₂O (Sigma-Aldrich >99%) and Mn(NO₃)₂·4H₂O (Sigma-Aldrich 98%) with a CA/EG ratio of 1 and a CA/metal ion ratio of 1. The precursors were dissolved in a round bottom flask containing 50 mL of high purity water. The solution was heated to allow the evaporation of water and the formation of the gel. The gel was heated at 250 °C for 6 h with a heating rate of 1 °C/min. The solid foam formed was ground in an agate mortar, loaded into an alumina crucible and calcined at 800 °C for 12 h.

2.1.2 Activation of μ -Ca₂MnO₄ and n-Ca₂MnO₄

The modification of Ca₂MnO₄ was achieved by suspending the pristine powder in an aqueous solution of H₂SO₄. In all reactions the acid concentration was kept constant by setting the pH value to pH=2 and the same quantity (0.5g) of pristine material was used for each sample. Theoretical calcium extractions of 25at%, 50at%, 75at% and 90at% were obtained by changing only the volume of the solution. The samples were named throughout the text as μ -Ca₂MnO₄-25%Ca-extr, μ -Ca₂MnO₄-50%Ca-extr, μ -Ca₂MnO₄-75%Ca-extr and μ -Ca₂MnO₄-90%Ca-extr.

The pH was monitored and the reaction was stopped after 24 h. During this time a steady pH was reached. The solution was then filtered and the residue (a black solid) was washed with distilled water and dried in an oven for 2 h at 75 °C in air.

For comparison amorphous hydrated manganese dioxide was prepared by mixing 1.58 g of KMnO₄ dissolved in 60 mL of high purity water with 3.68 g of manganese (II) acetate dissolved in 100 mL of high purity water as already reported [75].

A blend between pristine μ -Ca₂MnO₄ and MnO₂·xH₂O (supposing to contain roughly 1 eq. of water[76]) with an atomic ratio Ca/Mn of 1 was prepared mixing the right quantities in a mortar.

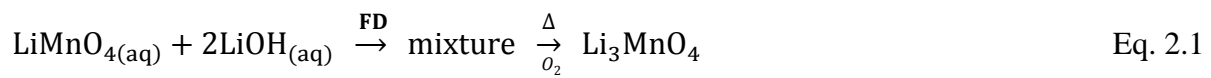
The modification of n-Ca₂MnO₄ was performed as described above. Theoretical calcium extractions of 25 at%, 50 at% and 75 at% were obtained. The samples were named throughout the text as n-Ca₂MnO₄-25%Ca-extr, n-Ca₂MnO₄-50%Ca-extr, and n-Ca₂MnO₄-75%Ca-extr.

2.1.3 Synthesis of SSR-Li₃MnO₄ (solid state route)

SSR-Li₃MnO₄ was prepared by a solid state route, typically used to synthesize this material [67]. A ground mixture of LiMnO₄·3H₂O and LiOH·H₂O (Alfa Aesar, 98% min) in a 1:2 ratio was introduced into a furnace under oxygen flow. The sample was heated at 1°C/min from RT to 70 °C. At this temperature the sample was re-ground and heated by steps of 10°C until 125°C. After 1h at 125°C the heating was continued at 1°C/min to 170°C and then heated for 3h. The LiMnO₄·3H₂O precursor was prepared by ion exchange from KMnO₄ as described elsewhere [77] .

2.1.4 Synthesis of FDR-Li₃MnO₄ (freeze drying route)

FDR- Li₃MnO₄ was prepared by freeze drying route in a two-step reaction. In the first step the synthesis of LiMnO₄·3H₂O was performed. At this stage LiOH·H₂O was added to the solution containing LiMnO₄·3H₂O (ratio of 2:1 for hydroxide: permanganate) (Eq. 2.1). The solution was initially cooled in liquid nitrogen and then maintained under vacuum (0.6 Pa) to remove the water by sublimation. As a result, a freeze dried purple powder was obtained. The powder was then introduced in the furnace and was subjected to the same heating steps as SSR-Li₃MnO₄.



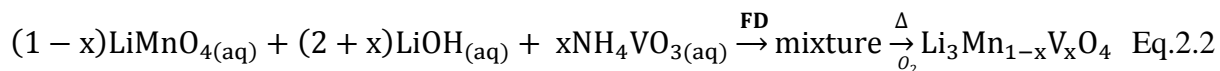
2.1.5 Preparation of Li₃MnO₄ cycled electrodes

SSR-Li₃MnO₄ sample and the equipment described in subchapter 2.3 were used to prepare the cycled electrodes. The electrodes were freshly prepared as described in section 2.3.2 and then underwent to the following cycling: the batteries were cycled in galvanostatic mode following the cell voltage until the intended electrochemical reaction was completed, then the cycle was stopped. The cells were quickly transferred into the glove box, where they were opened allowing collecting the electrodes at different charge. These electrodes were subjected to further analysis as described below. The analyzed electrodes were named through the text as: Li₃MnO₄-fresh for the fresh electrode (not cycled), Li₃MnO₄-1, Li₃MnO₄-2, Li₃MnO₄-3, and Li₃MnO₄-4 for the cycled electrodes where the electrochemical reaction was stopped in the points 1, 2, 3, and 4 respectively. Point 1 and 4 are charged states at 4.2 V after initial charge, and after discharge to 1.5 V followed by charging to 4.2 V, respectively. Point 2 and 3 are discharged states at 1.5 V after charge to 4.2 V followed by discharge to 1.5 V, and after initial discharge, respectively.

2.1.6 Incorporation of vanadium in Li₃MnO₄

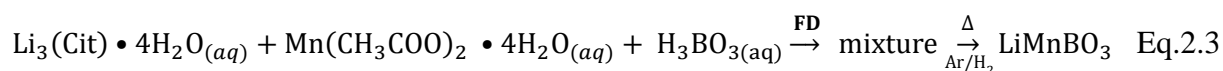
First, the synthesis of lithium permanganate (LiMnO₄) was performed by ion exchange reaction from potassium permanganate [77]. Then, lithium hydroxide (LiOH·H₂O) was added, to the solution containing LiMnO₄ creating a solution with pH around 12 (Eq.2.2). NH₄VO₃ was then added in the desired amount. The highly basic solution allowed the deprotonation of the

ammonium ion (NH_4^+) to form gaseous ammonia (NH_3). The solution was then freeze dried to obtain a purple powder. The powder was heated and ground by steps of 10°C from 70°C to 125°C then 1h at 125°C and 3h at 170°C under O_2 flow.



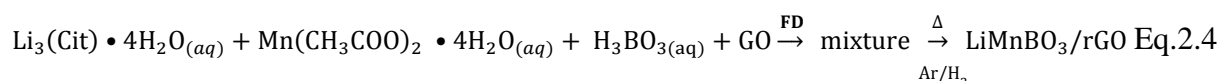
2.1.7 Synthesis of FDR-LiMnBO₃

FDR-LiMnBO₃ was prepared by a freeze drying route (Eq. 2.3). Lithium citrate tetrahydrate $\text{Li}_3(\text{Cit}) \cdot 4\text{H}_2\text{O}$ (Fluka analytical >99.5%), manganese acetate tetrahydrate $\text{Mn}(\text{CH}_3\text{COO})_2 \cdot 4\text{H}_2\text{O}$ (Merck > 99%) and boric acid (Sigma-Aldrich, > 99,5%) in a ratio 1/3:1:1 were dissolved in 20ml of high purity water. The solution was initially cooled in liquid nitrogen and then maintained under vacuum (0.6 Pa) to remove the water by sublimation. As a result, a freeze dried white powder was obtained. The powder was pressed in a pellet and introduced in the furnace for 12 h at 300°C under Ar/H₂ 95/5 mol% atmosphere. The pellet was then ground and the powder reheated at 400°C for 12 h in the same atmosphere.



2.1.8 Synthesis of FDR-LiMnBO₃/rGO

FDR-LiMnBO₃/rGO was prepared by a freeze drying route (Eq. 2.4). Lithium citrate tetrahydrate $\text{Li}_3(\text{Cit}) \cdot 4\text{H}_2\text{O}$ (Fluka analytical >99.5%), manganese acetate tetrahydrate $\text{Mn}(\text{CH}_3\text{COO})_2 \cdot 4\text{H}_2\text{O}$ (Merck > 99%) and boric acid (Sigma-Aldrich, > 99,5%) in a ratio 1/3:1:1 were dissolved in 20ml of high purity water. 10 ml of a GO solution (20g/L) was then added to obtain a ratio LiMnBO₃/GO of 80:20 wt%. To reduce GO agglomeration, a few mg of LiOH were added to reach a lightly basic pH around 8 and obtain an agglomerate-free fluid solution. The solution was cooled in liquid nitrogen and maintained under vacuum (0.6 Pa) to remove the water by sublimation. As a result, a freeze dried brown powder was obtained. The powder was pressed in a pellet and introduced in the furnace for 12 h at 300°C under Ar/H₂ 95/5 mol% atmosphere.



2.2 Physico-chemical characterization

2.2.1 X-ray diffraction (XRD)

Powder XRD measurements were performed for all samples on a PANalytical X'Pert PRO system equipped with a Johansson monochromator (Cu-K α_1 radiation, 1.5406 Å) and an X'Celerator linear detector operating in Bragg-Brentano geometry ($\theta/2\theta$). The diffraction patterns in Chapter 3, Chapter 4 subchapter 4.3 and 4.4 were recorded between 10° and 80° (2 θ) with an angular step interval of 0.008° and a time per step of 45s. The diffraction patterns in Chapter 4 subchapter 4.2 were recorded between 10° and 80° (2 θ) with an angular step interval of 0.004° and a time per step of 150s. The diffraction patterns in Chapter 5 were recorded between 10° and 80° (2 θ) with an angular step interval of 0.033° and a time per step of 200s.

In-situ high-temperature powder XRD patterns were obtained using a PANalytical X'Pert PRO θ - θ system with Cu-K α radiation ($\lambda = 1.5418$ nm).

The powder samples were placed in the heating chamber (XRK 900, Anton Paar, Austria) and a gas flow was applied through the mass flow controller (5850 TR, Brooks instrument, Germany). Roughly 0.03 g of sample powder was heated following material-specific temperature program. In chapter 3, the measurement was carried out in N $_2$ gas (99.999%, Messer, Switzerland) with a flow of 50ml/min from room temperature (RT) to 900°C with a heating rate of 20°C/min. In chapter 4 subchapter 4.2, the measurement was carried out in O $_2$ gas (99.999%, Messer, Switzerland) with a flow of 50 ml/min from room temperature (RT) to 170°C with a heating rate of 1° C/min. In chapter 4 subchapter 4.4, the measurement was carried out in Synthetic Air gas (99.999%, Messer, Switzerland) with a flow of 50 ml/min from room temperature (RT) to 700°C with a heating rate of 20 °C/min.

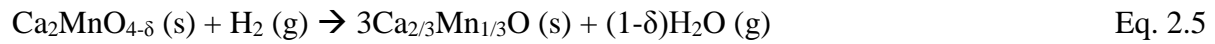
Data treatment and crystal phase identification were carried out with X'pert HighScorePlus software. The diffraction data in Chapter 4 subchapter 4.1 were analyzed by a profile matching mode (Le Bail fit) as implemented in the program *Fullprof*. Peak shapes were described by a Thompson-Cox-Hastings pseudo-Voigt function. The crystallite size was extracted from the microstructural analysis within the *Fullprof* software.

The diffraction data in chapter 5 were analyzed to extract the crystallite size by Williamson-Hall method.

2.2.2 Thermogravimetric analysis (TGA)

Thermogravimetric analysis experiments were performed with a NETZSCH STA 409 CD thermo-balance coupled with a quadrupole mass-spectrometer (Netzsch QMS 403 C Aeolos) sampling the thermobalance exhaust.

The oxygen content of the pristine μ -Ca₂MnO₄ phase in Chapter 3 subchapter 3.2 was determined from the relative sample weight loss (r). r was measured while heating 0.1 g of sample with 7.5 °C/min rate from 40 °C to 1200 °C under 50 ml/min flow of 5% H₂ in He. The oxygen content ($4-\delta$) was then calculated from r using Eq. 2.6 based on the reaction stoichiometry as stated in Eq. 2.5:



$$4-\delta = 4 - [(1-4r)\text{M}_\text{O} - 2r\text{M}_\text{Ca} - r\text{M}_\text{Mn}] / [(1-r)\text{M}_\text{O}] \quad \text{Eq. 2.6}$$

where M_i is the molar mass of the constituent element i . The Ca_{2/3}Mn_{1/3}O (s) solid-solution of the residual was verified using XRD.

To specify the H₂O-related volatile species present in the H₂SO₄-treated samples, an additional study was made using the sample ‘ μ -Ca₂MnO₄-25%Ca-extr’. The r was measured under both 5% H₂ in He and N₂ atmospheres. H₂O emissions from the sample with temperature were monitored using the mass-spectrometer. The reactively reducing 5% H₂ in He atmosphere is expected to facilitate the extraction of OH⁻ species, while H₂O should have atmosphere-independent extraction behaviour. The same heating program as described above for the pristine phase was employed with both atmospheres (maximum measurement temperature was 800 °C).

TGA data in Chapter 4 subchapter 4.2 were acquired on around 0.10 g of each powder. The sample was placed in an alumina crucible and heated at a rate of 20°C/min to 450°C in N₂ with a flow rate of 50 mL/min.

2.2.3 Scanning electron microscopy (SEM)

The morphology of the samples was studied with a Scanning Electron Microscope (SEM) FEI Nova NanoSEM 230 using ETD (Everhart-Thornley), TLD (Through-Lens), BSED (Back Scattered electrons) detectors with electron-beam energy of 5-10 keV. The chemical composition was determined by Energy Dispersive X-ray Spectroscopy (EDX) using electron-beam

energy of 20 keV in spot mode. The samples were sputtered with carbon or platinum in order to avoid charging effects in the images.

2.2.4 Transmission electron microscopy (TEM)

Transmission Electron Microscopy was carried out using a Philips CM30 (300 kV) equipped with a LaB₆ filament in bright field image and in selected area diffraction mode. A JEOL JEM 2000FS TEM/STEM (200kV) equipped with a high-angle annular dark field (HAADF) detector and an in-column Omega-type energy filter, was used to assess the morphology and local crystallinity of the samples by low-magnification imaging, and high-resolution electron micrographs (HREM). HREM images were further processed in the Digital Micrograph routine. Sample preparation was performed by depositing the powders suspended in ethanol or hexane on a holey carbon grid.

2.2.5 X-ray photoelectron spectroscopy (XPS)

X-ray photoelectron spectroscopy (XPS) spectra were acquired on a Physical Electronics (PHI) Quantum 2000 photoelectron spectrometer using monochromatic Al K α radiation (1486.6 eV) and a hemispherical capacitor electron-energy analyzer equipped with a channel plate and a position-sensitive detector. The electron take-off angle was 45°. The detail spectra were acquired with a pass energy of 58.7 eV and a step width of 0.250 eV for all measurements. The beam diameter was typically 150 μ m. A charge neutralizer system was used for all analyses. Data treatment was performed with CasaXPS software.

As for the XPS spectra in Chapter 4, subchapter 4.2, the C 1s signal position at 285.0 eV binding energy (BE) was used as an internal standard for calibration of the XPS peak positions. As for the XPS spectra in Chapter 4 subchapter 4.3, the C 1s of the adventitious carbon was not detectable because of the high amount of conductive carbon present in the electrodes. For this reason before and after measurements the peak position was calibrated with the signal of Au 4f_{7/2} at 83.95 eV as external standard. The samples were loaded on a XPS plate in a glovebox. The plate was closed in a sealed box to avoid contact with air during transportation from the glovebox to the XPS instrument. The plate was extracted from the sealed box and loaded in the pre-chamber under vacuum as fast as possible.

2.2.6 Raman spectroscopy

Raman spectra in Chapter 3 were measured on a Renishaw 2000 spectrometer equipped with holographic notch filters for elastic scattering and a CCD array detector. The WiRE software was used to collect the data. Sample powder was loaded onto a glass substrate, and excited with a red laser (632.816 nm). The laser was focused onto the sample using the optical microscope. The instrument was calibrated with a Si single crystal (Raman band at 520 cm^{-1}). The spectra were recorded at room temperature with an exposure time of 60 s and an accumulation number of 5. The range analyzed was between 1000 and 100 cm^{-1} .

Raman spectra in Chapter 4 subchapter 4.3 were measured using a Bruker Senterra instrument. Sample powder was loaded onto a glass substrate, and excited with a green laser (532 nm). The laser was focused onto the sample using a 50 times magnifying objective of the microscope, the laser beam power was 0.2 mW. The spectra were recorded in air, at room temperature with an exposure time of 15 s, an accumulation number of 5. The range analyzed was between 2000 and 100 cm^{-1} .

2.2.7 Surface area determination

Nitrogen adsorption and desorption experiments were performed at $-196\text{ }^{\circ}\text{C}$ on a Micromeritics ASAP 2020 Surface Area and Porosity Analyzer. The samples were evacuated for 1 h at 80°C under vacuum. The specific surface area (SSA) was determined using the Brunauer–Emmett–Teller (BET) model with N_2 gas (99.999%, Messer, Switzerland).

2.2.8 Particle size determination

Particle-size distribution was qualitatively analyzed by dynamic light scattering spectroscopy (DLS) with a Beckman Coulter LS230 Laser Diffraction Particle Analyzer (0.04 μm – 2000 μm) equipped with polarisation intensity differential scattering (PIDS) technology. Prior to measurement, the samples were suspended in water for Ca_2MnO_4 and toluene for Li_3MnO_4 and ultrasonicated for 5 min (Bandelin Sonoplus HD2200).

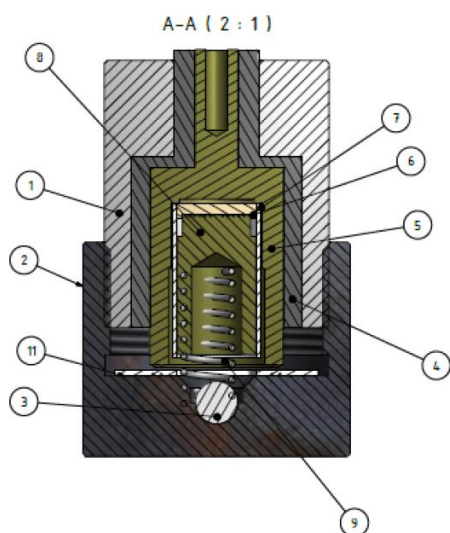
2.3 Electrochemical characterization

2.3.1 The equipment used for electrochemical measurements

Galvanostatic measurements were monitored by ASTROL, a computer software by Astrol Electronic AG. A potentiostat (BAT-SMALL battery cycler) was linked to a personal computer running Windows 7 by a serial-to-analog converter and by a serial cable. The assembled batteries were in-house built, two electrode cells. The technical drawing of the test cells is displayed in Fig. 1. The description of all parts and the used materials are given in Table 1.

The inner vertical stack was composed of a titanium current collector containing the EAM acting as working electrode, a polypropylene (PP) Cellgard 2400 (25 μm Polypropylene monolayer membrane) separator to prevent an internal short cut by lithium dendrites, a silica foam spacer filled with Merck® LP 50 electrolyte (1M LiPF_6 in EC/EMC 1:1) or LP30 electrolyte (1M LiPF_6 in EC/DMC 1:1) and covered with the lithium anode (Alfa Aesar 99.9% metal basis) acting as reference and counter electrode.

The battery test cells were assembled inside an argon filled dry glove box under inert conditions (< 0.1% H_2O and < 0.1% O_2). The potential values given through the text are referenced against Li^+/Li . Measurements were usually acquired at 10 A/kg or 50 A/kg.



Number	Element	Material
1	Container Top	Steel
2	Container Down	Steel
3	Ball-bearing; Ball	Steel
4	Insulation	PVC
5	Inward-container	Titanium
6	Current Collector	Titanium
7	Tube	PP
8	Lithium Support	Titanium
9	PP Sealing	PP

Figure 2.1: Technical drawing of the in-house test cell design.

2.3.2 Electrode preparation

Electrodes for electrochemical measurements in Chapter 3 were prepared by first mixing 60wt% of the electroactive material (EAM) with 30wt% of carbon black (Super P® Li from TIMCAL) and 10wt% of polyvinylidene difluoride (PVDF, Fluka powder Mw ~530k) in tetrahydrofuran (THF, Alfa Aesar 99%). This suspension was then dispersed ultrasonically for a few minutes until a dark homogenous suspension was obtained. The desired volume was transferred to a mortar and gently stirred with a pestle at room temperature. The THF evaporation leads to a very dark viscous solution that was then drop casted on the titanium current collector. The electrode was dried in air before being heat treated at 100 °C for 10 minutes. Electrodes containing 5 to 10 mg EAM were prepared by this method.

Electrodes for electrochemical measurements in Chapter 4 were prepared with 60/30/10 ratio between EAM, carbon and PVDF in toluene (Alfa Aesar 99%, anhydrous). After ultrasonication the desired volume was drop casted directly on the titanium current collector. The electrodes were dried in air before being heat treated at 80 °C for 1h in a vacuum oven. Electrodes containing 3 to 4 mg EAM were prepared by this method.

Electrodes for electrochemical measurements in Chapter 5 were prepared as follow: for FDR-LiMnBO₃ 60/30/10 ratio was used between EAM, carbon and PVDF in a solution THF:Toluene 1:1. In the case of FDR-LiMnBO₃/rGO the powder was directly suspended in THF. These suspensions were then dispersed ultrasonically and drop casted directly on the titanium current collector. The electrodes were dried in air before being heat treated at 80 °C for 1h in a vacuum oven.

Chapter 3

3. Manganese in octahedral coordination: activation of Ca_2MnO_4 for Li intercalation

3.1 Introduction

Mn-based Ruddlesden-Popper phases are promising materials for new battery cathodes due to their layered structure and often benign composition. The Ruddlesden-Popper (RP) phases are highly accommodating for transition-metal-site substitution [78-80], and form distinctly layered structures that are susceptible to Li insertion [81, 82]. The calcium manganate RP phases with the formula $\text{Ca}_{n+1}\text{Mn}_n\text{O}_{3n+1}$ ($n=1,2$ etc) or $\text{CaO}-(\text{CaMnO}_3)_n$ ($n=1,2,3\dots\infty$) are based on an array of corner sharing MnO_6 octahedra. When $n=\infty$, the typical orthorhombic perovskite structure is formed. When $n=1$, Ca_2MnO_4 forms the two dimensional (2D) K_2NiF_4 -type structure with CaMnO_3 perovskite blocks alternating with CaO rock salt layers [72] (Fig. 3.1). The synthesis of Ca_2MnO_4 is usually performed by solid state reaction or sol-gel reaction.

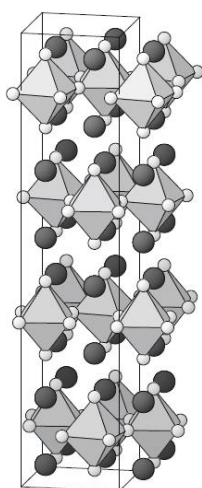


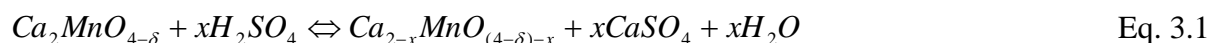
Figure 3.1: Structural representation of the Ruddlesden-Popper Ca_2MnO_4 .

Ca_2MnO_4 is very interesting since Ca and Mn are non-toxic and readily available elements and also Mn is an easily reducible/oxidable ion. On the other hand its extremely high resistivity [83] ($>20 \text{ M}\Omega$) prevents the use as battery material.

An acid treatment was designed to activate the material by extracting calcium, i.e. creating cation vacancies, in order to further facilitate lithium intercalation. Most reactions designed to extract/exchange interlayer ions rely on HCl [84]. However, the strong diprotic H_2SO_4 acid (with the double negatively charged SO_4^{2-} counter ion) should facilitate the Ca^{2+} extraction [85]. To our knowledge, Ca_2MnO_4 based oxides are not used as cathode material due to their poor performance. Therefore the aim of this research was to explore possibilities to enhance the electrochemical activity of pristine low cost Ca_2MnO_4 with an acid-treatment.

3.2 Acid treatment of $\mu\text{-Ca}_2\text{MnO}_4$ and characterization

Pristine $\mu\text{-Ca}_2\text{MnO}_4$ shows a basic behavior in high purity water (dissolution of 0.05 g of the compound in 0.05 L water results in a pH of 9.7) suggesting an easy removal of O^{2-} ions. When the acid treatment was carried out, Ca^{2+} ions were also extracted from the structure. The sulphate anions act as limiting reagent. The total calcium oxide extraction is explained by the following equation (Eq. 3.1):



The extracted Ca^{2+} ions reacted with sulphate anions, therefore CaSO_4 is recovered in the dried filtrate, as identified by XRD. The O^{2-} ions reacted with hydronium ions $\text{O}^{2-} + 2\text{H}_3\text{O}^+ \rightarrow 3\text{H}_2\text{O}$ leading to a neutral pH at the end of the extraction reaction for all cases. Consequently complete H_2SO_4 consumption during the reaction was concluded. The theoretical calcium extraction was calculated from the mass of the pristine $\mu\text{-Ca}_2\text{MnO}_{4-\delta}$ used, the initial pH and the volume of solution based on Equation 3.

The XRD pattern of the pristine Ruddlesden-Popper $\mu\text{-Ca}_2\text{MnO}_4$ and the Ca^{2+} -extracted compounds are shown in Figure 3.2.

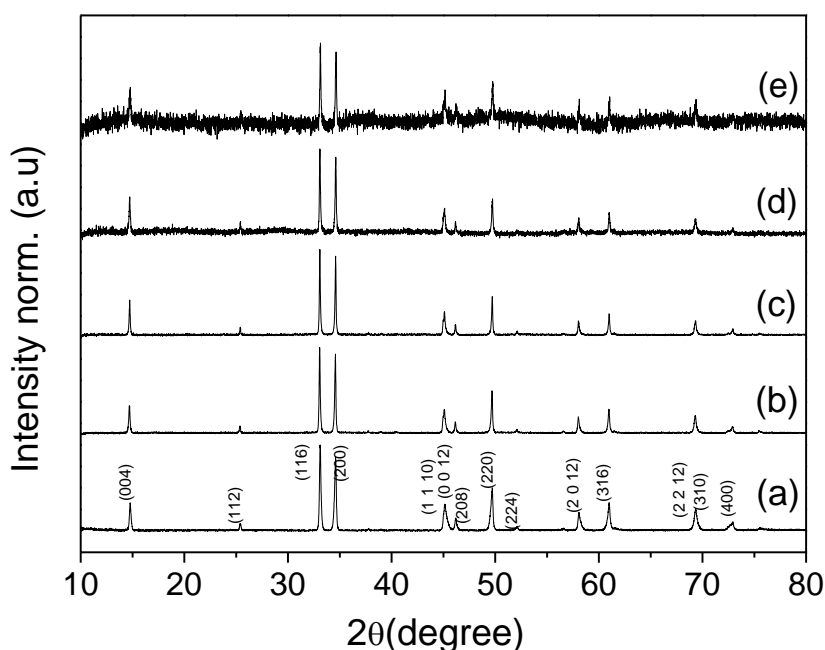


Figure 3.2: XRD pattern of $\mu\text{-Ca}_2\text{MnO}_4$ pristine (a), $\mu\text{-Ca}_2\text{MnO}_4$ -25%Ca-extr (b), $\mu\text{-Ca}_2\text{MnO}_4$ -50%Ca-extr (c), $\mu\text{-Ca}_2\text{MnO}_4$ -75%Ca-extr (d), $\mu\text{-Ca}_2\text{MnO}_4$ -90%Ca-extr (e).

All reflections in Figure 3.2(a) were indexed with the Ca_2MnO_4 , K_2NiF_4 -type structure belonging to tetragonal crystal system (space group $I4_1/acd$). The relative weight loss resulting from reductive TG measurement was measured as $r = 7.91(5) \%$ indicating an oxygen stoichiometry for the pristine phase as $(4-\delta) = 3.98(1)$. A tendency towards oxygen deficiency is typical for the oxide compounds of mid- and late-transition $3d$ metals having several relatively stable oxidation states [86-89]. The XRD patterns of the $\mu\text{-Ca}_2\text{MnO}_4$ -25%Ca-extr and $\mu\text{-Ca}_2\text{MnO}_4$ -50%Ca-extr compounds (Figure 3.2(b) and Figure 3.2(c)) revealed no perceptible 2θ -shift in comparison to the pristine compound. However, the peaks intensity decreases for the $\mu\text{-Ca}_2\text{MnO}_4$ -75%Ca-extr and $\mu\text{-Ca}_2\text{MnO}_4$ -90%Ca-extr (Figure 3.2(d) and 3.2(e)) compounds. Additional XRD analysis was carried out by in situ high-temperature XRD (HT-XRD) experiments (Figure 3.3).

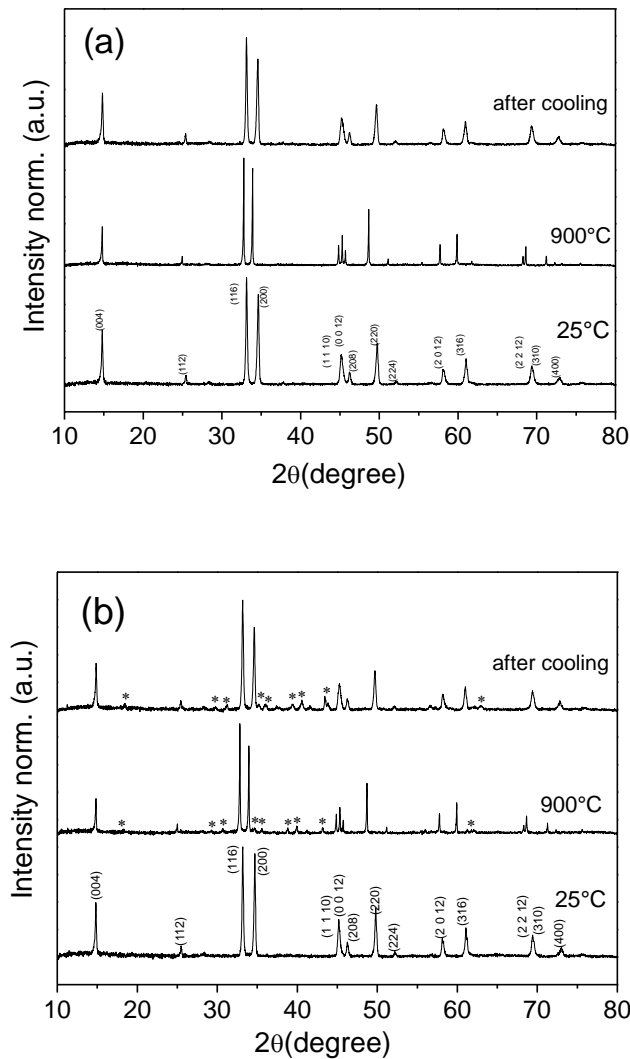


Figure 3.3: XRD pattern of $\mu\text{-Ca}_2\text{MnO}_4$ (a) and $\mu\text{-Ca}_2\text{MnO}_4\text{-25\%Ca-extr}$ (b) before heating, at 900°C and after cooling. The peaks corresponding to the impurity phases are marked with asterisks.

No phase transitions or evolution of impurity phases were observed. Aside from an expected shift in diffraction-peak position due to thermal expansion, the patterns were identical before, during, and after heating (Figure 3.3(a)).

The diffraction pattern of the $\mu\text{-Ca}_2\text{MnO}_4\text{-25\%Ca-extr}$ compound unmistakably showed the formation of additionally $\text{Ca}_2\text{Mn}_2\text{O}_5$, CaMn_2O_4 and Mn_2O_3 phases starting at around $T=800^\circ\text{C}$, which remain present upon cooling (Figure 3.3(b)). The diffraction peaks of $\mu\text{-Ca}_2\text{MnO}_4$ were not influenced by the formation of these phases during the heating and cooling process indicating that the impurity phases crystallized from the amorphous component present in the sample were not detectable by RT-XRD. These phases have a lower Ca/Mn stoichiometric ratio than the pristine compound indicating calcium losses upon the acid treatment.

Thermal analysis was performed for the $\mu\text{-Ca}_2\text{MnO}_4\text{-25\%Ca-extr}$ compound (Figure 3.4) to specify the volatile H_2O -related species possibly intercalated into the sample crystal structure during the Ca^{2+} extraction process.

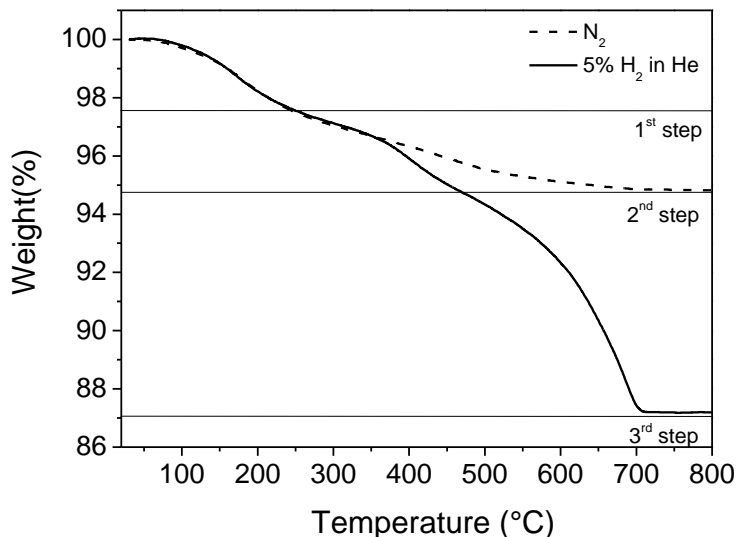


Figure 3.4: Relative weight loss with respect to T of the $\mu\text{-Ca}_2\text{MnO}_4\text{-25\%Ca-extr}$ compound under N_2 and 5% H_2 in He atmospheres.

Under N_2 a two-step weight loss associated with an extraction of H_2O was observed between $T = 100\text{ }^\circ\text{C}$ and $600\text{ }^\circ\text{C}$, while under 5% H_2 in He a third step is added, related to the reduction of the sample into $\text{Ca}_{1-x}\text{Mn}_x\text{O}$. The first step terminates at $230\text{ }^\circ\text{C}$ regardless the employed atmosphere, implying the accommodated species to be a coordinated H_2O . The second weight-loss step, on the other hand, appears to be facilitated under the reductive atmosphere, which is understood on the basis of the easier convertibility of the OH^- species into extractable H_2O in the presence of H_2 (g). Similar observations of the decomposition behaviour were made by others for the MnO_2 hydrate prepared reducing NaMnO_4 in an aqueous solution of fumaric acid and H_2SO_4 [90]. In the case of MnO_2 the first weight reduction from the as-prepared compound concluding at slightly higher temperature was understood as the extraction of crystal water, while the second step was considered to be related with oxygen extraction due to conversion of the MnO_2 into Mn_2O_3 .

SEM images of the samples (Figure 3.5) showed that the microstructure of pristine $\mu\text{-Ca}_2\text{MnO}_4$ and acid-treated samples consisted of agglomerates of irregularly shaped particles smaller than 1 micron. The morphology of higher calcium extraction samples ($>50\text{at\%}$) was altered. Additional roughness on the surface of the samples was observed. In general, the agglomerates and particle dimensions were similar before and after acid treatment.

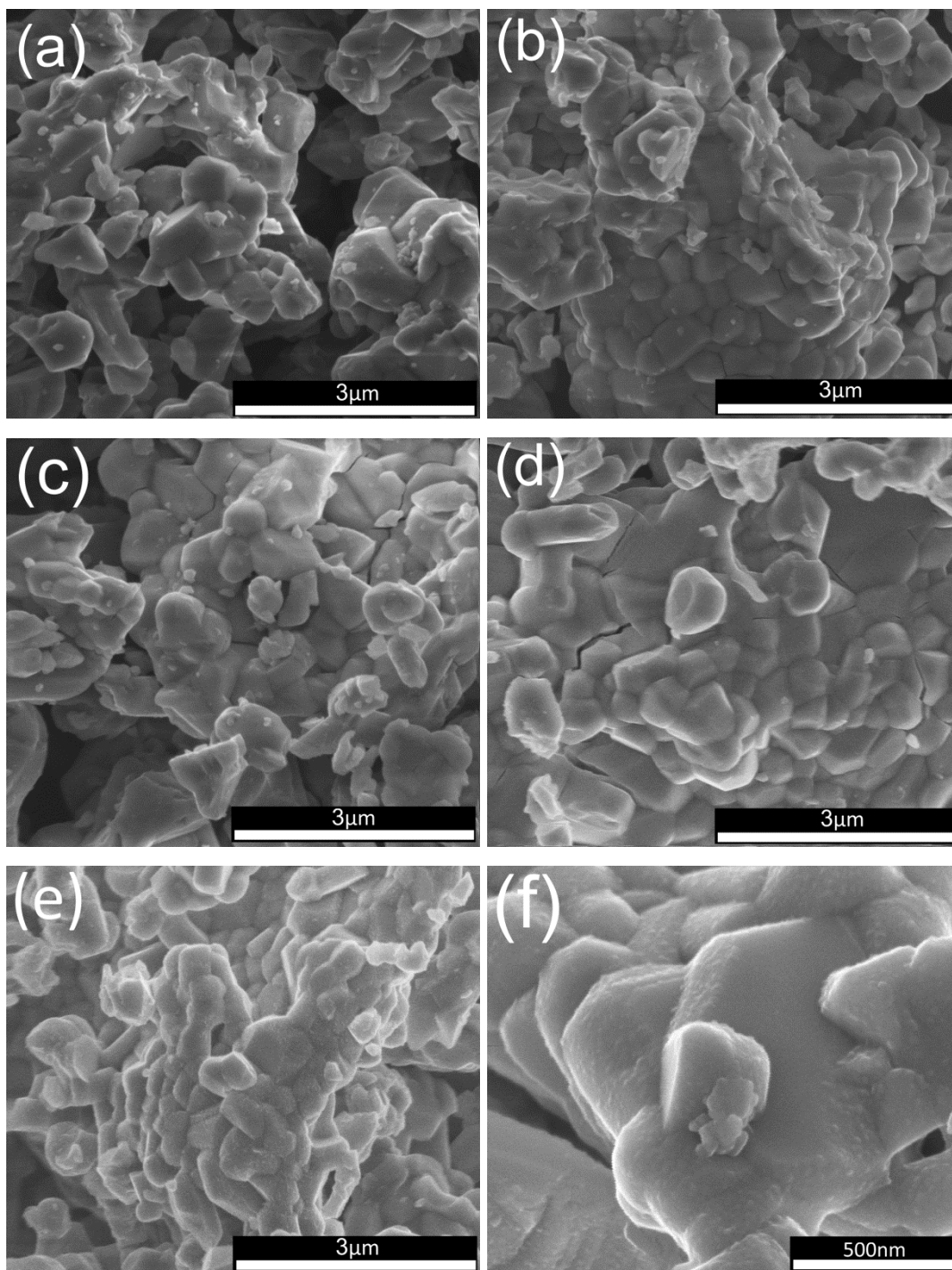


Figure 3.5: SEM images of $\mu\text{-Ca}_2\text{MnO}_4$ pristine (a), $\mu\text{-Ca}_2\text{MnO}_4\text{-25%Ca-extr}$ (b), $\mu\text{-Ca}_2\text{MnO}_4\text{-50%Ca-extr}$ (c), $\mu\text{-Ca}_2\text{MnO}_4\text{-75%Ca-extr}$ (d), $\mu\text{-Ca}_2\text{MnO}_4\text{-90%Ca-extr}$ (e), high magnification of $\mu\text{-Ca}_2\text{MnO}_4\text{-75%Ca-extr}$.

Local chemical compositions were obtained by SEM/EDX. EDX spectra were recorded in different zones of the samples. Qualitative analysis confirmed the presence of a constant calcium manganese ratio on each spot showing the respective $K\alpha_1$ and $K\beta_1$ lines. Although no chemical inhomogeneity was observed within each sample, a relative quantification of the atomic ratio between calcium and manganese in the pristine and the Ca^{2+} -extracted com-

pounds showed a significant difference. The quantification is in agreement with the theoretical Ca^{2+} extraction calculated from ionic equilibrium. The results are summarized in Table 3.1.

Table 3.1: EDX quantification

Compound	Ca %at	Mn %at	Theoretical ratio Ca:Mn	Experimental ratio Ca:Mn (EDX)
$\mu\text{-Ca}_2\text{MnO}_4$ pristine	67.1±0.3	32.9±0.3	2	2.04
$\mu\text{-Ca}_2\text{MnO}_4\text{-25\%Ca-extr}$	59.2±0.5	40.8±0.5	1.5	1.44
$\mu\text{-Ca}_2\text{MnO}_4\text{-50\%Ca-extr}$	51.7±0.6	48.3±0.6	1	1.07
$\mu\text{-Ca}_2\text{MnO}_4\text{-75\%Ca-extr}$	34.7±0.5	65.7±0.5	0.5	0.53
$\mu\text{-Ca}_2\text{MnO}_4\text{-90\%Ca-extr}$	14.5±0.3	85.5±0.3	0.2	0.17

DLS measurements were performed on all samples to determine the particle size distribution. The major particle size of between 2 μm and 8 μm was found in all samples. Combined SEM and DLS indicate the samples consist of particles having dimensions of around 1 micron along with larger agglomerates. It was found no difference in particle size as a result of acid treatment.

The TEM images of pristine and $\mu\text{-Ca}_2\text{MnO}_4\text{-50\%Ca-extr}$ compounds are shown in Figure 3.6. The pristine compound consisted of particles with well-defined facets. However, the $\mu\text{-Ca}_2\text{MnO}_4\text{-50\%Ca-extr}$ compound had a rough surface suggesting that an amorphous coverage was formed. This result was in agreement with SEM characterisation.

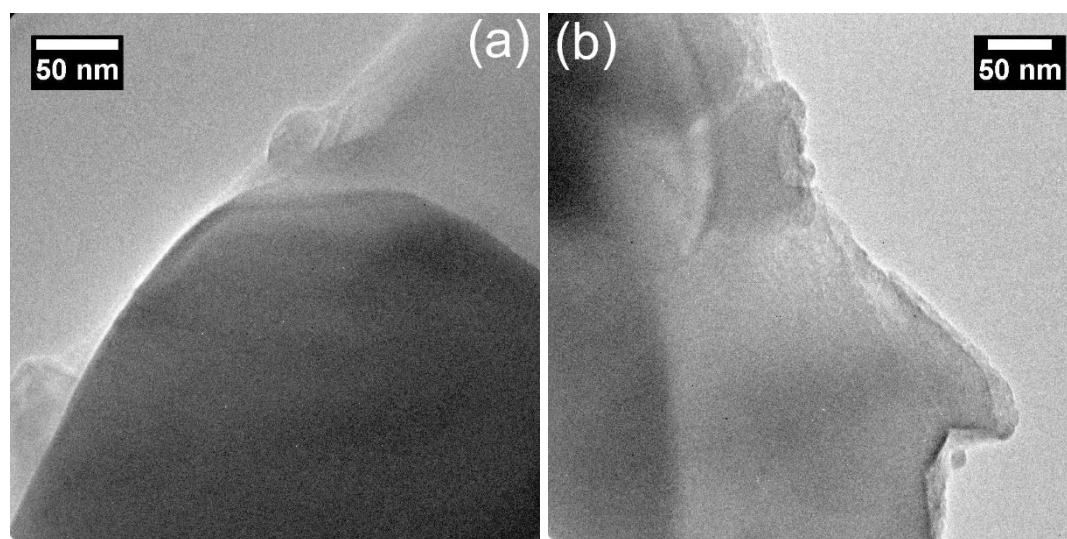


Figure 3.6: TEM images of $\mu\text{-Ca}_2\text{MnO}_4$ pristine (a) and $\mu\text{-Ca}_2\text{MnO}_4\text{-50\%Ca-extr}$ (b).

Raman spectra were recorded on all samples to clarify the composition of the amorphous coverage (Figure 3.7).

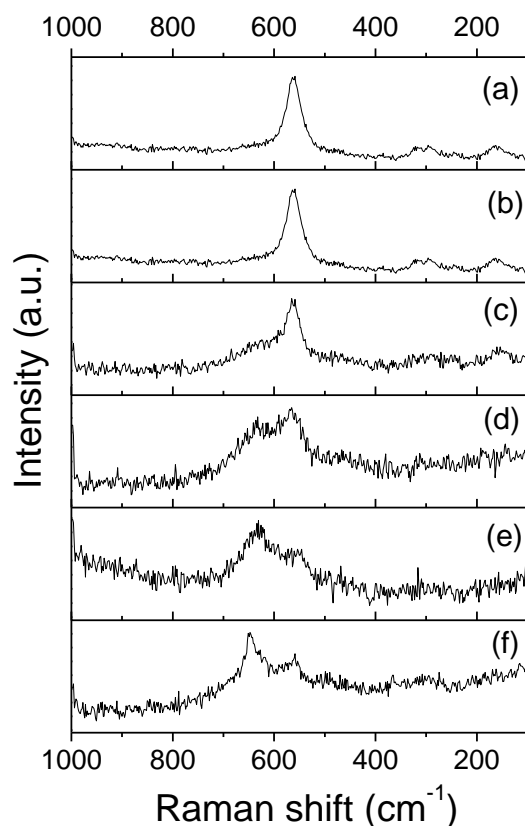


Figure 3.7: Raman spectra of $\mu\text{-Ca}_2\text{MnO}_4$ pristine (a), $\mu\text{-Ca}_2\text{MnO}_4\text{-25\%Ca-extr}$ (b), $\mu\text{-Ca}_2\text{MnO}_4\text{-50\%Ca-extr}$ (c), $\mu\text{-Ca}_2\text{MnO}_4\text{-75\%Ca-extr}$ (d), $\mu\text{-Ca}_2\text{MnO}_4\text{-90\%Ca-extr}$ (e) and amorphous $\text{MnO}_2 \cdot x\text{H}_2\text{O}$ (f).

The spectrum of pristine $\mu\text{-Ca}_2\text{MnO}_4$ (Figure 3.7(a)) showed a main peak centred at 560 cm^{-1} related to the $\nu(\text{Mn-O})$ stretching vibration of Mn^{4+} in O_h coordination and small peaks between 180 cm^{-1} and 400 cm^{-1} related to skeletal vibrations [91]. The two main peaks centered at 630 cm^{-1} and 560 cm^{-1} in the hydrated amorphous MnO_2 spectrum were also due to the $\nu(\text{Mn-O})$ stretching vibration of Mn^{4+} in O_h coordination [91]. These two spectra can be seen as the end members of the calcium-extracted compound series, while the others represent intermediate states between the two extreme compositions. Looking at Figure 3.7 from the top to the bottom, namely increasing the quantity of extracted calcium, the peak present at 630 cm^{-1} in the MnO_2 spectra was correlated to the MnO_2 content on the compounds with extracted Ca^{2+} . The intensity of the band at 630 cm^{-1} seemed to be directly related to the amount of extracted Ca^{2+} from $\mu\text{-Ca}_2\text{MnO}_4$.

To summarize, the calcium deficiency was a function of the amount of acid used in the reaction as confirmed by SEM/EDX measurements, while XRD confirmed the presence of the

pristine Ca_2MnO_4 phase. The deficiency was indirectly confirmed in HT-XRD by the formation of new phases with Ca/Mn ratios lower than in the pristine material after heating up at around 800 °C. They were attributed to two factors: 1) the reduction of MnO_2 to Mn_2O_3 and 2) the enhanced diffusion of calcium from the Ca-rich phase to the manganese oxide at high temperature. An amorphous hydrated manganese dioxide $\text{MnO}_2 \cdot x\text{H}_2\text{O}$ coverage was identified by Raman spectroscopy. The lower intensity of the $\mu\text{-Ca}_2\text{MnO}_4\text{-75\%Ca-extr}$ and $\mu\text{-Ca}_2\text{MnO}_4\text{-90\%Ca-extr}$ reflections in the XRD pattern was attributed to a decrease of the crystalline primary phase in the centre of the particles as a consequence of formation of the outer amorphous layer. The amorphization of the surface was observed also by TEM and by SEM for high calcium extraction.

The overall characterization carried out on acid-treated samples revealed the presence of an amorphous material distributed uniformly on the surface of the crystalline particles. This treatment attacked the surface of the particles, but the global morphology was preserved. The removal of calcium and consequently of oxygen provoked a collapse of the structure with a loss of the long range order in the surface layers, while the crystallinity of the bulk remained the same as in the pristine materials.

Electrochemical measurements were carried out to study the lithium intercalation in the acid-treated compounds. The first galvanostatic cycle for all compounds is shown in Figure 3.8.

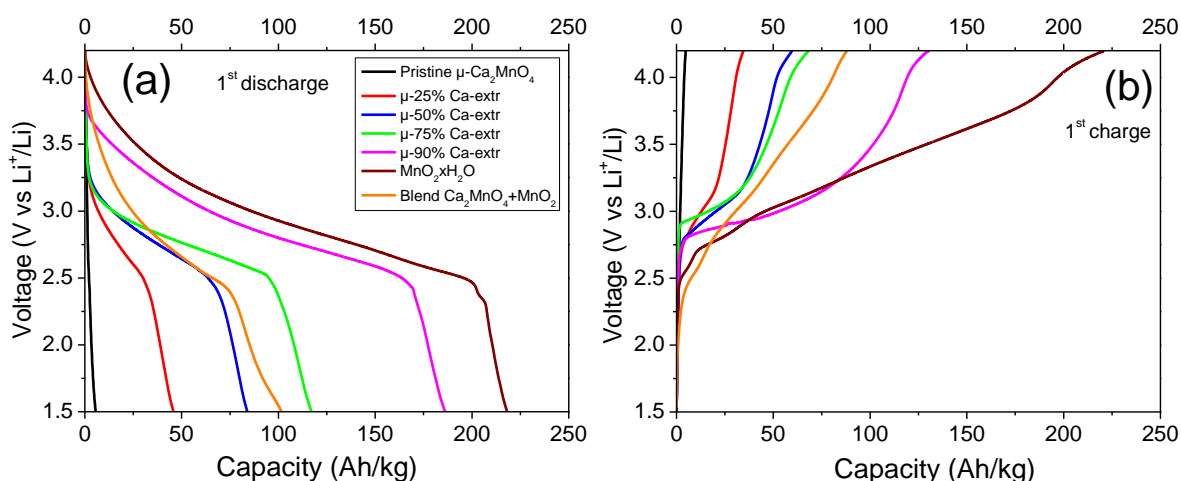


Figure 3.8: Discharge (a) and charge (b) profile for the 1st cycle between 1.5 V and 4.2 V at 10A/kg of $\mu\text{-Ca}_2\text{MnO}_4$ pristine (black), $\mu\text{-Ca}_2\text{MnO}_4\text{-25\%Ca-extr}$ (red), $\mu\text{-Ca}_2\text{MnO}_4\text{-50\%Ca-extr}$ (blue), $\mu\text{-Ca}_2\text{MnO}_4\text{-75\%Ca-extr}$ (green), $\mu\text{-Ca}_2\text{MnO}_4\text{-90\%Ca-extr}$ (magenta), amorphous $\text{MnO}_2 \cdot x\text{H}_2\text{O}$ (brown) and $\mu\text{-Ca}_2\text{MnO}_4/\text{MnO}_2 \cdot x\text{H}_2\text{O}$ blend (orange).

The pristine compound showed negligible electrochemical activity in the selected potential range. Although a discharge capacity of around 4 Ah/kg was measured, it is unlikely due to an intercalation reaction. All the acid-treated compounds showed identical discharge profile, but a different capacity depending on the amount of calcium extracted. An approximate discharge capacity of 40 Ah/kg could be achieved for each 25 at% calcium extraction. The lithium intercalation is reversible. During charging, roughly 30 Ah/kg can be deintercalated for each 25 at% calcium extracted material. The shape of the charge curve is similar for all acid-treated compounds. Upon charging, the measured capacity value is in good agreement with the dependency on the amount of calcium extracted, as observed during the discharge. A large difference between the first and second discharge was measured and capacity losses between 20% and 40% were observed for all compounds (Table 3.2). This behaviour was more prominent when increasing the calcium extraction and was also present in amorphous manganese oxide.

The 30th cycle was selected for comparison with the 1st cycle since all samples have reached the maximum of coulombic efficiency (>95%) and showed stable capacity values in the following cycles (Figure 3.9). The discharge and charge curves show the amorphous-like profile as observed during the 1st cycle. The lithium intercalation is still reversible. The capacities are lower than at the 1st cycle although in accordance with the amount of calcium extracted.

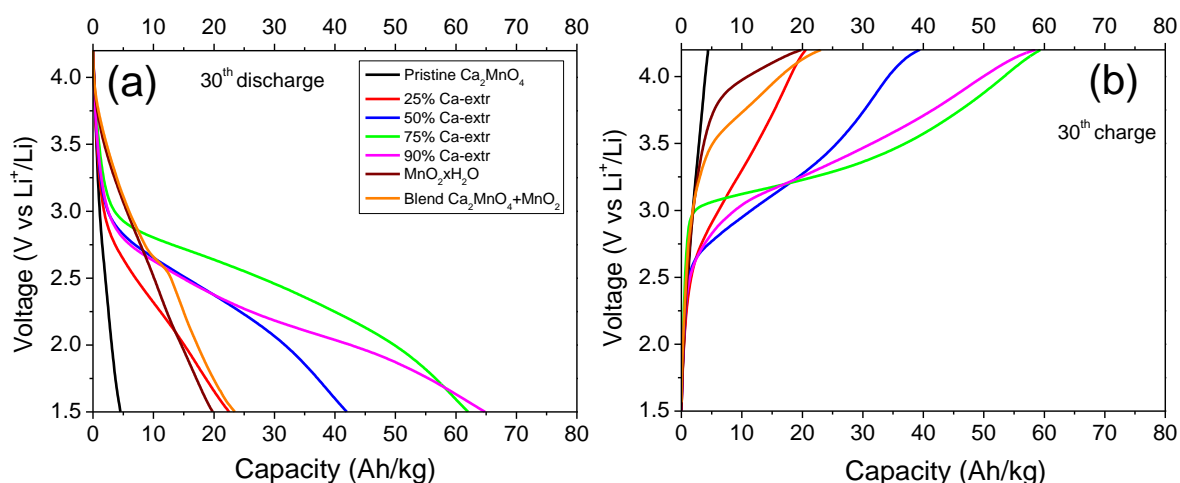


Figure 3.9: Discharge (a) and charge (b) profile for the 30th cycle between 1.5 V and 4.2 V at 10A/kg of μ -Ca₂MnO₄ pristine (black), μ -Ca₂MnO₄-25% Ca-extr (red), μ -Ca₂MnO₄-50% Ca-extr (blue), μ -Ca₂MnO₄-75% Ca-extr (green), μ -Ca₂MnO₄-90% Ca-extr (magenta), amorphous MnO₂·xH₂O (brown) and μ -Ca₂MnO₄/MnO₂·xH₂O blend (orange).

A plot of discharge capacity vs. number of cycles for all compounds is shown in Figure 3.10(a).

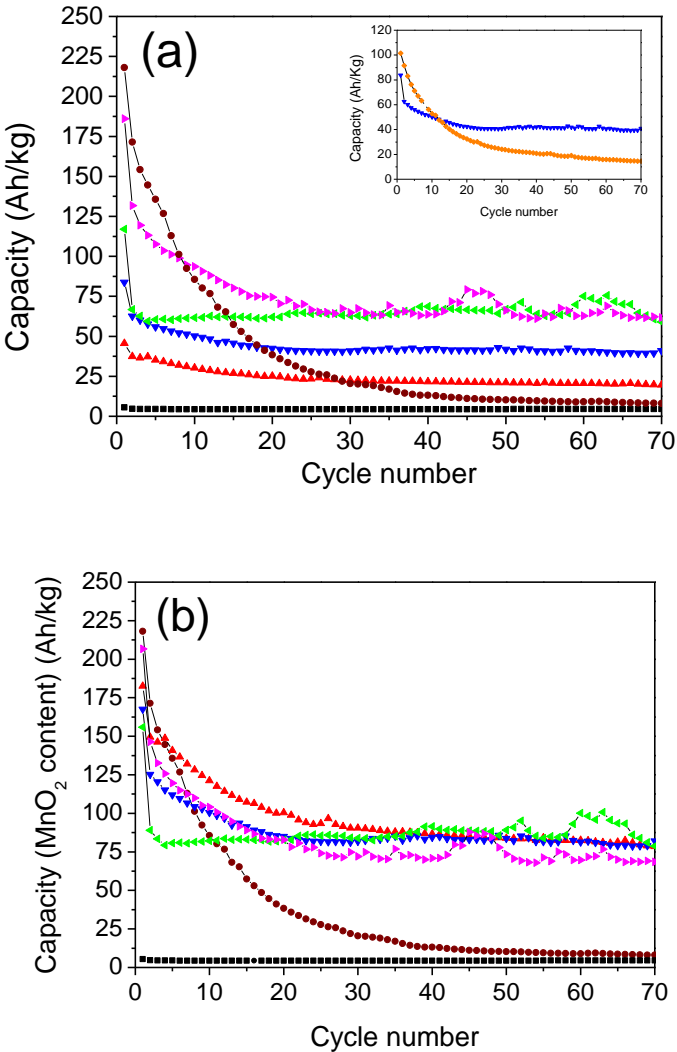


Figure 3.10: (a) Discharge capacity vs cycle at 10A/kg of $\mu\text{-Ca}_2\text{MnO}_4$ pristine (■, black), $\mu\text{-Ca}_2\text{MnO}_4$ -25%Ca-extr (▲, red), $\mu\text{-Ca}_2\text{MnO}_4$ -50%Ca-extr (▼, blue), $\mu\text{-Ca}_2\text{MnO}_4$ -75%Ca-extr (◄, green), $\mu\text{-Ca}_2\text{MnO}_4$ -90%Ca-extr (►, magenta) and amorphous $\text{MnO}_2 \cdot x\text{H}_2\text{O}$ (●, brown). Inset: cathodic specific charge vs cycle of $\mu\text{-Ca}_2\text{MnO}_4$ -50%Ca-extr (▼, blue) and $\mu\text{-Ca}_2\text{MnO}_4/\text{MnO}_2 \cdot x\text{H}_2\text{O}$ blend (◆, orange). (b) Discharge capacity vs cycle normalized to MnO_2 content for all compounds.

A very fast degradation occurred for amorphous manganese oxide $\text{MnO}_2 \cdot x\text{H}_2\text{O}$. The capacity retention on this compound after 35 cycles was almost zero. As for the calcium-extracted compounds, they reached the stability after 30 cycles delivering a capacity of ca. 20 Ah/kg for $\mu\text{-Ca}_2\text{MnO}_4$ -25%Ca-extr, 40 Ah/kg for $\mu\text{-Ca}_2\text{MnO}_4$ -50%Ca-extr and 60 Ah/kg for both $\mu\text{-Ca}_2\text{MnO}_4$ -75%Ca-extr and $\mu\text{-Ca}_2\text{MnO}_4$ -90%Ca-extr. The capacity for lithium-ion intercala-

tion on the Ca-deficient compounds was lower when compared to the initial value of amorphous $\text{MnO}_2 \cdot x\text{H}_2\text{O}$, while the capacity retention under cycling was significantly improved. Aiming to better understand the stabilizing effect of the crystalline core of the acid treated compounds under cycling, a blend was prepared by mixing pristine $\mu\text{-Ca}_2\text{MnO}_4$ and $\text{MnO}_2 \cdot x\text{H}_2\text{O}$ for comparison. The inset in Figure 3.10(a) shows the plot of discharge capacity vs. number of cycles considering only $\mu\text{-Ca}_2\text{MnO}_4\text{-50\%Ca-extr}$ and the $\mu\text{-Ca}_2\text{MnO}_4/\text{MnO}_2 \cdot x\text{H}_2\text{O}$ blend. As expected the discharge capacity of the blend electrode during the first discharge was almost half of the pure $\text{MnO}_2 \cdot x\text{H}_2\text{O}$ since only half of manganese was electrochemically active. The degradation of the blend followed the same trend of $\text{MnO}_2 \cdot x\text{H}_2\text{O}$ and the capacity retention was much lower than $\mu\text{-Ca}_2\text{MnO}_4\text{-50\%Ca-extr}$. The analysis of the electrochemical results for all compounds is summarized in Table 3.2.

Table 3.2: Resume of the electrochemical data for all compounds

Compound	Specific Charge [Ah/kg]		% Specific charge lost between 1 st and 2 nd cycle	% Capacity retention after 70 cycles
	1 st cycle discharge	70 th cycle discharge		
$\mu\text{-Ca}_2\text{MnO}_4$ pristine	4	4	n.d	n.d
$\mu\text{-Ca}_2\text{MnO}_4\text{-25\%Ca-extr}$	45	20	18	44
$\mu\text{-Ca}_2\text{MnO}_4\text{-50\%Ca-extr}$	85	41	25	48
$\mu\text{-Ca}_2\text{MnO}_4\text{-75\%Ca-extr}$	117	59	43	50
$\mu\text{-Ca}_2\text{MnO}_4\text{-90\%Ca-extr}$	185	61	29	33
$\text{MnO}_2 \cdot x\text{H}_2\text{O}$	220	8	21	4
Blend $\mu\text{-Ca}_2\text{MnO}_4 + \text{MnO}_2 \cdot x\text{H}_2\text{O}$	102	15	10	15

In Figure 3.10(b) the same data were plotted assuming that only the percentage of calcium extracted material gave rise to electrochemical activity. The compounds having 25at%, 50at%, 75at% and 90at% Ca extraction, normalized to 100at% MnO_2 -content, showed a stable discharge capacity around 90-100 Ah/kg over 70 cycles.

Taking into account the characterization and the electrochemical measurements discussed above, the following model was proposed to explain the electrochemical behaviour: the acid treatment removed calcium oxide from the samples leaving a crystalline bulk of $\mu\text{-Ca}_2\text{MnO}_4$ covered with an amorphous $\text{MnO}_2 \cdot x\text{H}_2\text{O}$ layer. XRD measurements on compounds obtained

after electrochemical cycling revealed that the crystal structure of the crystalline part of the sample did not change (Fig. 3.11). Since no differences were observed in the XRD pattern before and after battery cycling, we conclude that lithium ion intercalation occurs only into the amorphous structure formed on the surface.

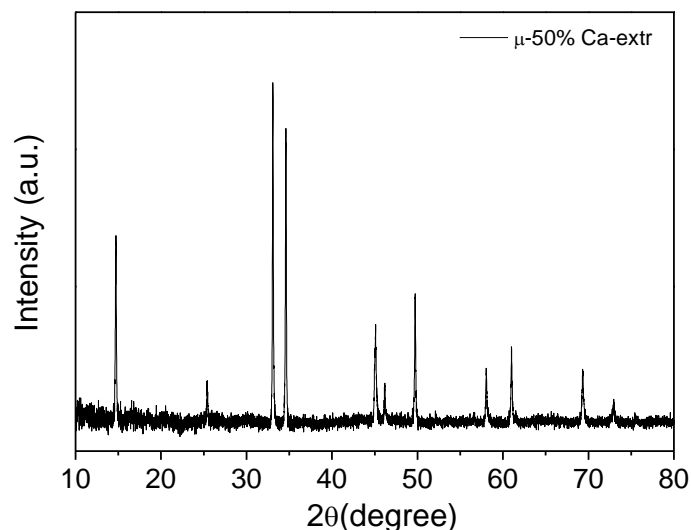


Figure 3.11: XRD pattern of $\mu\text{-Ca}_2\text{MnO}_4\text{-50\%Ca-extr}$ after 70 cycles.

Higher calcium extraction causes a higher quantity of manganese oxide on the surface of the particles and therefore more available sites for lithium ion intercalation. The electrochemical activity data of the first cycle confirmed the structural finding that the active compound consisted of amorphous $\text{MnO}_2 \cdot x\text{H}_2\text{O}$ (Figure 3.10b). However, the crystalline bulk appeared to have a stabilizing influence on the capacity retention under cycling. A considerable improvement of the stability was noticed on the Ca-extracted compounds, compared to bare amorphous $\text{MnO}_2 \cdot x\text{H}_2\text{O}$ and the $\mu\text{-Ca}_2\text{MnO}_4/\text{MnO}_2 \cdot x\text{H}_2\text{O}$ blend.

The functionalization of the surfaces of the particles obtained by controlled calcium extraction was synthesis-dependent and cannot be obtained by mixing the two different materials having different properties. With this bifunctional crystalline-amorphous structure, composed by a $\mu\text{-Ca}_2\text{MnO}_4$ bulk phase for the stability and an amorphous $\text{MnO}_2 \cdot x\text{H}_2\text{O}$ surface for the electrochemical response, it was possible to reach a stability improvement by a factor of 10. After 70 cycles this structure was still stable and capacity retention around 35%-50% is reached for all compounds. This new structure leads to an increased stability during charge and discharge cycling of amorphous $\text{MnO}_2 \cdot x\text{H}_2\text{O}$ as a host for lithium intercalation in Li-ion battery cathodes.

3.3 Acid treatment of n-Ca₂MnO₄: influence of the particle size and comparison with μ-Ca₂MnO₄

In the previous subchapter Ca₂MnO₄ having micron-sized particles has been already synthesized, modified for lithium intercalation, and characterized electrochemically. It is well known, however, that lowering the particle size increases the electrode/electrolyte contact area improving total capacity and rate capability [92], especially in materials with low conductivity. For this reason, Ca₂MnO₄ was synthesized as nanoparticles and subsequently activated removing calcium ions from the surface of the samples by acid treatment similar to the treatment described in subchapter 3.2.

The activation of n-Ca₂MnO₄ towards lithium intercalation was performed in two steps. In the first step, nanoparticles of Ca₂MnO₄ were obtained by Pechini method. Synthesis parameters as C_M (CA to metal ratio) and C_E (CA to EG ratio) [93] and calcination temperature were set to obtain the smallest particle size possible. In the second step, n-Ca₂MnO₄ was treated with H₂SO₄.

The XRD patterns of the pristine n-Ca₂MnO₄ and the Ca²⁺-extracted compounds are shown in Fig. 3.12. All reflections in Fig. 1(a) were indexed with the Ca₂MnO₄, K₂NiF₄-type structure. The XRD patterns of all Ca²⁺-extracted compounds revealed no 2θ-shift in comparison to the pristine compound. However, a decrease in crystallinity and consequently of the peak intensities can be observed for n-Ca₂MnO₄-50%Ca-extr and n-Ca₂MnO₄-75%Ca-extr.

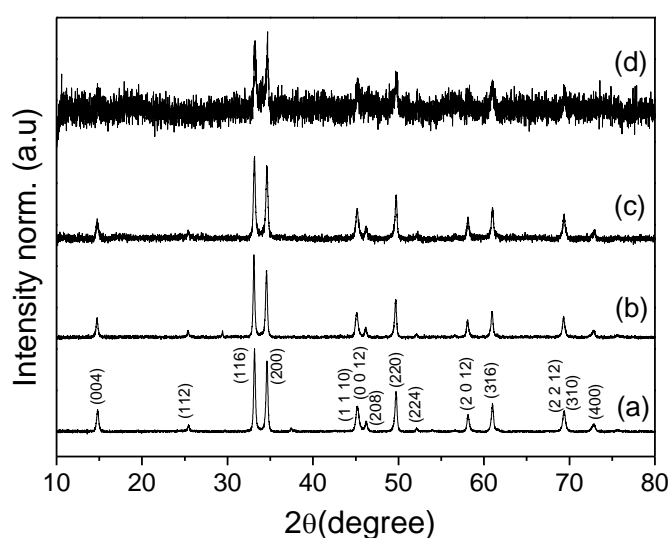


Figure 3.12: XRD patterns of Ca₂MnO₄ pristine (a), Ca₂MnO₄-25%Ca-extr (b), Ca₂MnO₄-50%Ca-extr (c), and Ca₂MnO₄-75%Ca-extr (d).

Figure 3.13 shows the SEM micrograph of the pristine $n\text{-Ca}_2\text{MnO}_4$. It is composed of nanoparticles having irregular shape and dimension between 50 and 100 nm. EDX spectra were recorded in different zones of the samples. Quantitative analysis showed a Ca to Mn ratio in very good agreement with the theoretical one (Table 1) highlighting the occurred calcium extraction. SEM micrographs of the Ca^{2+} -extracted compound showed a higher degree of agglomeration but no changes in overall particles dimension.

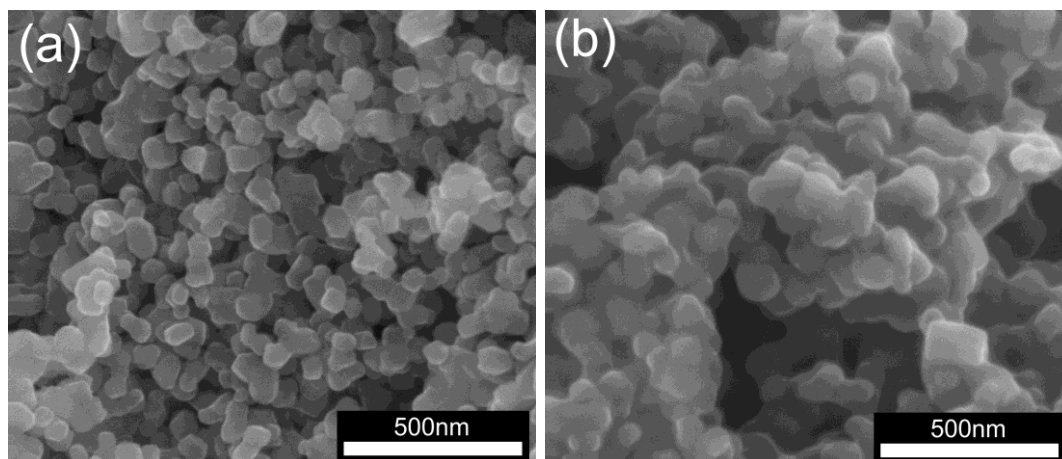


Figure 3.13: SEM micrographs of (a) $n\text{-Ca}_2\text{MnO}_4$ pristine and (b) $n\text{-Ca}_2\text{MnO}_4$ -50% Ca-extr.

Table 3.3: EDX quantification.

Compound	Ca %at	Mn %at	Theoretical ratio Ca:Mn	Experimental ratio Ca:Mn (EDX)
$n\text{-Ca}_2\text{MnO}_4$ pristine	67.5±0.5	32.5±0.5	2	2.08
$n\text{-Ca}_2\text{MnO}_4$-25% Ca-extr	60.4±0.5	39.6±0.5	1.5	1.52
$n\text{-Ca}_2\text{MnO}_4$-50% Ca-extr	50.0±0.6	50.0±0.6	1	1
$n\text{-Ca}_2\text{MnO}_4$-75% Ca-extr	33.0±0.6	67.0±0.6	0.5	0.49

TEM images of pristine and $n\text{-Ca}_2\text{MnO}_4$ -50%Ca-extr compound are shown in Fig.3.14. $n\text{-Ca}_2\text{MnO}_4$ was composed of crystalline nanoparticles. Lattice planes could be clearly identified up to the surface of the particles. On the other side, $n\text{-Ca}_2\text{MnO}_4$ -50%Ca-extr particles showed an inner crystalline bulk and an amorphous outer layer separated by a well-defined interface.

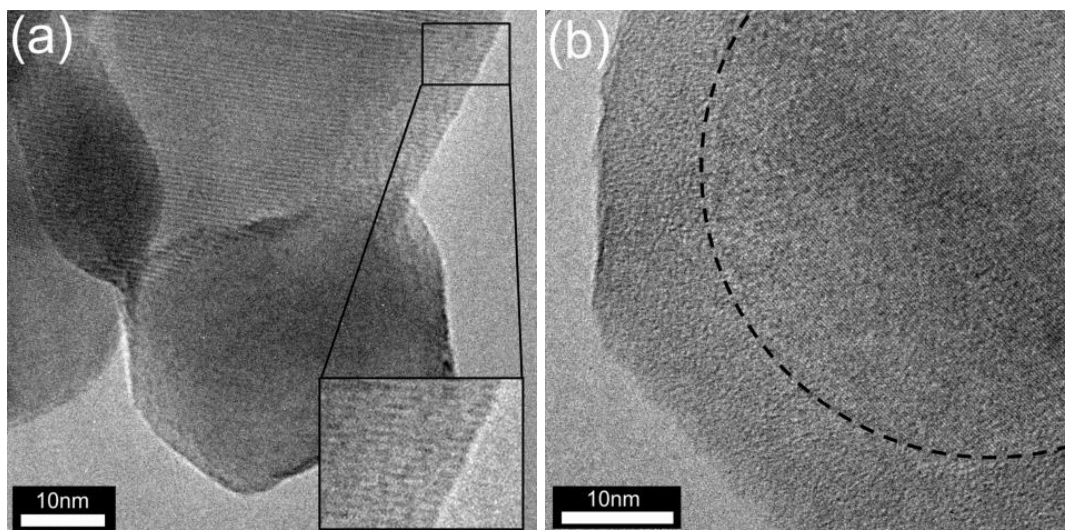


Figure 3.14: TEM images of (a) $n\text{-Ca}_2\text{MnO}_4\text{Ca-extr}$ pristine and (b) $n\text{-Ca}_2\text{MnO}_4\text{-50\%Ca-extr}$.

Line scan EDX analysis was carried out by STEM/EDX to study the change of the Ca:Mn ratio in the outer amorphous layer and in the inner crystalline bulk (Fig. 3.15). The Ca:Mn ratio in the outer layer was approximately 0.6 with a composition of Ca 37.5 at% and Mn 62.5 at%. The Ca:Mn ratio changed abruptly in the first 15 nm approach to 1.7 when the inner bulk was reached (Ca 62.5 at% and Mn 37.5 at%). The experimental Mn content of the inner bulk was lightly underestimated due to 3D effect of the measurements but still close to the theoretical value. These results indicate that the inner bulk is constituted of Ca_2MnO_4 and the calcium extraction involved the surface of the particles.

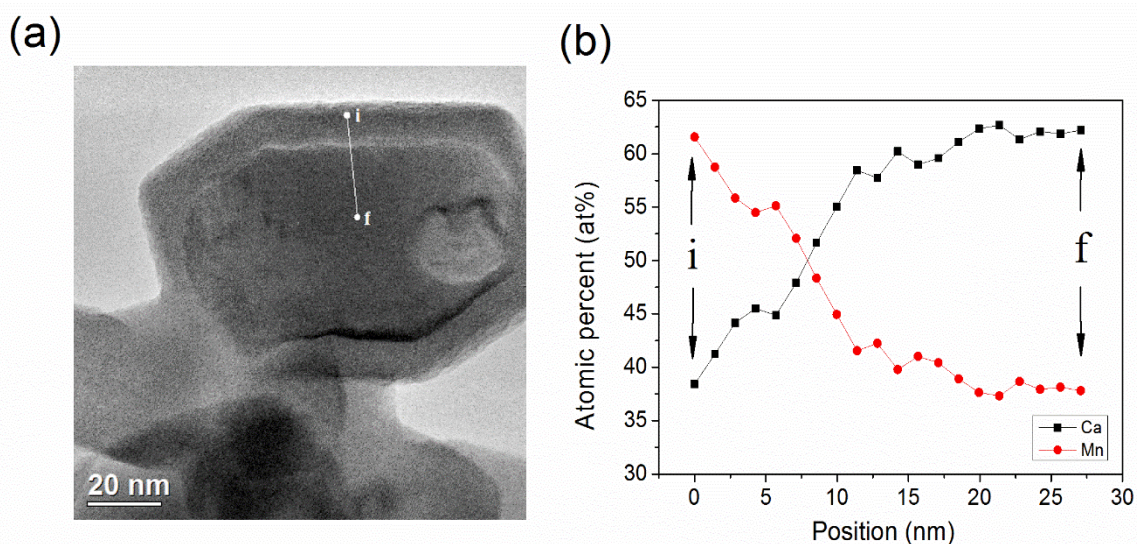


Figure 3.15: (a) BF-STEM image of $n\text{-Ca}_2\text{MnO}_4\text{-50\%Ca-extr}$ and (b) line scan EDX quantification.

The calcium extraction, as confirmed by SEM/EDX and STEM/EDX, should theoretically give rise to manganese oxide with formula Ca_xMnO_2 on the surface of the samples. To determine the composition of the amorphous outer layer, Raman measurements were carried out on all samples (Fig.3.16). Amorphous hydrated manganese oxide ($\text{MnO}_2 \cdot x\text{H}_2\text{O}$) was synthesized for comparison. The spectrum of pristine $n\text{-Ca}_2\text{MnO}_4$ showed a main peak centered at 560 cm^{-1} related to the $\nu(\text{Mn-O})$ stretching vibration of Mn^{4+} in O_h coordination and small peaks between 180 cm^{-1} and 400 cm^{-1} related to skeletal vibrations [94].

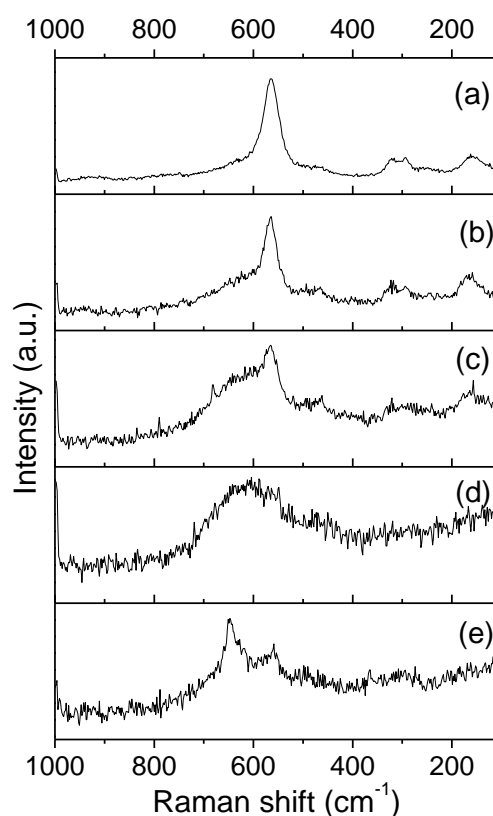


Figure 3.16: Raman spectra of $n\text{-Ca}_2\text{MnO}_4$ pristine (a), $n\text{-Ca}_2\text{MnO}_4$ -25%Ca-extr (b), $n\text{-Ca}_2\text{MnO}_4$ -50%Ca-extr (c), $n\text{-Ca}_2\text{MnO}_4$ -75%Ca-extr (d) and $\text{MnO}_2 \cdot x\text{H}_2\text{O}$.

Increasing the calcium extraction, namely increasing the amount of amorphous material on the surface of the samples, a shoulder started to appear around 630 cm^{-1} . This shoulder was correlated to the peak present at 630 cm^{-1} in the $\text{MnO}_2 \cdot x\text{H}_2\text{O}$ reference spectra. The intensity of the band at 630 cm^{-1} correlated well with the amount of extracted Ca^{2+} from Ca_2MnO_4 therefore to the amount of $\text{MnO}_2 \cdot x\text{H}_2\text{O}$ on the surface of the samples.

Lithium intercalation was studied by galvanostatic measurements at 10 Ah/kg and the results were compared with amorphous hydrated MnO_2 . The voltage profile for the first discharge of the pristine $n\text{-Ca}_2\text{MnO}_4$ and the Ca^{2+} -extracted compound is shown in Fig.3.17(a). Ca_2MnO_4

shows a discharge capacity of 24 Ah/kg which is probably due to capacitive charge on the surface of the particles. All the Ca^{2+} -extracted compounds showed an identical discharge profile with a voltage onset around 3.5 V, and an intercalation voltage between 3.5 V and 2.5 V. The capacity depended on the amount of calcium extracted: an approximate discharge capacity of 50 Ah/kg could be achieved for each 25 at.% calcium extraction. Ca^{2+} -extracted compounds and amorphous $\text{MnO}_2 \cdot x\text{H}_2\text{O}$ have the same discharge profile. For this reason the active compound was identified as $\text{MnO}_2 \cdot x\text{H}_2\text{O}$.

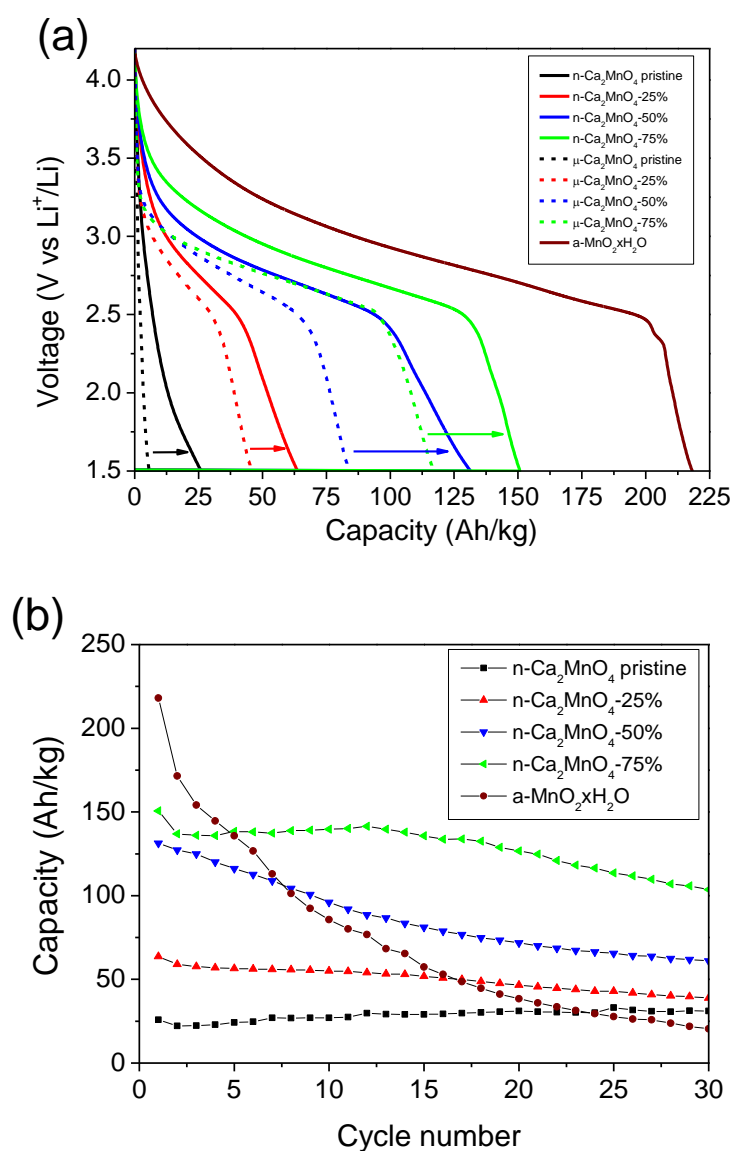


Figure 3.17: Discharge profile (a) for the 1st cycle between 1.5 V and 4.2 V at 10 A/kg and discharge capacity vs cycles graph (b) of n- Ca_2MnO_4 pristine (black), n- Ca_2MnO_4 -25% (red), n- Ca_2MnO_4 -50% (blue), n- Ca_2MnO_4 -75% (green) and amorphous $\text{MnO}_2 \cdot x\text{H}_2\text{O}$ (brown).

The stability of the compounds was studied over 30 cycles (Fig.3.17(b)). As can be seen from Fig. 3.17b the acid treatment significantly improved capacity retention (Table 3.4). n-Ca₂MnO₄-25%Ca-extr, n-Ca₂MnO₄-50%Ca-extr and n-Ca₂MnO₄-75%Ca-extr delivered 46, 60 and 70 Ah/kg respectively after 30 cycles. Although amorphous hydrated MnO₂ showed higher capacity during the first discharge, it undergoes a very fast degradation during cycling with only 9% capacity retention. XRD was also carried out after cycling and no changes were observed in comparison with the material before cycling.

Table 3.4: Resume of the electrochemical data for all compounds.

Compound	Specific Charge [Ah/kg]		% Capacity retention after 30 cycles
	1 st cycle discharge	30 th cycle discharge	
n-Ca ₂ MnO ₄ pristine	26	31	-
n-Ca ₂ MnO ₄ -25%	64	39	60
n-Ca ₂ MnO ₄ -50%	131	61	46
n-Ca ₂ MnO ₄ -75%	150	104	70
MnO ₂ ·xH ₂ O	220	20	9

The overall physicochemical characterization carried out on pristine and Ca²⁺-extracted compounds revealed a calcium extraction which was a function of the amount of acid used in the synthesis. The Ca²⁺ extraction, simultaneously with O²⁻ extraction, gave rise to an amorphization of the particles surface exposed to the acid, creating an outer amorphous layer of few nanometers. The inner part of the particles was preserved as crystalline Ca₂MnO₄. The interface between amorphous and crystalline part of the particles is sharp and the calcium concentration changes in function of the distance from the surface. The outer layer is probable composed of Ca²⁺-containing amorphous hydrated MnO₂ (Fig. 3.18).

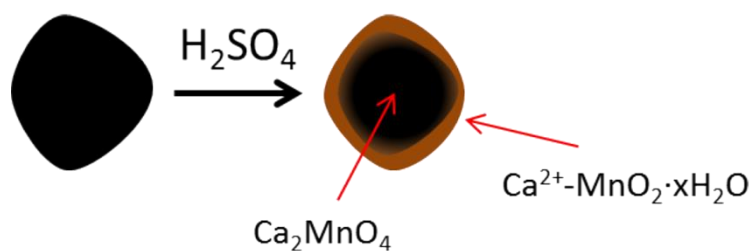


Fig.3.18: Graphical representation of the calcium extracted materials.

Similar results were obtained for Ca_2MnO_4 having micron-sized particles. In that case, the inner crystalline bulk was preserved for calcium extraction up to 90 at%. However, the presence of big agglomerates did not allow for a uniform amorphization of the particle surface.

Taking into account also the electrochemical characterization we explain our findings as follows: lithium intercalation in acid-treated materials occurred only in the amorphous outer layer created on the surface of the particles. The more Ca^{2+} was extracted, the bigger was the amorphous layer and the higher was the capacity of the material. The inner crystalline bulk which was kept intact after acid treatment had a stabilizing influence on capacity retention under cycling. This amorphous-crystalline structure allowed reaching a stability improvement by a factor of 7 in comparison with amorphous $\text{MnO}_2\cdot\text{xH}_2\text{O}$.

$n\text{-Ca}_2\text{MnO}_4$ in comparison with micro- Ca_2MnO_4 showed higher capacity (Fig.3.17a dotted lines) for the same amount of calcium extracted. The capacity improvement was correlated to the particles dimension. Due to the smaller particle size, after the acid treatment, the amorphous electroactive part of the material had a higher surface area exposed to the electrolyte which allowed for a deeper lithiation. At the same time, however, the inner crystalline bulk, which had a stabilizing influence, was much smaller giving rise to lower capacity retention.

Chapter 4

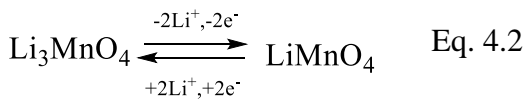
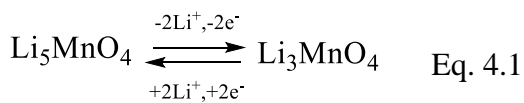
4. Manganese in tetrahedral coordination: Li_3MnO_4 as cathode material.

4.1 Introduction

Recently, Saint et al. [67] proposed the possibility to extend the range of the manganese redox couples used in cathodes to $\text{Mn}^{4+}/\text{Mn}^{5+}$ or even higher, using compounds containing oxyanions MnO_4^{n-} . As described in the introduction, according to ligand field theory (LFT), the extraction of one electron leading to an oxidation state from Mn^{4+} to Mn^{5+} can only occur if the manganese ion is in tetrahedral coordination [67].

One example of material belonging to this class is $\alpha\text{-Li}_3\text{MnO}_4$ (low temperature form) with wurzite-type structure and manganese (V) in tetrahedral coordination [95]. The synthesis of this compound is performed only by solid state reaction at low temperature. The compound is very sensitive to water due to disproportionation of Mn^{5+} to Mn^{4+} and Mn^{7+} and decomposes if exposed to air for 2-3 days, therefore it has to be stored in inert atmosphere.

Theoretical calculations [67] predicted a topotactic intercalation /deintercalation of lithium into Li_3MnO_4 structure following the pathway described in the following reactions (1) and (2):



occurring at 1.9 V and 3.4 V vs Li^+/Li , respectively. The total theoretical capacity for the extraction of four Li eq from Li_5MnO_4 to give LiMnO_4 is 698 Ah/kg which confirms that Li_3MnO_4 is a promising cathode material. A novel synthesis route based on a freeze drying (FD) process was developed with the aim to decrease the number of synthesis steps, enable an easier process for doping the structure and improve the electrochemical properties of Li_3MnO_4 . The FD process, used for many decades in polymer science and technology, is be-

coming widely used in the synthesis of oxides materials for a broad range of applications; including Li-ion battery materials [96-98]. The main advantage of this method is the creation of fine powders with 1) high surface area, 2) small crystallite size and 3) small particle size and agglomerates [99]. These characteristics increase the electroactive area of the material exposed to the electrolyte improving the full lithiation of the particles; decrease the Li^+ pathway promoting a faster lithium intercalation improving electrochemical performances.

The structural, morphological and electrochemical properties of the new freeze dried Li_3MnO_4 are compared to material synthesized by standard solid state reaction.

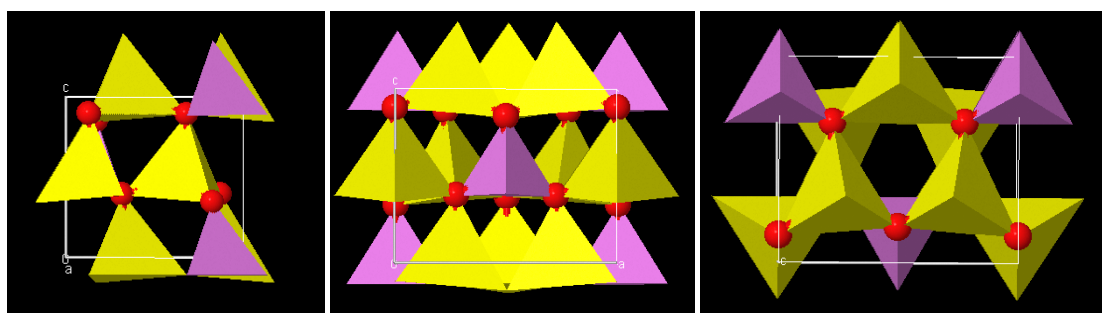
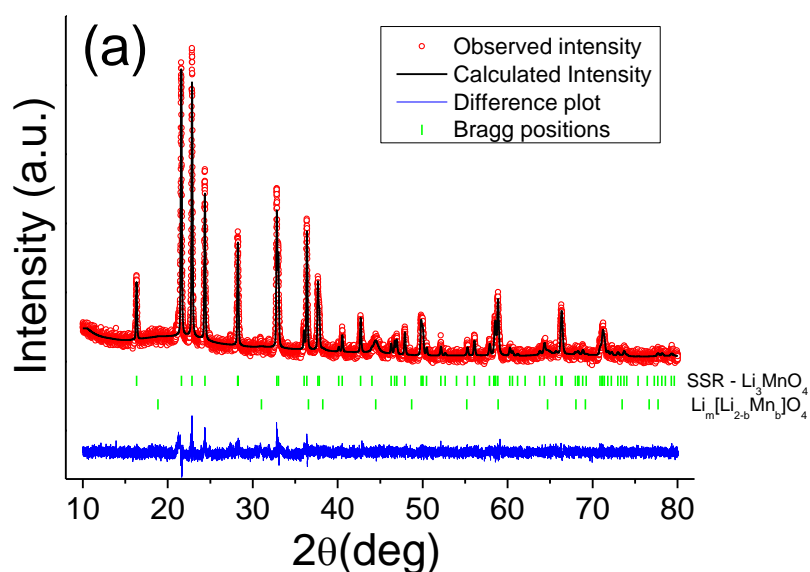


Figure 4.1. Structure of LT- Li_3MnO_4 (yellow tetrahedral (Li), purple tetrahedral (Mn)).

4.2 Characterization of Li_3MnO_4 synthesized by FD

Structural characterization of the compounds obtained by both solid state and freeze drying routes was carried out by XRD. The XRD patterns of SSR- Li_3MnO_4 and FDR- Li_3MnO_4 are shown in Fig. 4.1.



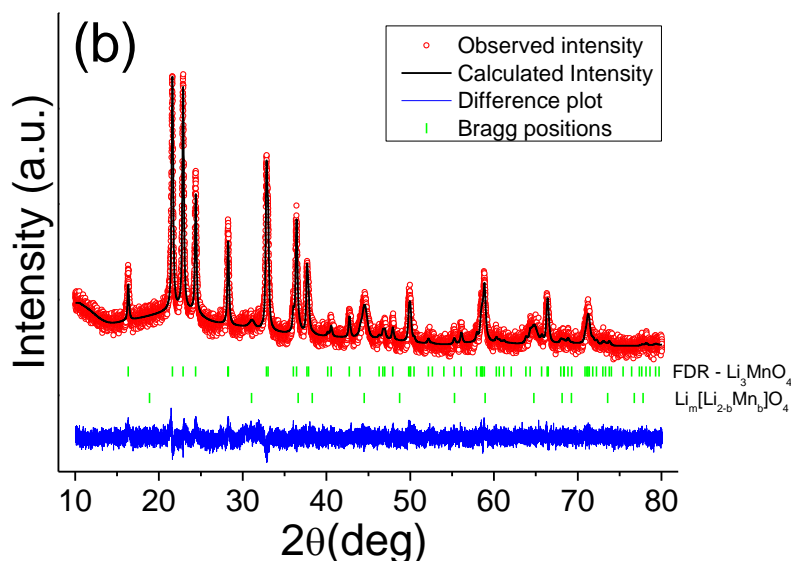


Figure 4.1: XRD pattern with Le Bail fitting plot of (a) SSR-Li₃MnO₄ and (b) FDR-Li₃MnO₄.

The main reflections were indexed with the α -Li₃MnO₄ structure (low temperature form) (JCPDS-PDF 00-032-0572), belonging to the orthorhombic crystal system (space group: Pmn2₁). Small amounts of impurities are present in the samples which are attributed to the decomposition product of lithium permanganate and identified as an over-stoichiometric lithium manganese spinel structure (main peak at 44.8°) with formula Li_m[Li_{2-b}Mn_b]O₄ where $m=(2b-b)>1$. These types of spinels were named “over-stoichiometric”, because the number of Li ions in tetrahedral sites is higher than 1. However, in over-stoichiometric spinels Li ions reside also in octahedral sites [77]. Le Bail fitting was performed to extract the information on lattice parameters and on crystallite size of the compounds as summarized in Table 4.1.

Table 4.1: Le Bail fitting results.

Samples	R _{wp} (%)	R _{exp} (%)	χ ²	a (Å)	b (Å)	c (Å)	Crystallite size (nm)
SSR-Li ₃ MnO ₄	3.40	2.83	1.45	6.3060(2)	5.4218(2)	4.9358(2)	101.3(1)
FDR- Li ₃ MnO ₄	2.71	2.40	1.27	6.3074(2)	5.4212(2)	4.9306(2)	35.5(1)

A slight lattice expansion was observed along the a axis, and a contraction was observed along the b and c axes, for FDR- Li₃MnO₄ in comparison with SSR-Li₃MnO₄.

The FD process strongly affected the crystallinity of Li_3MnO_4 . Much broader diffraction peaks were obtained for FDR- Li_3MnO_4 (Fig. 4.2) as result of a significant change in the crystallite size, from 101.3 nm for SSR- Li_3MnO_4 to 35.5 nm for FDR- Li_3MnO_4 .

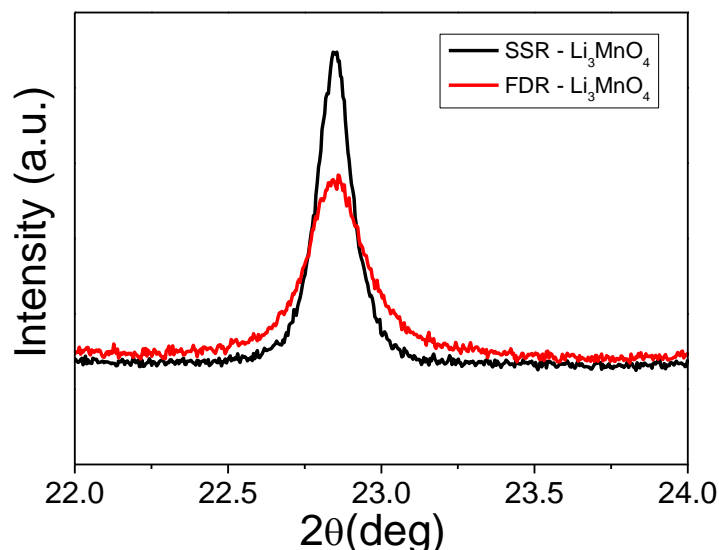


Figure 4.2: XRD patterns comparing the (101) reflection of SSR- Li_3MnO_4 (black) and FDR- Li_3MnO_4 (red).

This effect, as stated before, is a typical characteristic of materials prepared by freeze drying routes and it has been reported in lithium manganese spinel (LiMn_2O_4) synthesized by a FD method [100].

TEM micrographs (Fig. 4.3) show faceted particles with crystalline domains in the order of 60-100 nm for SSR- Li_3MnO_4 . Much smaller domains having a dimension close to 20-30 nm were detected for FDR- Li_3MnO_4 and those values are in good agreement with the estimated crystallite size by Scherrer analysis. The Fast Fourier Transform (FFT) in the lower right corner shows single crystallinity for the zone observed in Fig. 4.1(a), while a polycrystalline pattern on top of a strongly amorphous background is found in Fig. 4.1(b), for SSR- Li_3MnO_4 and FDR- Li_3MnO_4 respectively. Selected area electron diffraction (SAD) was carried out to study the local crystallinity of the compound. The upper right corner inset in Fig.4.3(a) shows very intense diffraction spots up to high order reflections resulting from a small number of highly crystalline grain orientations present in SSR- Li_3MnO_4 compound. The ED-pattern of the FDR- Li_3MnO_4 shows less intense reflections originating in several grain orientations on an amorphous background indicating a lower crystallinity (upper right corner inset in Fig.4.3(b)). These TEM results confirm the decrease in crystallinity and crystallite size for FDR- Li_3MnO_4 .

Lowering the crystallite size leads to shortening of the lithium ion diffusion path [101] which improves electrochemical performance as already observed for other Mn-based materials [102].

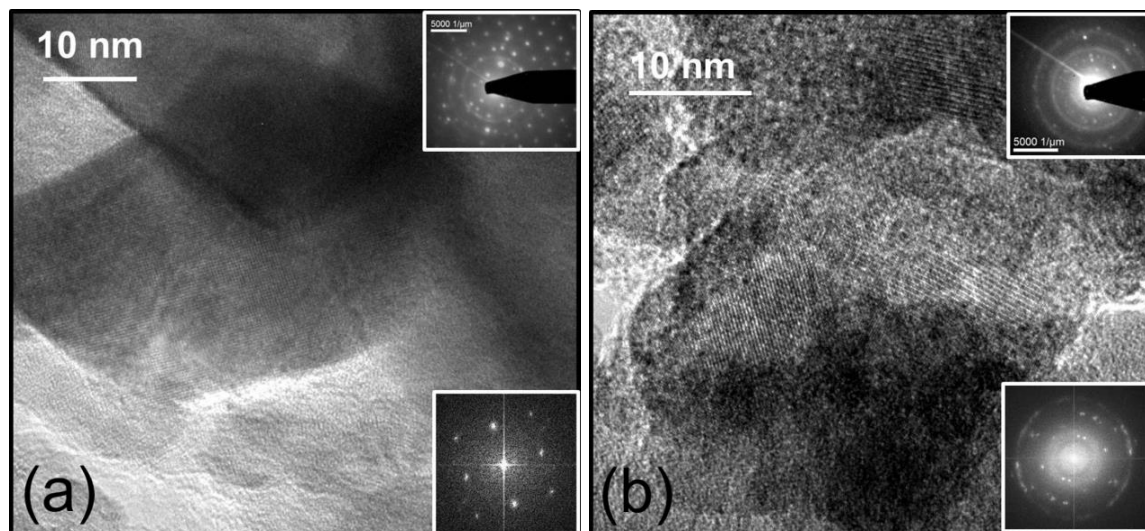


Figure 4.3: TEM micrographs of (a) SSR- Li_3MnO_4 and (b) FDR- Li_3MnO_4 . The inset in the upper right corners show selected area electron-diffractograms from a circular area with 260 nm in diameter, while the inset on the lower right corner show the FFT of the high resolution images.

SEM micrographs (Fig. 4.4) show a pronounced difference in morphology between the two compounds. SSR- Li_3MnO_4 is composed of micron-sized particles having an irregular shape.

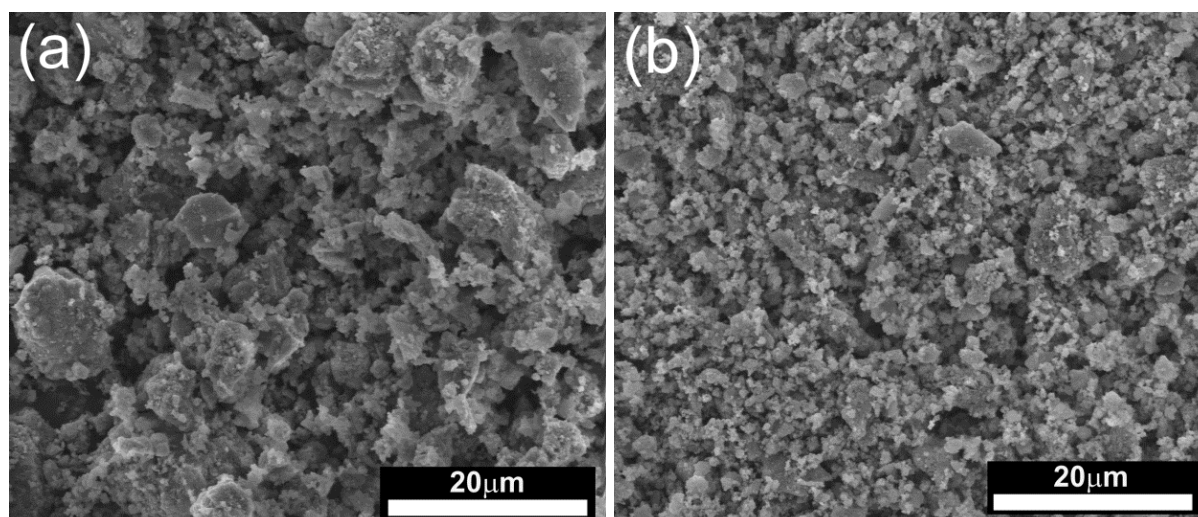


Figure 4.4: SEM micrographs of (a) SSR- Li_3MnO_4 and (b) FDR- Li_3MnO_4 .

To determine the particle size distribution, DLS measurements (Fig.4.5) were carried out. A mean particle size of 10 μm was obtained for the SSR material. Results for FDR- Li_3MnO_4

showed a lower degree of agglomeration and smaller particles, which have been quantified by DLS to have a mean size of 3.5 μm (Fig. 4.4).

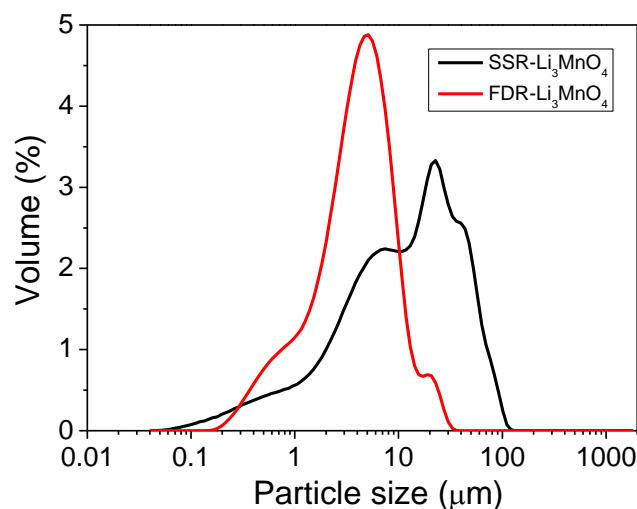
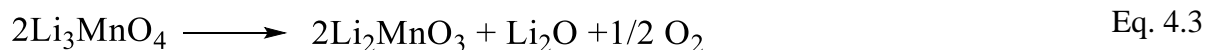


Figure 4.5: Particle size distribution of SSR- Li_3MnO_4 (black) and FDR- Li_3MnO_4 (red) in toluene.

The smaller average particle size resulted in a higher surface area for the FDR- Li_3MnO_4 (11.5 m^2/g) in comparison to SSR- Li_3MnO_4 (7.5 m^2/g), measured by BET. These results show that the microstructure of Li_3MnO_4 was successfully modified by the FD process. Consequently, improved electrochemical properties are expected for compounds with higher surface area. Thermal analysis conducted under inert conditions on SSR- Li_3MnO_4 and FDR- Li_3MnO_4 revealed that they start to decompose at around 120°C (Fig.4.6). The decomposition reaction proceeded slowly through the whole temperature range with a final temperature of 392-395°C. XRD patterns of the residuals after thermal analysis (not shown) confirmed the complete decomposition of the compounds. The weight loss for SSR- Li_3MnO_4 (5.6 wt.%) was in good agreement with the theoretical estimation (5.7 wt.%) relative to the expected decomposition reaction [103]:



The change in crystallite and particle size affected the thermal stability of the product depending on the synthesis method. In fact, FDR- Li_3MnO_4 showed a faster decomposition in comparison to SSR- Li_3MnO_4 and a slightly increase in weight loss (5.9 wt.%).

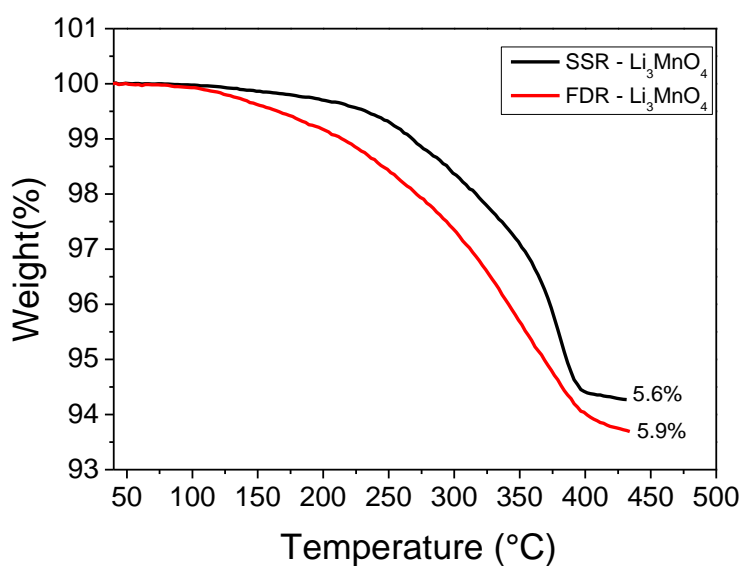


Figure 4.6: Relative weight loss of the SSR-Li₃MnO₄ (black) and FDR- Li₃MnO₄ (red) under N₂.

SSR- and FDR-Li₃MnO₄ were characterized by XPS to access the Mn oxidation state. The Mn2p spectra for SSR- and FDR-Li₃MnO₄ are shown in Fig.4.7. Both spectra exhibited two main peaks at 642.8 eV and 654.2 eV attributed to Mn2p_{3/2} and Mn2p_{1/2} respectively separated by a spin orbit splitting of 11.4 eV. The binding energies of the main manganese peaks are in good agreement with the Mn(V) oxidation state as already reported [103]. The spin splitting supports our assignment, since its value resides between the spin orbit values for Mn(IV) and Mn(VI)/Mn(VII) [104, 105].

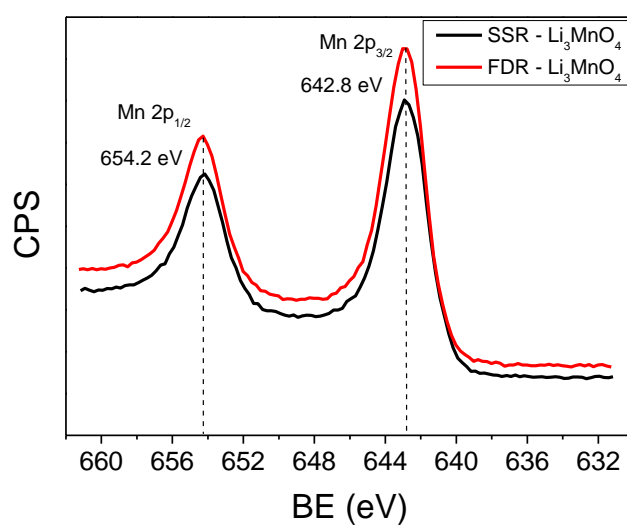


Figure 4.7: XPS spectra of SSR-Li₃MnO₄ (black) and FDR- Li₃MnO₄ (red).

In-situ high temperature XRD was carried out to better understand the formation mechanism of the final Li_3MnO_4 product by the SS and the FD route.

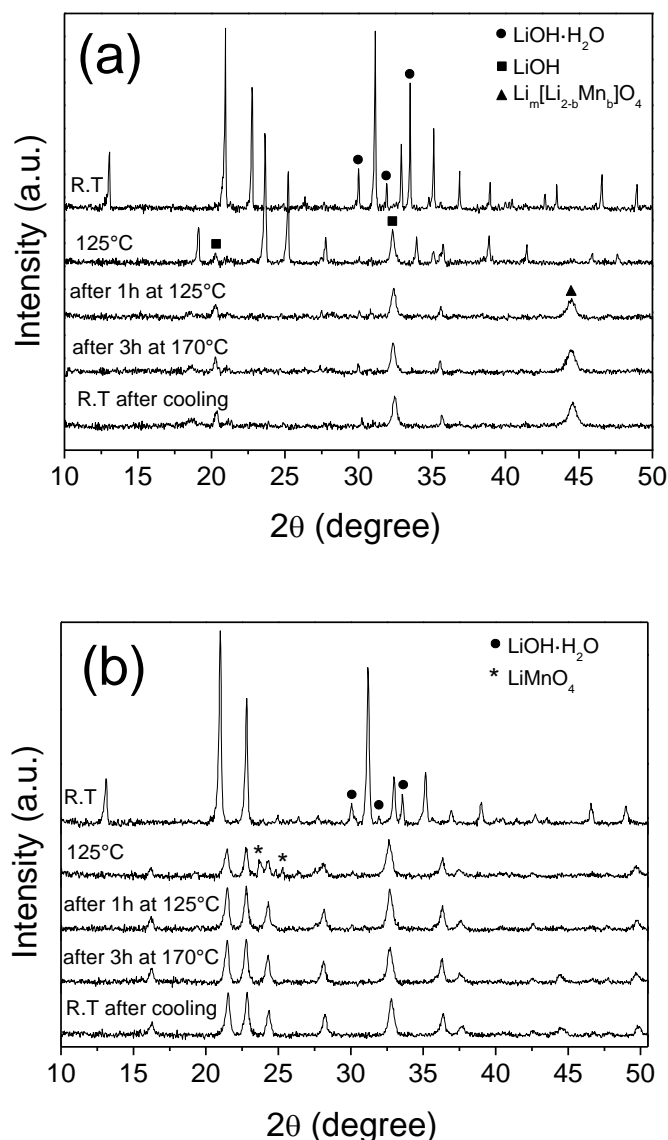


Figure 4.8: In-situ XRD patterns of $\text{LiMnO}_4 \cdot 3\text{H}_2\text{O} - 2\text{LiOH} \cdot \text{H}_2\text{O}$ for (a) SS and (b) FD precursor powders from room temperature (RT) to 170°C .

The measurements were performed on the ground precursor mixture used for the solid state route and on the precursor powder obtained after freeze drying employing the same heating procedure for both syntheses. The XRD patterns for the SSR material are shown in Fig. 4.8(a). At room temperature (RT) the pattern exhibit the peaks related to the two precursors ($\text{LiMnO}_4 \cdot 3\text{H}_2\text{O}$ and $\text{LiOH} \cdot \text{H}_2\text{O}$). At 125°C the dehydration of the precursors was complete and the pattern showed peaks assigned to anhydrous precursors (LiMnO_4 and LiOH). The decomposition of LiMnO_4 occurred after 1 h holding time at 125°C . The decomposition product

was a overstoichiometric Li-Mn spinel with a broad peak at 44.8° , already detected by RT XRD (Fig.4.1(a)). No changes in the XRD patterns were observed during the heating steps from 125°C to 170°C and after cooling to RT. The final pattern, obtained after cooling down to RT from 170°C did not show the formation of the Li_3MnO_4 phase. The two main phases present in these patterns were: Li-Mn spinel and LiOH.

Fig.4.8(b) shows the XRD patterns recorded for the freeze dried precursor powder at different temperatures. At RT, $\text{LiMnO}_4 \cdot 3\text{H}_2\text{O}$ and $\text{LiOH} \cdot \text{H}_2\text{O}$ were identified as the two main phases, which was in agreement with those observed for the SS route. After heating to 125°C , the formation of Li_3MnO_4 was detected. At this temperature the dehydrated precursor LiMnO_4 was still present (peak at 23.6°) but Li_3MnO_4 was already formed as the main phase. After 1h holding time at 125°C , only Li_3MnO_4 was present and this phase was stable during the heating to 170°C and further cooling down to RT.

The in-situ XRD measurements provide important insights about the formation mechanism of Li_3MnO_4 . The reaction is based on the diffusion process of Li^+ ions in the MnO_4^- permanganate framework with a simultaneous reduction of the Mn from (VII) to (V). The tetrahedral coordination of the Mn-ion remains unchanged during the reaction. Instead, the lithium coordination changes from octahedral to tetrahedral. In the light of these results the importance of the lithium diffusion process for the formation of this material is revealed. In the case of the SSR, the final compound could not be obtained starting with the ground powder because the reagents are mixed at a macroscopic level and this synthesis procedure requires additional grinding steps to enable the lithium diffusion into the LiMnO_4 .

Using the FD method the reagents are homogeneously mixed at a smaller scale allowing the formation of the final product Li_3MnO_4 without grinding steps at a lower reaction temperature.

The characterization carried out on SSR- Li_3MnO_4 , FDR- Li_3MnO_4 and related precursors showed: 1) the improvement of the synthesis procedure for the freeze drying route and 2) the influence of the FD process on the micro- and nanostructure of FDR- Li_3MnO_4 . SEM, BET and DLS characterization showed a decrease of the particle size from $10 \mu\text{m}$ to $3.5 \mu\text{m}$ and increased surface area. The crystallinity is also affected by the FD process; smaller crystallite size and lower crystallinity were confirmed by XRD and TEM.

Galvanostatic measurements were carried out to study the lithiation activity and stability of Li_3MnO_4 , and the effect of the synthesis route on its electrochemical properties. Four data sets were collected for both compounds obtained under defined electrochemical conditions: the cells were charged initially or discharged initially to evaluate the behaviour of the SSR- and

FDR compounds upon cycling when lithium is first removed (oxidation) or inserted (reduction) from/into the structure. These experiments serve to establish the reversibility of the lithiation/delithiation processes. In addition, measurements at two different current rates (10 A/kg and 50 A/kg) were performed to investigate the electrochemical kinetic behaviour of Li_3MnO_4 .

In Fig. 4.9 the 1st galvanostatic cycles of both SSR- and FDR- Li_3MnO_4 at 10 A/kg discharging initially (solid lines) and at 50 A/kg (dotted lines) are shown.

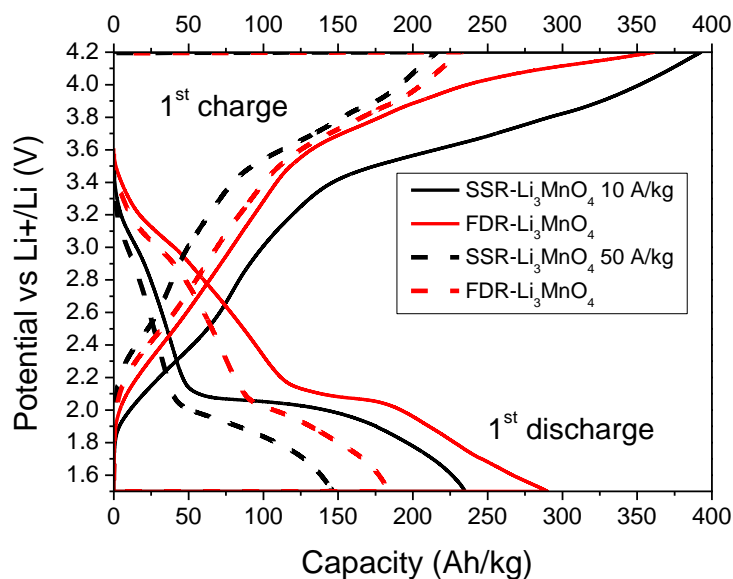


Figure 4.9: Discharge and charge profile for the 1st cycle between 4.2 V and 1.5 V at 10 A/kg (solid line) and 50 A/kg (dotted line) of SSR- Li_3MnO_4 (black) and FDR- Li_3MnO_4 (red). The cells were discharged initially.

The material has an open-circuit voltage (OCV) of 3.55 V in both cases. SSR- Li_3MnO_4 and FDR- Li_3MnO_4 showed comparable voltage profiles. During the first discharge, lithium intercalation occurred between the OCV and 2.1 V, and then a plateau appeared between 2.1 V and 2.0 V. This plateau can be assigned to the lithiation of Li_3MnO_4 as shown by the reaction described in Eq. 2. The final discharge capacities were 290 Ah/kg and 235 Ah/kg for the FDR- Li_3MnO_4 and SSR- Li_3MnO_4 , respectively. An increase in the discharge capacity of 23% (55 Ah kg^{-1}) was obtained for the FD compound. During the following charge, the plateau at 2.0 V disappeared and the compound showed an amorphous-like polarization curve with no clearly defined intercalation voltage plateau. Lithium intercalation is reversible after the 1st discharge, but the voltage profile significantly changes due to a change in the material structure. The 1st galvanostatic cycle at 50A/kg discharging initially (dotted line) showed the same voltage shape of the measurement at a lower rate (10 A kg^{-1}) during charge and discharge, but

an overall decrease in capacity can be seen. This indicates that the lithiation reaction is kinetically limited.

In Fig.4.10 the 1st galvanostatic cycles of both SSR-Li₃MnO₄ and FDR-Li₃MnO₄ are shown at 10 A/kg (solid line) and 50Ah kg⁻¹ (dotted line), when the cells were charged initially.

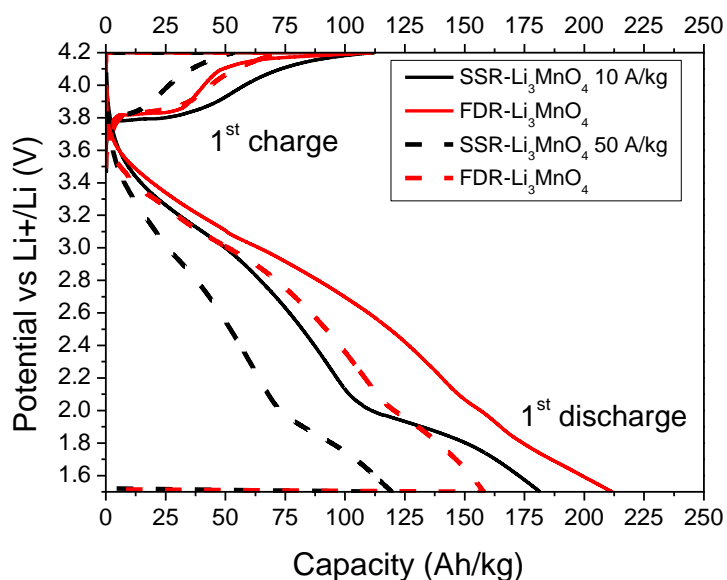


Figure 4.10: Charge and discharge profile for the 1st cycle between 4.2 V and 1.5 V at 10A/kg (solid line) and 50 A/kg (dotted line) of SSR-Li₃MnO₄ (black) and FDR-Li₃MnO₄ (red). The cells were charged initially.

The voltage profile during the first charge showed a plateau at 3.8 V, 0.4 V higher than the theoretically expected voltage due to the extraction of Li from Li₃MnO₄ (Eq. 1). The plateau was not reversible during the subsequent discharge. The plateau at 2.0 V was less pronounced comparing to the materials that were discharged first (Fig. 4.9). This result is an indication of an irreversible oxidation reaction occurring when the materials are first cycled at high potential and the lithium is removed from the structure. Lower discharge capacities were obtained when the cells were charged initially, but still a capacity improvement was observed for the FD compound (Table 4.2).

Table 4.2: Electrochemical data for all compounds.

Compound	Discharge capacity [Ah/kg]			
	Charged initially		Discharged initially	
	10 A/kg	50 A/kg	10 A/kg	50 A/kg
	1 st discharge	1 st discharge	1 st discharge	1 st discharge
SSR-Li ₃ MnO ₄	181	120	235	147
FDR-Li ₃ MnO ₄	212	158	290	184
Capacity improvement (%)	18	31	23	25

During the 2nd cycle, regardless whether the cells were discharged or charged initially, the voltage profile did not show any of the plateaux that were visible during the first cycle. Lithium insertion and extraction was reversible and occurred throughout the whole examined voltage range. However, the electrochemical features related to an ordered (crystal) structure with well- defined intercalation sites were lost as can be seen in Fig. 4.11 by the absence of any potential plateaux.

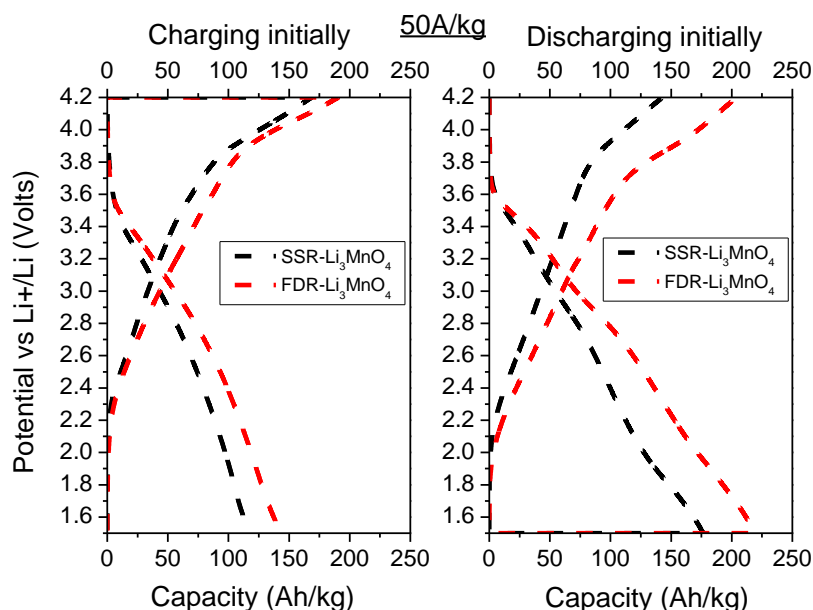


Figure 4.11: Voltage profile for the 2nd cycle between 4.2 V and 1.5 V at 50A/kg of SSR-Li₃MnO₄ (black) and FDR-Li₃MnO₄ (red).

A plot of discharge capacity vs cycle number is shown in Fig. 4.12(a) for measurements at 10A/kg and in Fig. 4.12(b) for measurements at 50 A/kg. It can be clearly seen, that the material prepared by FDR has a higher capacity on the first cycle compared to the one from the SSR independently of the electrochemical protocol. In all four examined protocols, a probable

reorganization of the material structure occurred within the first cycles, giving rise to a quick decrease in capacity. Then a slower degradation was observed until the 30th cycle. Very high capacities were recorded at 10 A/kg which implied large amounts of lithium being involved in the lithiation processes. We propose that structural stress or a kinetically limited conversion reaction could lead to the poor cyclability of these materials. SSR-Li₃MnO₄ and FDR-Li₃MnO₄ delivered around 60 Ah/kg at 10 A/kg after 30 cycles.

A better cyclability could be achieved at higher current rates (50 A/kg) resulting in a final higher absolute capacity. The compounds delivered around 80 Ah/kg after 30 cycles when the cells were initially charged. If the cells were initially discharged, however, SSR-Li₃MnO₄ showed a discharge capacity of 73 Ah/kg and FDR-Li₃MnO₄ 96 Ah/kg.

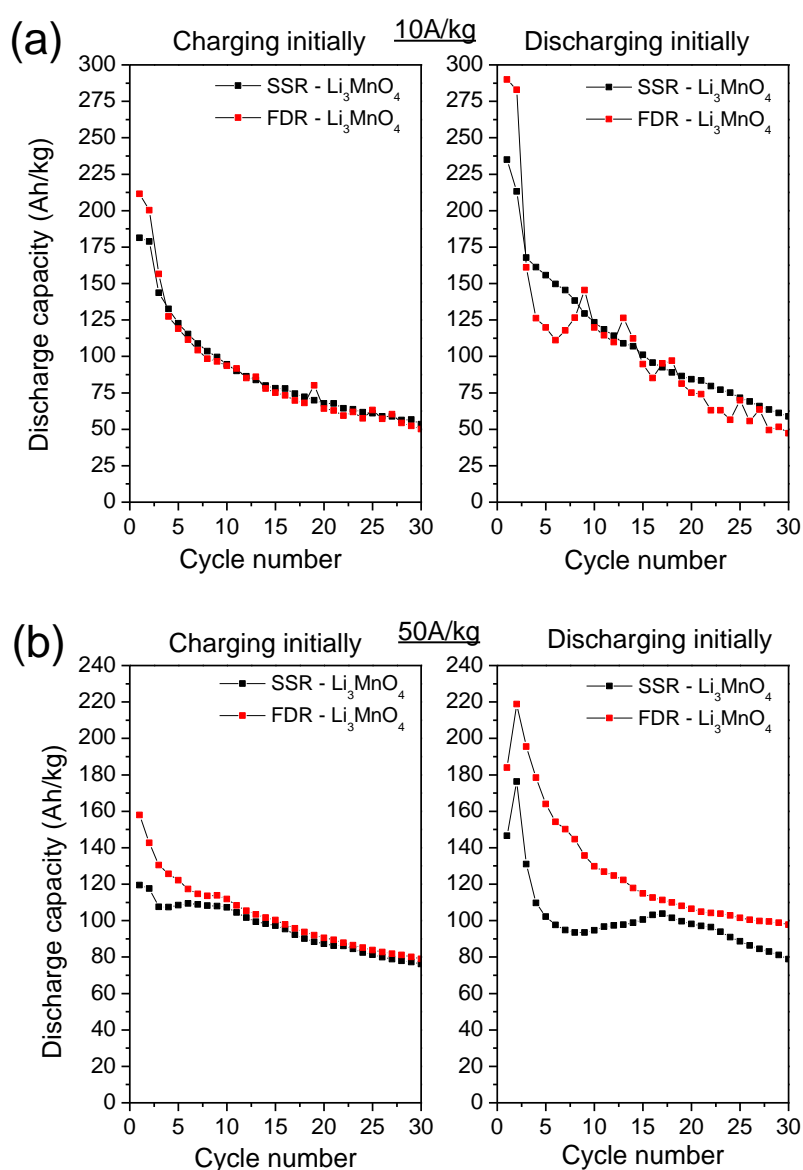


Figure 4.12: Discharge capacity vs cycle at (a) 10A/kg and (b) 50 A/kg of SSR-Li₃MnO₄ (black) and FDR-Li₃MnO₄ (red).

As for the electrochemical characterization, two main improvements can be observed for the FDR material comparing to the SSR: higher absolute initial capacity and faster kinetics. A larger amount of lithium can be inserted in FDR- Li_3MnO_4 ; between 18% and 31% higher capacity was obtained for all measurements in comparison to SSR- Li_3MnO_4 . The lithium intercalation is also faster in the FD material since higher capacity is obtained at higher current rates.

The stability over cycling of the two materials is very similar. The initial improvement, observed during the first 3-5 cycles for the FD compound, vanished during the following cycles. This can be attributed to a structural instability of Li_3MnO_4 . In fact, XRD after cycling showed an amorphous phase with no evidence of the initial crystal structure (Fig.4.13).

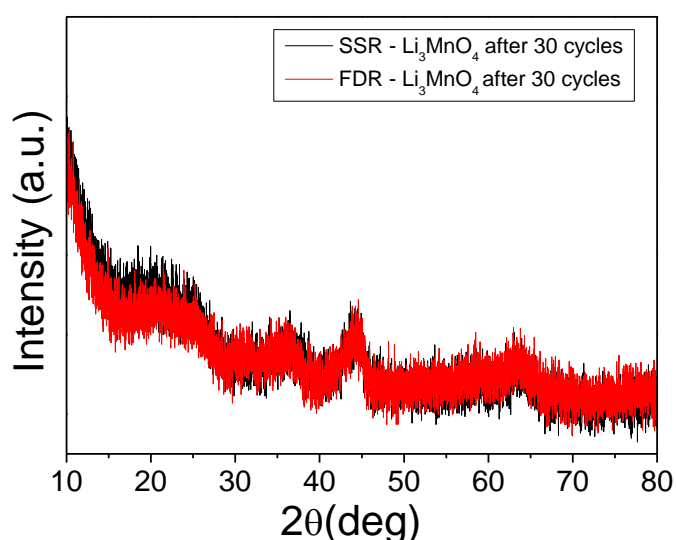


Figure 4.13: XRD patterns of SSR- Li_3MnO_4 (black) and FDR- Li_3MnO_4 (red) after 30 cycles.

The material structure can be correlated with the electrochemical properties as follows: lowering the particles size and increasing the surface area created more electroactive area for the lithium insertion. In the case of the FD compound, we propose that a higher number of lithiated particles in connection with a deeper lithiation are the most probable causes for the higher capacity. The smaller crystallite size, in addition, helps for better lithium diffusion: the lithium path into the material is shorter. Lithiation and delithiation processes can proceed faster than in the SS material. Nevertheless, the structural stability under cycling needs to be improved to obtain better capacity retention.

4.3 Capacity fading in Li_3MnO_4

In this subchapter we focused our attention on a step-wise *post-mortem* analysis of cycled Li_3MnO_4 . Through a detailed follow-up of the structural and chemical changes occurring during the lithiation and delithiation process in first full cycle (charge and discharge, discharge and charge) we aimed to understand the degradation mechanism.

Li_3MnO_4 shows a very fast capacity fading during cycling as shown in Fig.4.14a. The material capacity over 30 cycles drops by 66% and 75% when it is charged initially or discharged initially, respectively. The voltage profile of the 1st, 2nd, and 30th cycle is shown when the material is charged initially (Fig.4.14b) or discharged initially (Fig.4.14c).

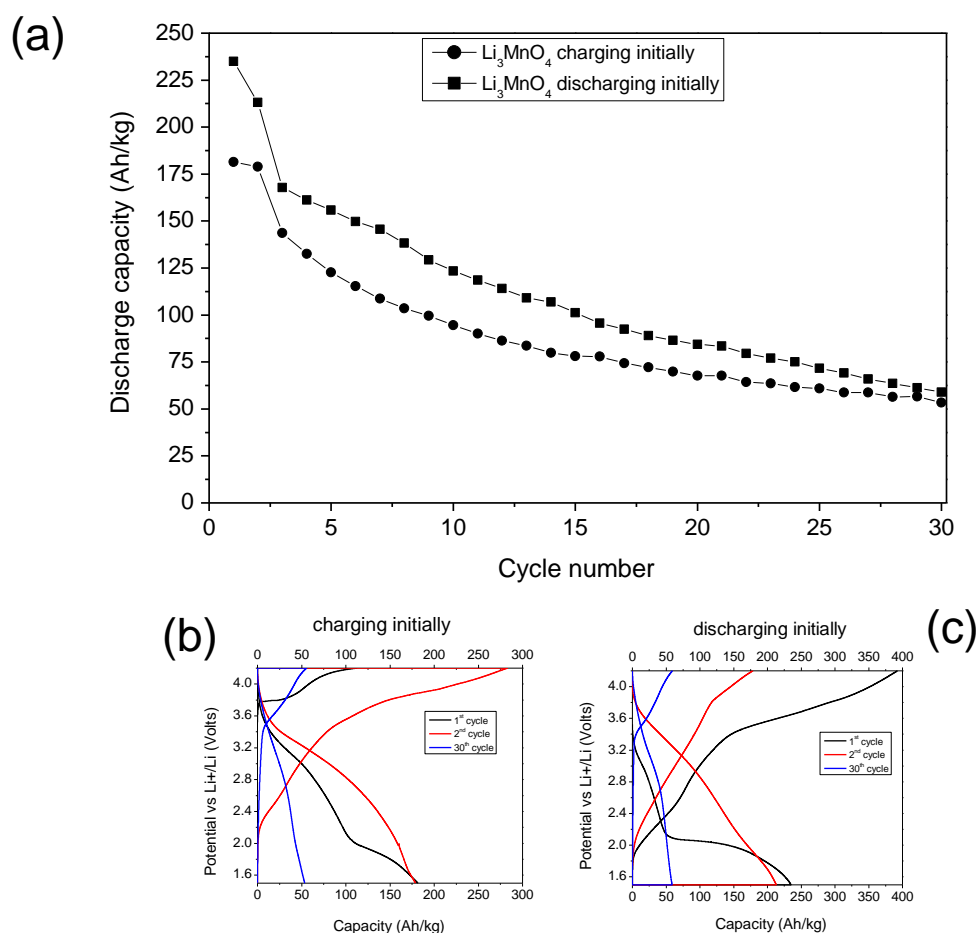
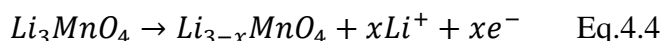


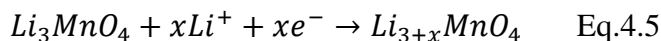
Figure 4.14: (a) Discharge capacity vs cycle at 10A/kg of Li_3MnO_4 , (b) voltage profile for the 1st, 2nd, 30th cycle between 4.2 V and 1.5 V at 10A/kg for Li_3MnO_4 charging initially, (c) voltage profile for the 1st, 2nd, 30th cycle between 4.2 V and 1.5 V at 10A/kg for Li_3MnO_4 discharging initially.

During the first charge (Fig.4.15a) a small plateau around 3.8 V was observed due to reaction described by Eq. 4.4, as suggested by Saint et al. [67]:



No plateau was present in the subsequent discharge. Therefore, we conclude that the reaction was irreversible.

When the material was initially discharged (Fig.4.15b), a plateau between 2.1 and 2.0 V was present due to reaction described by Eq.4.5 [67]:



Similar to reaction in Eq.4.4, the following charge showed an amorphous-like voltage shape with no evidence of the previously observed plateau, leading again to the conclusion that also this reaction (Eq.4.5) is irreversible. The voltage profile for the 2nd and 30th cycle clearly showed that the complete loss of structure is not regained in the following cycles and the amorphous voltage shape formed in the first cycle is kept. These are clear indications that the lithiation and delithiation processes associated with the above reactions led to irreversible structural changes and occurred already during the first cycle.

To better understand the material modifications during the first cycle, the analysis of Li_3MnO_4 was carried out by XRD, XPS, SEM/EDX and Raman spectroscopy at different states of charge after specific cycling protocols)

Four critical points in the voltage profile were identified which could provide us important information about the degradation mechanism in Li_3MnO_4 (Fig.4.15):

- Point 1: the material was initially charged to 4.2 V.
- Point 2: the material was initially charged to 4.2 V then discharged to 1.5 V.
- Point 3: the material was initially discharged to 1.5 V.
- Point 4: the material was initially discharged to 1.5 V and then charged to 4.2 V.

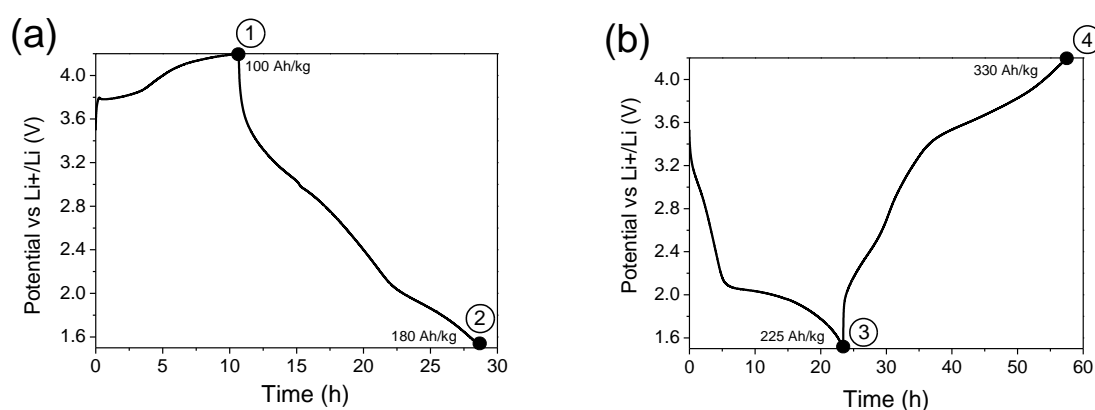


Figure 4.15: Voltage profile of Li_3MnO_4 for the 1st cycle between 1.5 V and 4.2 V at 50Ah/kg. The cells were a) charged initially and b) discharged initially.

In Fig.4.16 the XRD patterns of the fresh electrode and cycled electrodes are shown. Li_3MnO_4 -fresh showed a crystalline orthorhombic structure with the three main peaks be-

tween 20° and 25° 2θ degree. When the material was charged to 4.2 V (Li_3MnO_4 -1) a decrease of crystallinity and peak intensity was observed. The peak intensity further decreased during the following discharge to 1.5 V (Li_3MnO_4 -2) leaving an almost amorphous material after the 1st cycle. In the same way, the first lithiation of Li_3MnO_4 to 1.5 V (Li_3MnO_4 -3) destroyed completely the structure which was not restored in the following charge to 4.2 V (Li_3MnO_4 -4).

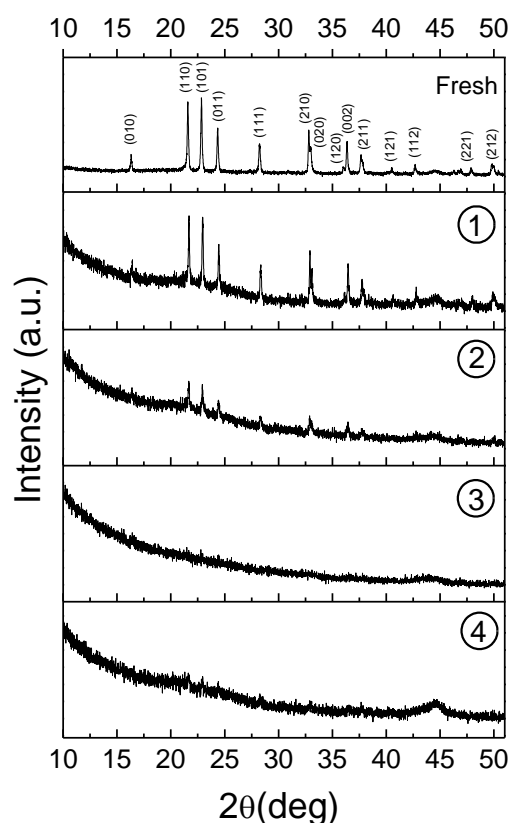


Figure 4.16: XRD patterns of the fresh electrode, Li_3MnO_4 -1, Li_3MnO_4 -2, Li_3MnO_4 -3, and Li_3MnO_4 -4.

The morphology of the electrodes was studied by scanning electron microscopy (SEM) (Fig.4.17). Since the electrode particles are embedded in carbon based conductive layer, backscattered electron micrographs were acquired to have higher bulk sensitivity and to obtain a better view of the particle dimensions and distribution after cycling. All samples were composed of micron-sized particles having an irregular shape with dimension around 10-15 μm . These particles were embedded in a carbon matrix. The amount of carbon used to prepare the samples (30 wt%) gave rise to an homogeneous dispersion of the Li_3MnO_4 in the carbon matrix (Fig. 4.17a). In all four cases, although we have seen before that cycling leads to amorphization, the particle size morphology did not change significantly. This is an indication that the amorphization did not trigger massive Mn dissolution during the first cycle.

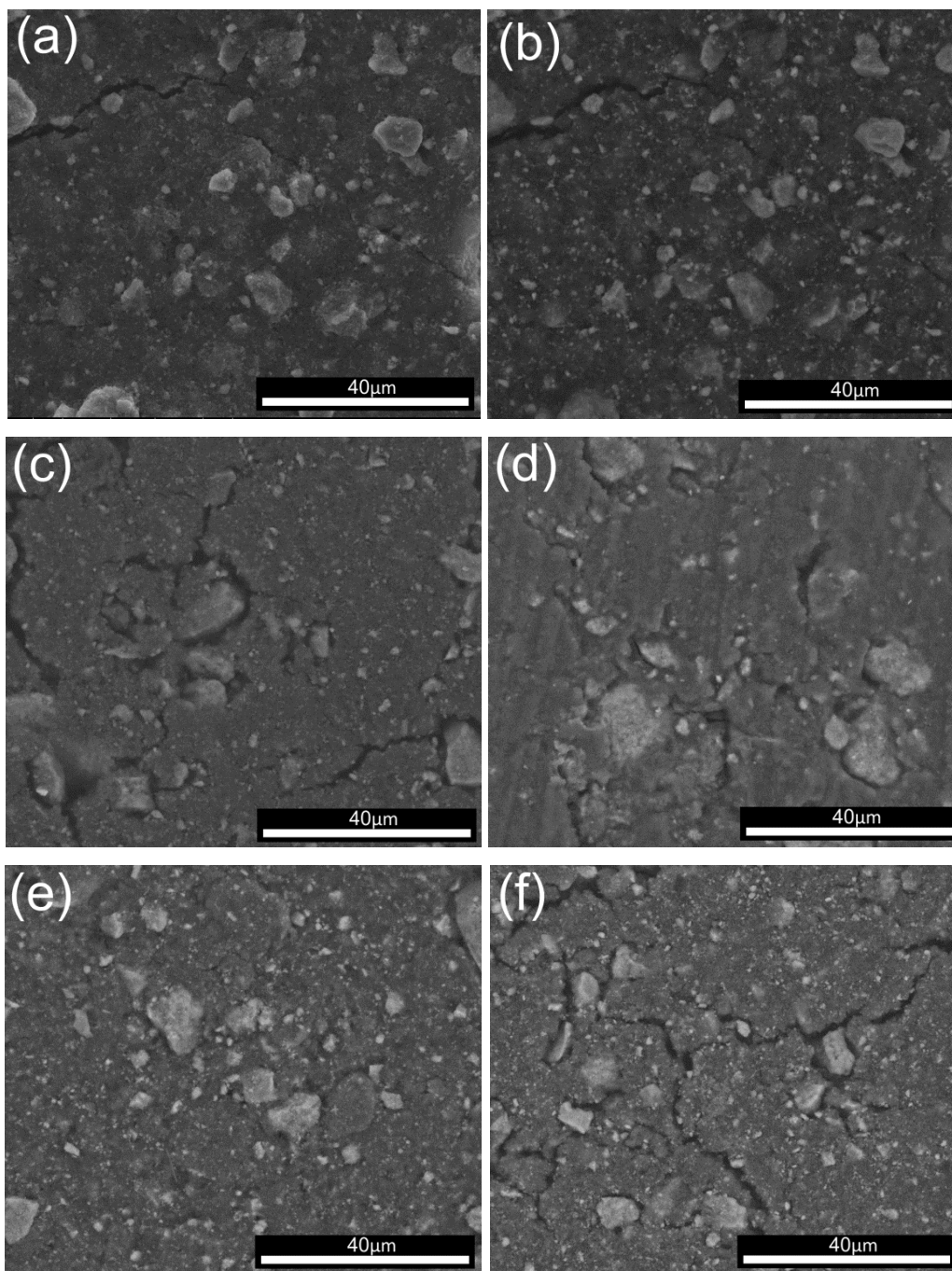


Figure 4.17: SEM micrographs of a) and b) the fresh electrode, c) Li_3MnO_4 -1, d) Li_3MnO_4 -2, e) Li_3MnO_4 -3, and f) Li_3MnO_4 -4.

X-ray photoelectron spectroscopy was carried out to determine how lithiation and delithiation of Li_3MnO_4 affect the oxidation state of manganese. In addition, the acquisition of oxygen, carbon and lithium spectra allowed to determine chemical changes involving directly the material but also the possible formation of new chemical species (Fig.4.18). The O1s spectrum of the fresh electrode showed one main peak at 531.0 eV with a shoulder at 528.9 eV. The former can be assigned to LiOH and the latter to a manganese-oxygen bond. The cycled electrodes showed similar features in the XPS spectra depending if they were in the charged state

($\text{Li}_3\text{MnO}_4\text{-1}$ and $\text{Li}_3\text{MnO}_4\text{-4}$) or in the discharged state ($\text{Li}_3\text{MnO}_4\text{-2}$, $\text{Li}_3\text{MnO}_4\text{-3}$). $\text{Li}_3\text{MnO}_4\text{-1}$ showed a broad peak shifted at higher BE (531.4 eV) due to LiOH with an additional contribution from Li_2CO_3 . $\text{Li}_3\text{MnO}_4\text{-2}$ and $\text{Li}_3\text{MnO}_4\text{-3}$ showed spectra with two contributions at lower BE in comparison to the charged state. The contribution at 530.7 eV can be assigned to Li_2O_2 and another one at 527.3 eV due to Li_2O [106]. The electrode $\text{Li}_3\text{MnO}_4\text{-4}$ in the charged state had a main peak due to Li_2CO_3 at 531.8 eV [107]. The formation of lithium oxide and carbonate species are commonly found on the surface of cycled electrode due to decomposition of the electrolyte [108].

The carbon 1s spectra did not provide important information because the amount of carbon used in the electrode preparation was much higher than the amount of C species which could be expected due to electrolyte degradation. The C1s spectra showed only the asymmetric peak typical of carbon black compounds. The main contribution came from the C-C bond centred at 284.3 eV and the asymmetry is due to C-O bonds lying around 286.0 eV [109].

The XPS spectra of the manganese showed the Mn 2p_{3/2} and 2p_{1/2} peaks. They were located at 642.3 eV in the fresh electrode and at 642.1 eV for $\text{Li}_3\text{MnO}_4\text{-1}$ and $\text{Li}_3\text{MnO}_4\text{-4}$ indicating that the active species is Mn^{4+} . However, the intensity of the Mn signal in the discharged state decreased considerably and for $\text{Li}_3\text{MnO}_4\text{-3}$ the Mn signal was almost not detectable. This was already observed for Mn-based cathode materials and it was interpreted as solid electrolyte interface (SEI) formation on the surface of the particles [110]. During the following charge, SEI dissolution or creation of cracks in the SEI layer allowed the detection of the Mn signal.

The Li1s and Mn3p zone was analysed to confirm our previous findings. The XPS spectra of the fresh electrode showed a Li1s peak at 54.8 eV typical of LiOH species and a Mn3p peak at 49.5 eV due to Mn^{4+} . The electrodes recovered after an electrochemical charge against lithium ($\text{Li}_3\text{MnO}_4\text{-1}$ and $\text{Li}_3\text{MnO}_4\text{-4}$) showed a peak shift towards higher BE of Li1s peak (55.4 eV and 55.6 eV, respectively) in agreement with O1s shift, due to the formation of Li_2CO_3 . However, since the Li1s peak of LiOH and Li_2O_2 overlap [107], the electrodes in the discharged state ($\text{Li}_3\text{MnO}_4\text{-2}$ and $\text{Li}_3\text{MnO}_4\text{-3}$) showed a Li1s main peak at the same binding energy of the fresh electrode (54.8 eV) which can be assigned to Li_2O_2 with an additional shoulder related to the formation of Li_2O . The Mn3p peaks were also in agreement with the measurements of the Mn2p energy level. $\text{Li}_3\text{MnO}_4\text{-1}$ and $\text{Li}_3\text{MnO}_4\text{-4}$ showed a shift towards lower BE (48.9 eV and 49.1 eV, respectively) probably because the 3p orbitals were more affected than the 2p but their values were still in the range of the Mn^{4+} oxidation state. In $\text{Li}_3\text{MnO}_4\text{-2}$ and $\text{Li}_3\text{MnO}_4\text{-3}$ the manganese was hardly detectable due probably to SEI formation as discussed above.

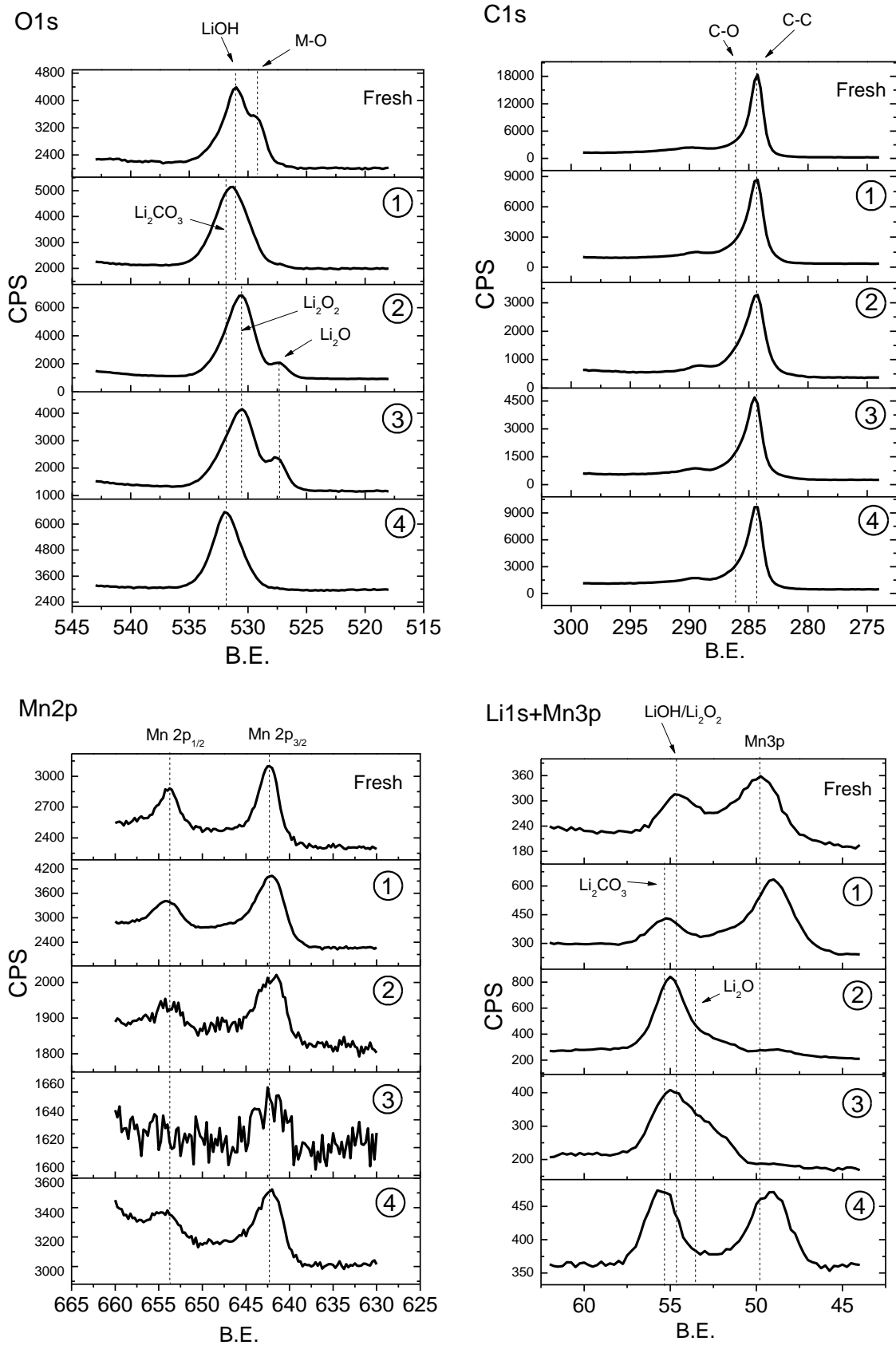


Figure 4.18: XPS spectra for a) O1s, b) C1s, c) Mn2p and d) Li1s+Mn3p of the fresh electrode, Li₃MnO₄-1, Li₃MnO₄-2, Li₃MnO₄-3, and Li₃MnO₄-4.

Raman spectroscopy was carried out on all electrodes to study the Mn chemical environment and to get better insight about the bonding in the amorphous material (Fig.4.19). The deeper penetration depth of Raman spectroscopy in comparison with XPS allowed obtaining information about Li_3MnO_4 vibrations in the fresh electrode. A sharp peak was observed at 756 cm^{-1} related to Mn-O stretching (A_1 mode) of the $[\text{MnO}_4]^{3-}$ tetrahedron [111, 112]. The carbon matrix gave rise to signals characteristic of the D and G bands located around $1350\text{--}1360\text{ cm}^{-1}$ and $1580\text{--}1590\text{ cm}^{-1}$, respectively [113]. $\text{Li}_3\text{MnO}_4\text{-1}$ and $\text{Li}_3\text{MnO}_4\text{-4}$ showed a broad peak centred at 620 cm^{-1} , typical of Mn-O stretching in O_h [91] coordination indicating that the coordination surrounding the Mn ion changed during the cycling. In $\text{Li}_3\text{MnO}_4\text{-2}$ and $\text{Li}_3\text{MnO}_4\text{-3}$ spectra the Mn signal was not detectable; this is in agreement with XPS analysis and confirmed the presence of a thick SEI formed during discharge. Considering the Raman analysis there are strong indications that the amorphous compound, formed from decomposition of Li_3MnO_4 , is amorphous MnO_2 .

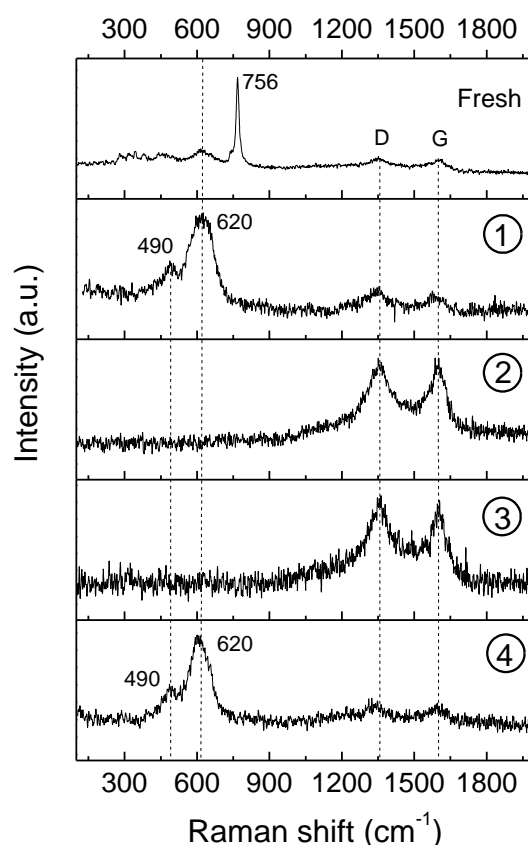


Figure 4.19: Raman spectra of the fresh electrode, $\text{Li}_3\text{MnO}_4\text{-1}$, $\text{Li}_3\text{MnO}_4\text{-2}$, $\text{Li}_3\text{MnO}_4\text{-3}$, and $\text{Li}_3\text{MnO}_4\text{-4}$.

The overall characterization carried out on fresh and cycled electrode allowed us to propose a mechanism for the electrochemical degradation of Li_3MnO_4 (Fig.4.20).

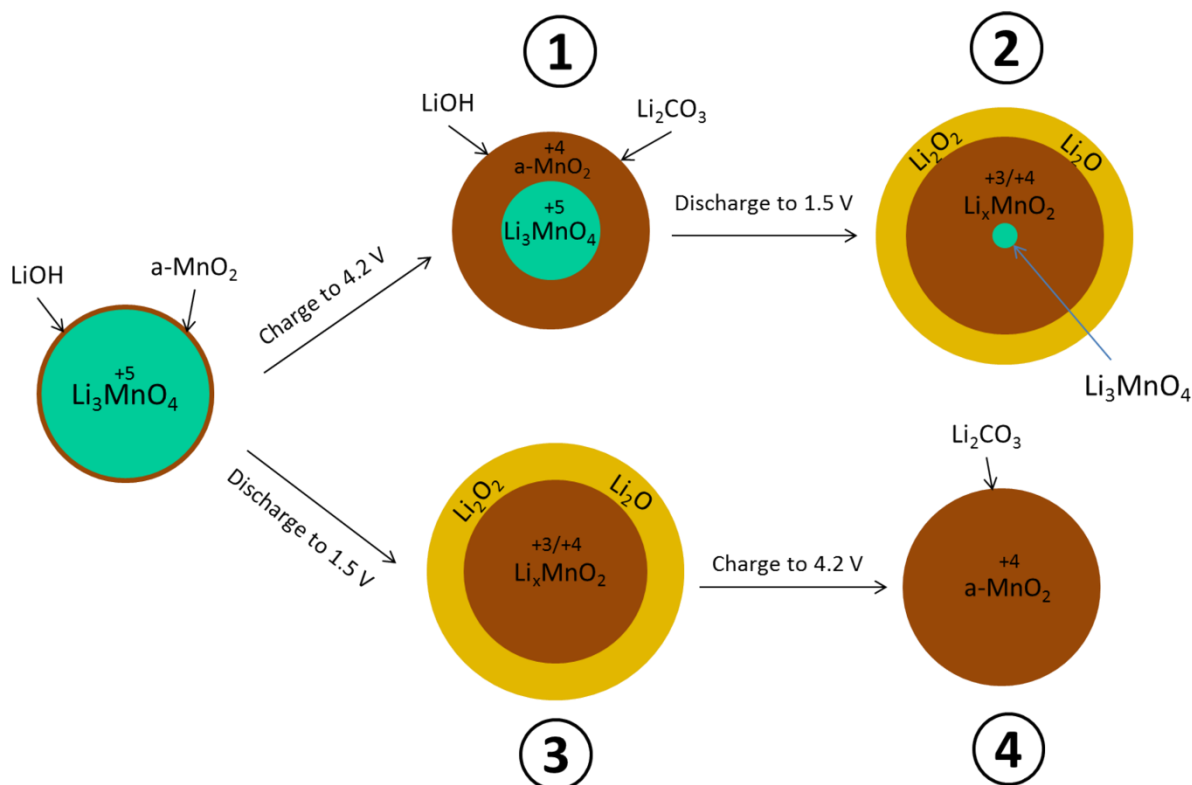


Figure 4.20: Degradation mechanism of Li_3MnO_4

Starting from the fresh electrode, XRD and Raman spectroscopy confirmed the Li_3MnO_4 phase. The presence of a very thin layer of LiOH and MnO_2 on the surface of the particles, detectable only by XPS, can be explained with the high reactivity of Mn^{5+} . In fact, as it was reported previously [103], the detection of Mn^{5+} by XPS should be possible in the bare powder. However, in this case, the electrode preparation in organic solvents and the absorption of water molecules from the atmosphere could have caused the reduction of Mn^{5+} to Mn^{4+} and the formation of LiOH on the surface.

When the material was initially charged (point 1), approximately 0.5 Li equivalents could be extracted from the structure (100Ah/kg) with the characteristic plateau at 3.8 V (Eq.1). The extraction of Li ions should theoretically lead to an oxidation of the Mn^{5+} ions; instead surprisingly Mn^{4+} was detected by XPS with a concomitant destruction of the crystal structure (lower intensity in XRD) and the detection of Li_2CO_3 . Our interpretation of these results is that the amorphization caused by Li removal gave rise to an extraction of oxygen species, as already known for Mn-based cathode materials [30, 114]. Simultaneously Mn ions were reduced from Mn^{5+} to Mn^{4+} and the electrolyte was oxidized to form Li_2CO_3 , as already ob-

served before [115]. The manganese has now oxidation state (IV); except a few very rare examples of materials with Mn^{4+} in tetrahedral coordination, the most stable coordination in this oxidation state is the octahedral one [68]. In fact, the coordination changed from T_d to the most stable O_h as verified by Raman spectroscopy. In the following discharge (point 2) around 1 Li equivalent was inserted in the structure (180 Ah/kg) causing the reduction of the remaining manganese Mn^{5+} to Mn^{4+} and Mn^{3+} (not visible in the XPS). This resulted in the almost complete collapse of the structure and probably further oxygen species were released. The oxygen species formed during these processes can directly react with lithium ions or can be electrochemically reduced to Li_2O_2 and Li_2O [39, 116] creating a thick inorganic SEI on the surface of the particles, as observed by XPS. This SEI hinders the detection of Mn by XPS and Raman spectroscopy in the discharged state.

When the material was discharged initially (point 3), Li ions were inserted into the structure for a total of 1.5 Li equivalents (230Ah/kg) at 1.5 V. The same behaviour was observed as described above: amorphization of the material and SEI formation. In the following charge (point 4) a much higher capacity was recorded (330Ah/kg) in comparison with the previous discharge. This was due to the electrochemical oxidation of Li_2O_2 and Li_2O composing the SEI which left back the “naked” particles of amorphous MnO_2 as confirmed by Raman and XPS spectroscopy.

Amorphization during the first cycle occurred without apparent change in the particle morphology as we discussed above. However, SEM/EDX analysis was also carried out on the separator and lithium anode after cycling, more precisely at point 3 and 4. In all analysed zones no Mn was detected leading to the conclusion that a massive dissolution is not the cause of amorphization.

Further characterization was carried out after 30 cycles to study possible modifications related to cycling. In Fig. 4.21a the XRD pattern of Li_3MnO_4 is shown after 30 cycles. As explained above, the compound formed by degradation of Li_3MnO_4 during the first cycle was amorphous MnO_2 and this is the compound which was cycled in the following cycles. As expected for amorphous manganese oxide, the cycling did not influence the short range order and the compound remained amorphous during cycling [117]. It is well known that Mn dissolution affects the performance of Mn-based battery materials [59], but in our case the particle morphology was not strongly affected as can be seen in Fig.4.21b, in the allocated amount of cycles.

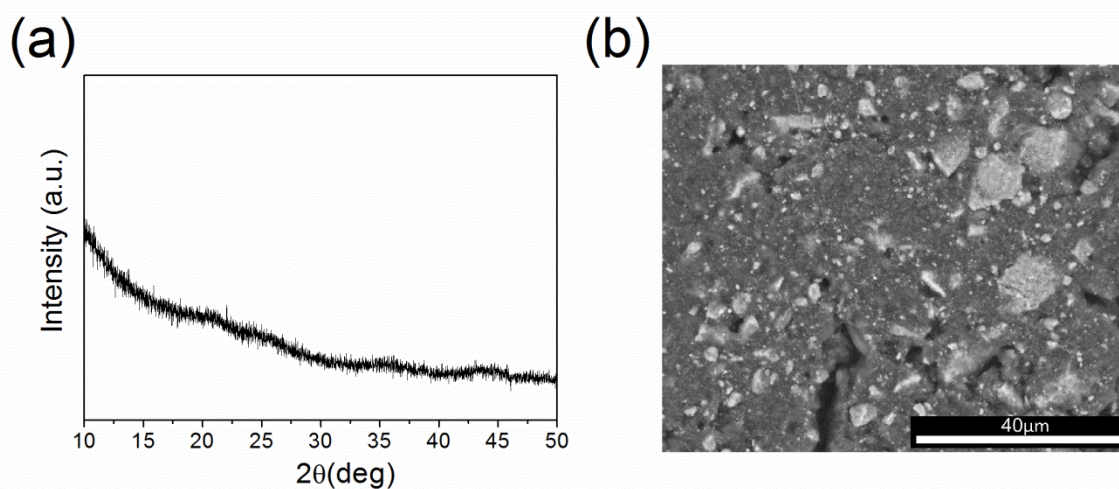


Figure 4.21: (a) XRD pattern of Li_3MnO_4 after 30 cycles (b) SEM micrographs of Li_3MnO_4 after 30 cycles.

From this detailed post mortem study we could confirm that the fast capacity fading recorded in the previous chapter was due to the electrochemical conversion of Li_3MnO_4 to amorphous MnO_2 by electrochemical degradation already during the first cycle. The low cycling stability is the well-known behaviour of amorphous manganese oxide [118] formed during the first cycle.

4.4 Vanadium incorporation in Li_3MnO_4

In the previous chapter, a *post-mortem* analysis of SSR- Li_3MnO_4 revealed the conversion of this material to $\alpha\text{-MnO}_2$ during cycling. For this reason, our work focused now on the attempt to improve the structural stability of Li_3MnO_4 to obtain better capacity retention.

Substitution of the electroactive metal ion in cathode materials is a well-known approach to obtain structural stabilization. For example, in layered LiNiO_2 substitution of Ni^{3+} by Co^{3+} increased the cation ordering allowing for a higher reversible capacity [20, 25]. In LiMn_2O_4 , substitution of Mn^{3+} by Ni^{3+} or Co^{3+} lowered the $\text{Mn}^{3+}/\text{Mn}^{4+}$ ratio, decreased Mn dissolution, suppressed the transition to tetragonal phase, and increased cycling stability [25].

Considering Li_3MnO_4 , Saint et al.[67] proposed to substitute Mn^{5+} with V^{5+} or P^{5+} ions, this could lead to the exchange of MnO_4^{n-} oxyanions with the much more stable VO_4^{n-} or PO_4^{n-} oxyanions, with the aim to increase the structural stability and lowering the capacity fading.

Taking into account the very low formation and decomposition temperature of Li_3MnO_4 , the incorporation of V^{5+} or P^{5+} ions by classic solid state reaction techniques is not a very promising approach due to the very low ion diffusion coefficient below 200°C (decomposition temperature of Li_3MnO_4). Therefore, it is preferable to mix the metal ions by solution techniques. This can be easily performed using the FD process proposed in the previous subchapter for the synthesis of pristine Li_3MnO_4 . The FD process has the potential to incorporate metal ions by facilitating the phase mixing procedure and hence contribute to the stabilization of the cycling behaviour. Vanadium ions were chosen for the incorporation because vanadium can theoretically fulfil a double function: 1) it can act as stabilizer for the structure as described above, and it can act as electroactive metal ion increasing capacity or voltage.

Considering that Li_3MnO_4 and Li_3VO_4 have the same crystal structure and that the ionic radii of $\text{Mn}^{5+}(\text{T}_d)$ and $\text{V}^{5+}(\text{T}_d)$ are very similar (0.330 \AA and 0.355 \AA , respectively) the creation of a solid solution $\text{Li}_3\text{Mn}_{1-x}\text{V}_x\text{O}_4$ is theoretically possible. For this reason our first attempt was to synthesize a solid solution with high vanadium content (50 at%).

The synthesis route described for the pristine material was now applied for the solid-solution synthesis between vanadium and manganese. Ammonium metavanadate (NH_4VO_3) was selected as vanadium source because vanadium is in (V) oxidation state and the compound is soluble in water.

The XRD pattern of the precursor powder after FD is shown in Figure 4.22. The main peaks were indexed as $\text{LiMnO}_4 \cdot 3\text{H}_2\text{O}$ phase. Peaks of KMnO_4 (dark square) were also present as impurity due to incomplete exchange of potassium ions with lithium ions. These peaks were superimposed to a weak hump present between 10° and 40° , indication of a secondary phase.

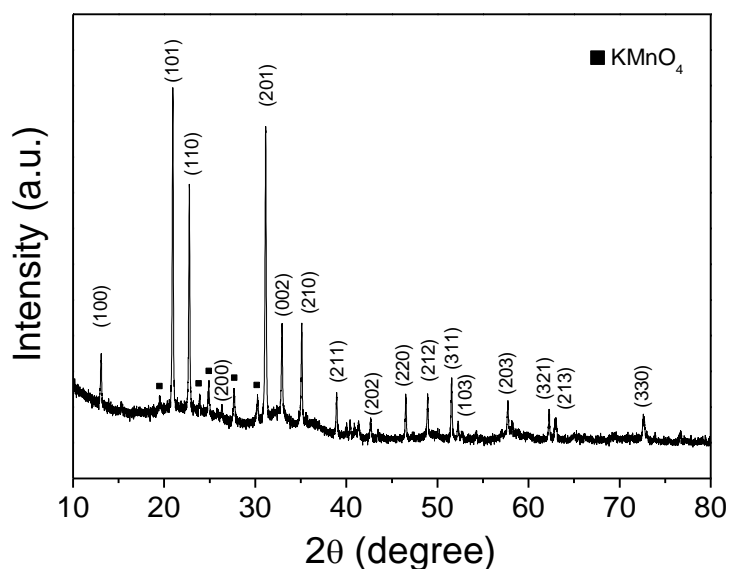


Figure 4.22: XDR pattern of the FD powder.

Li_3MnO_4 and Li_3VO_4 show almost identical XRD patterns, therefore the solid solution between MnO_4^{3-} and VO_4^{3-} should have similar peak positions as the parent compounds.

The XRD pattern of the final compound labelled as FDR- $\text{Li}_3\text{Mn}_{0.5}\text{V}_{0.5}\text{O}_4$ is shown in Fig.4.23.

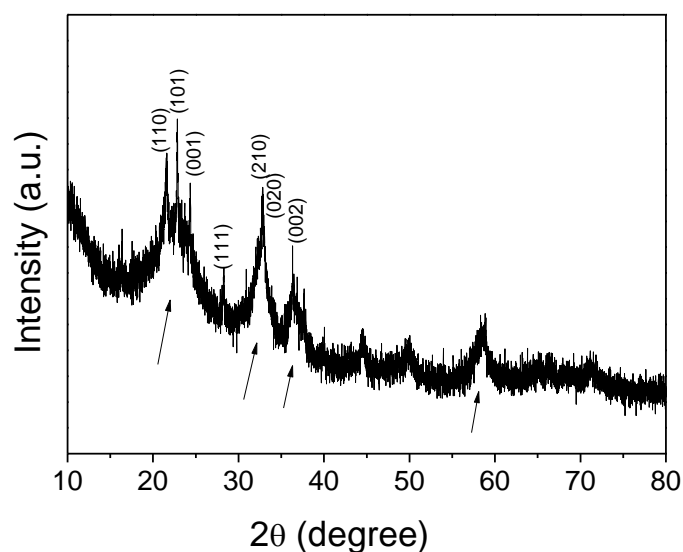


Figure 4.23: XDR pattern of the FDR- $\text{Li}_3\text{Mn}_{0.5}\text{V}_{0.5}\text{O}_4$ powder.

Two clear contributions were present in the pattern: sharp peaks having low intensity plus very broad peaks. The sharp peaks could be assigned to both phases (Li_3MnO_4 and/or Li_3VO_4) but the broad peaks (indicated with arrows), were an indication of a phase separation during the freeze drying process.

To understand if the formation of the solid solution was successful, and to clarify the nature of the broad peaks, pristine FDR- Li_3MnO_4 and FDR- Li_3VO_4 were synthesized by the FD process and subjected to the same temperature treatment of FDR- $\text{Li}_3\text{Mn}_{0.5}\text{V}_{0.5}\text{O}_4$. The XRD patterns obtained from these powders were successively compared (Fig.4.24). FDR- Li_3MnO_4 (Fig.4.24a) showed a crystalline structure with reflection assigned to orthorhombic crystal system (Chapter 4 subchapter 4.2). FDR- Li_3VO_4 instead showed very broad peaks indication for a nano-crystalline material with crystallite size lower than 10 nm [119, 120]; FDR- $\text{Li}_3\text{Mn}_{0.5}\text{V}_{0.5}\text{O}_4$ seemed to be constituted by the superimposition of these two different phases: the crystalline FDR- Li_3MnO_4 and the nano-crystalline FDR- Li_3VO_4 .

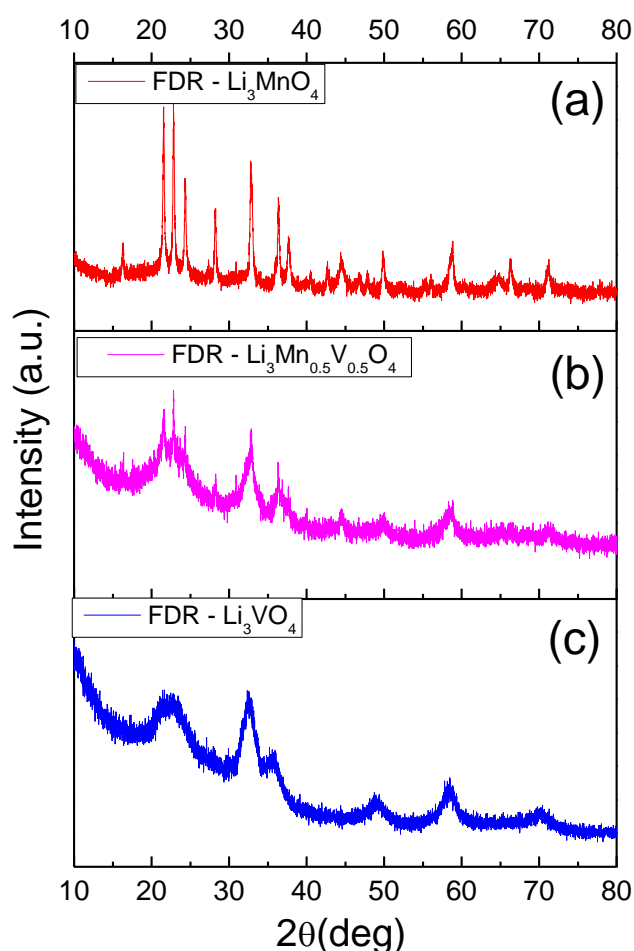
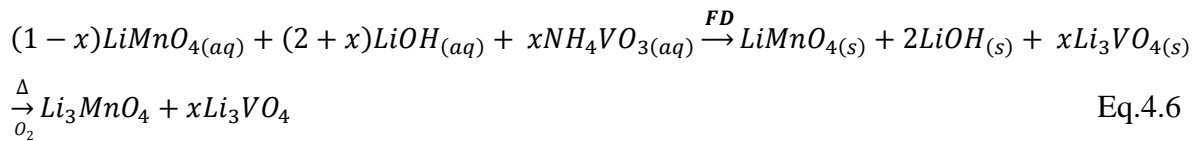


Figure 4.24: XDR pattern of (a) FDR- Li_3MnO_4 , (b) FDR- $\text{Li}_3\text{Mn}_{0.5}\text{V}_{0.5}\text{O}_4$ (c) FDR- Li_3VO_4 powder.

The interpretation of the XRD measurements (Fig.4.22, 4.23, 4.24) is that during the sublimation of the water in the FD process, a phase separation between LiMnO_4 and Li_3VO_4 occurred. Li_3VO_4 was made of very small crystallite size and originated the weak hump (Fig.4.22). During the subsequent heating step, the low synthesis temperature allowed only the transformation from LiMnO_4 to Li_3MnO_4 to take place, leaving unchanged the nano-crystalline Li_3VO_4 phase which is now more visible in XRD due to the lower intensity of the Li_3MnO_4 peaks. The entire process can be summarized by the Eq.4.4:



This explanation was confirmed by HT-XRD carried out on FDR- Li_3VO_4 (Fig.4.25). In fact, the crystallization of the vanadate phase out of the nanocrystalline precursor started around 400°C and was complete around 600°C . At this temperature, the manganate phase was already formed and underwent decomposition (TGA Chapter 4 subchapter 4.2)

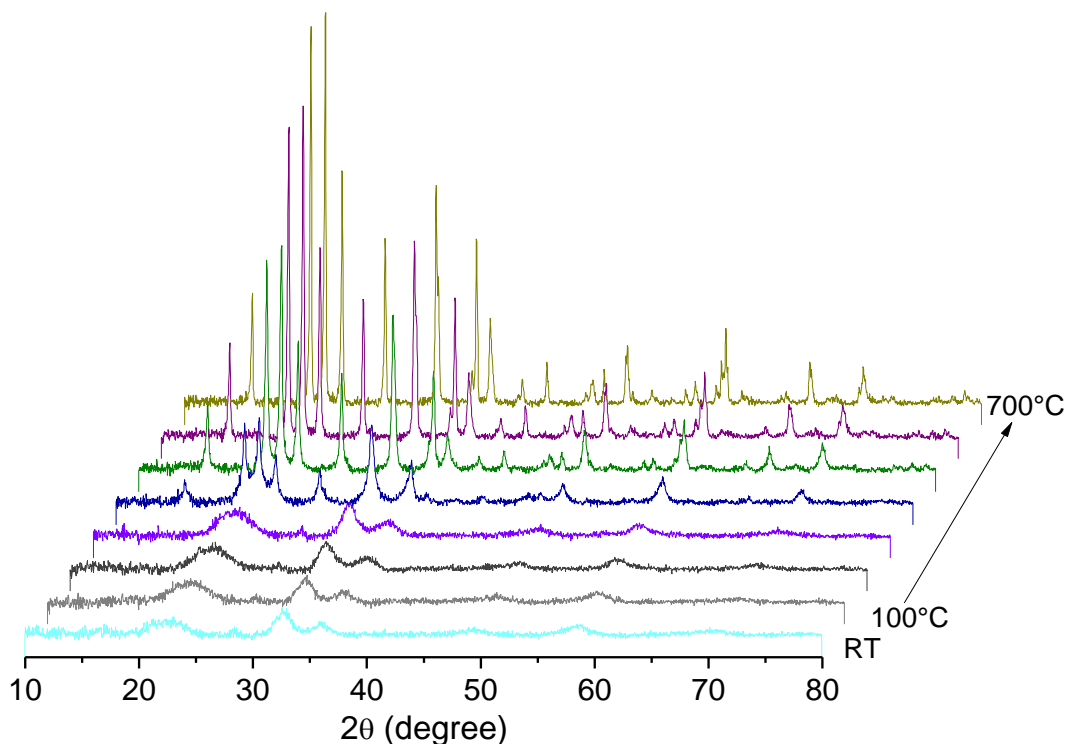


Figure 4.25: High Temperature HT-XDR pattern of FDR- Li_3VO_4 powder.

Morphology and chemical composition of the sample were studied by SEM/EDX. FDR- $\text{Li}_3\text{Mn}_{0.5}\text{V}_{0.5}\text{O}_4$ was composed of micron-sized particles and porous sheets, a probable result of the water sublimation during the FD process (Figure 4.26). The distribution of Mn and V was homogeneous in all analyzed zones with an average composition of 47.9 at% of vanadium and 52.1 at% of manganese which was in good agreement with the nominal composition.

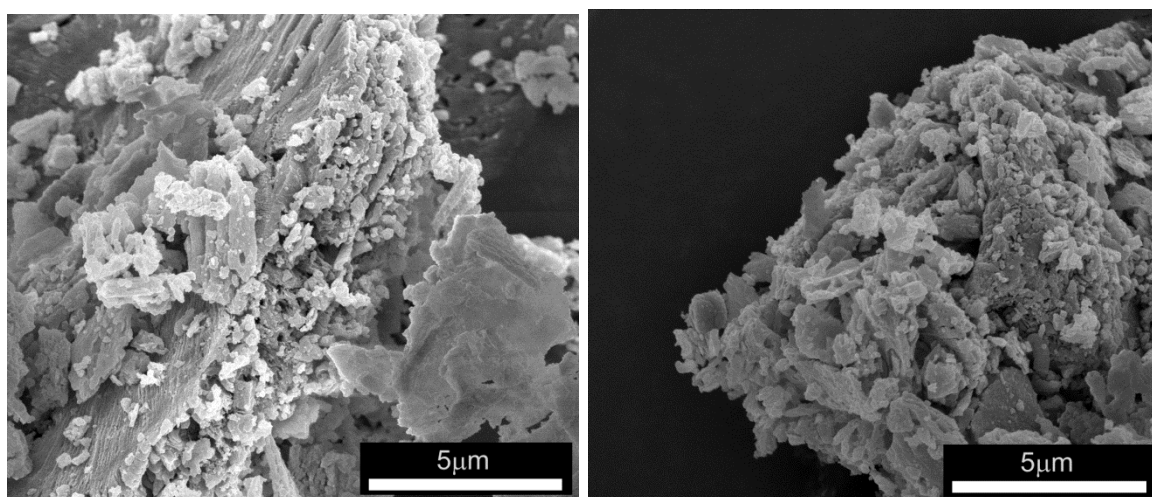
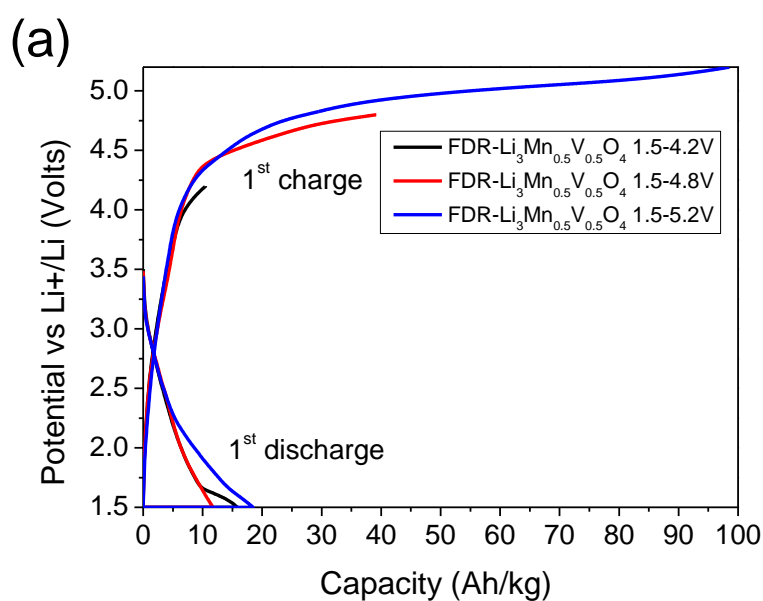


Figure 4.26: SEM micrographs of FDR- $\text{Li}_3\text{Mn}_{0.5}\text{V}_{0.5}\text{O}_4$

Galvanostatic measurements were carried out to study the electrochemical properties of FDR- $\text{Li}_3\text{Mn}_{0.5}\text{V}_{0.5}\text{O}_4$. In Fig.4.27a and Fig.4.27b the voltage profiles of the 1st and the 2nd cycle using different cut-off voltages during charge are shown.



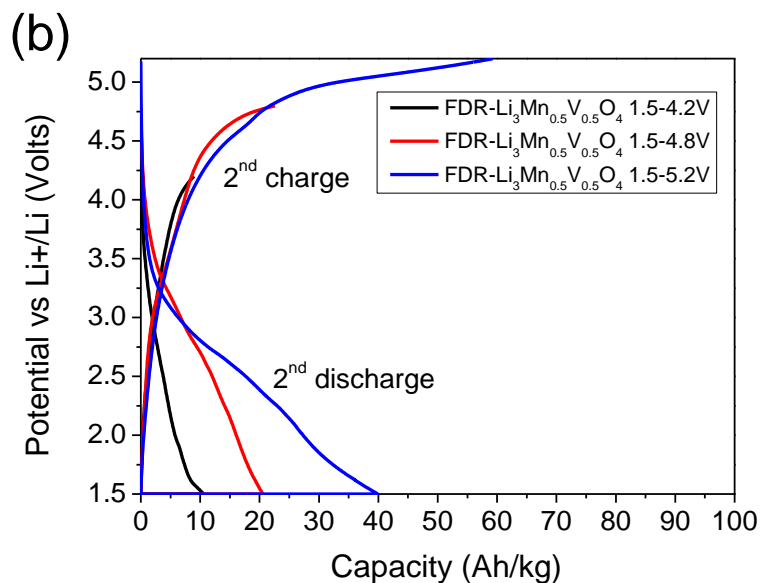


Figure 4.27: Discharge and charge profile for the (a) 1st cycle and (b) 2nd cycle between 1.5-4.2 V (black), 1.5-4.8 V (red), and 1.5-5.2 V (blue) at 50A/kg of FDR- $\text{Li}_3\text{Mn}_{0.5}\text{V}_{0.5}\text{O}_4$. The cells were discharged initially.

Taking into account the same voltage range used to analyze the pristine material (1.5-4.2 V, Fig.4.9 and Fig.4.10), a huge capacity decrease during charge and discharge was observed for the vanadium containing compound in comparison with the pristine FD compound. Extending the analyzed voltage range to higher potentials, an increase in charge capacity was observed above 4.5 V. Even though the material was cycled at high voltages during the 1st cycle, the discharge capacity during the 2nd cycle was still very low (< 40 Ah/Kg). For this reason, the additional capacity obtained above 4.5 V during the first charge can be associated to an irreversible removal of oxygen species.

Li_3MnO_4 is a cathode material active between 4.2 V and 1.5 V while Li_3VO_4 is known to be an anode material active between 1.5 V and 0.1 V (capacity of 350Ah/kg) [46]. Taking into account the very low capacity recorded at high voltages it is likely that in FDR- $\text{Li}_3\text{Mn}_{0.5}\text{V}_{0.5}\text{O}_4$ only the vanadate phase is the active phase.

To extract more information about the redox potential of this material and to confirm our previous hypothesis, FDR- $\text{Li}_3\text{Mn}_{0.5}\text{V}_{0.5}\text{O}_4$ was also tested at low voltages (Fig.4.28) and compared with pristine FDR- Li_3MnO_4 and FDR- Li_3VO_4 . The discharge profile of FDR- $\text{Li}_3\text{Mn}_{0.5}\text{V}_{0.5}\text{O}_4$ showed two main contributions to the total capacity: 1) a plateau between 1.2 V and 0.2 V contributing about 350 Ah/kg and 2) a plateau between 0.2 V and 0.1 V with a total capacity of about 1000 Ah/kg. Considering that the Mn redox reaction should occur between 3.0 V and 1.5 V and this feature was not present in the voltage profile of FDR- $\text{Li}_3\text{Mn}_{0.5}\text{V}_{0.5}\text{O}_4$, the first contribution can be assigned to the intercalation of Li-ions into the

Li_3VO_4 phase, and the second contribution was due to over-reduction of the manganese phase (probable formation of MnO) with irreversible conversion reactions and SEI formation [121].

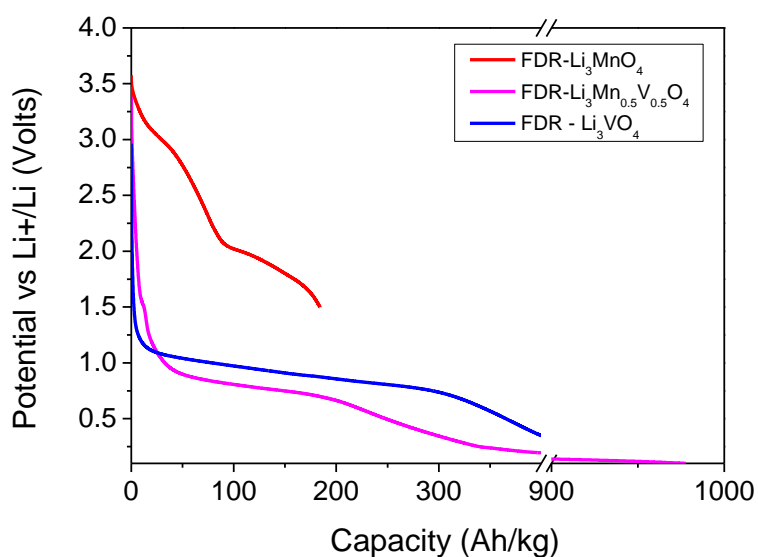


Figure 4.28: 1st discharge profile at 50A/kg of FDR- Li_3MnO_4 (red), FDR- $\text{Li}_3\text{Mn}_{0.5}\text{V}_{0.5}\text{O}_4$ (magenta), SSR- Li_3VO_4 (blue). Cells were discharged initially.

To further prove that the disappearance of the Mn redox activity at high voltages in FDR- $\text{Li}_3\text{Mn}_{0.5}\text{V}_{0.5}\text{O}_4$ was a direct consequence of the FD process, galvanostatic measurements were carried out on a 50/50 wt.% ground mixture between SSR- Li_3MnO_4 and SSR- Li_3VO_4 (Fig. 4.29). In this case, indeed, manganese activity occurred between 3.0 V and 1.5 V, as shown by the arrow.

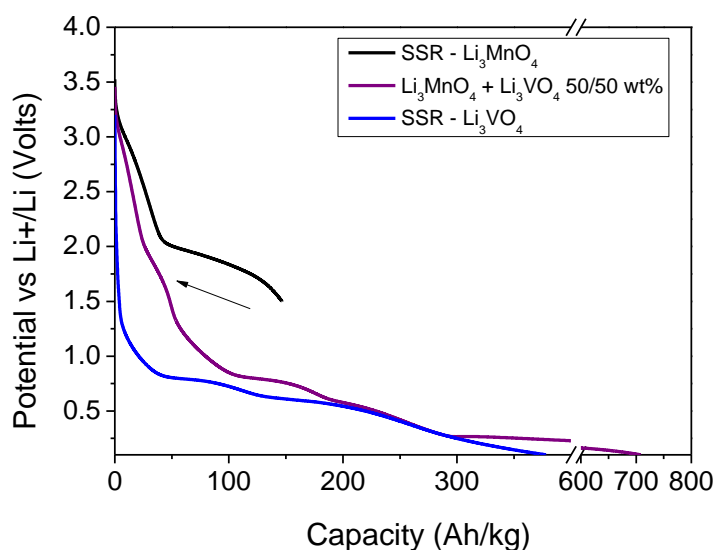


Figure 4.29: 1st discharge profile at 50A/kg of SSR- Li_3MnO_4 (black), SSR- Li_3MnO_4 +SSR- Li_3VO_4 50/50 wt.% (purple), SSR- Li_3VO_4 (blue). Cells were discharged initially.

The overall characterization carried out on FDR- $\text{Li}_3\text{Mn}_{0.5}\text{V}_{0.5}\text{O}_4$ showed that the attempt of creating a solid solution with a vanadium content of 50 at% by FD synthesis led to a bi-phase material composed of a crystalline Li_3MnO_4 phase and a nano-crystalline Li_3VO_4 phase; However, the disappearance of the Mn contribution at high voltages was a clear indication that a morphological shielding of the Mn phase was present (i.e. coverage of Li_3MnO_4 particles with Li_3VO_4).

Taking into account the results shown above, a smaller amount of vanadium (5 wt%) was then used for the solid solution reaction. The synthesis was carried out as previously explained (Eq.1 and Eq.2). In Fig.4.30 the XRD patterns of pristine FDR- Li_3MnO_4 and FDR- $\text{Li}_3\text{Mn}_{0.95}\text{V}_{0.05}\text{O}_4$ is shown. No differences were observed in the peak positions; however a weak hump was clearly visible between 20° and 25° . This originated probably from the nano-crystalline Li_3VO_4 phase formed during the FD process, as shown above for 50 at% V.

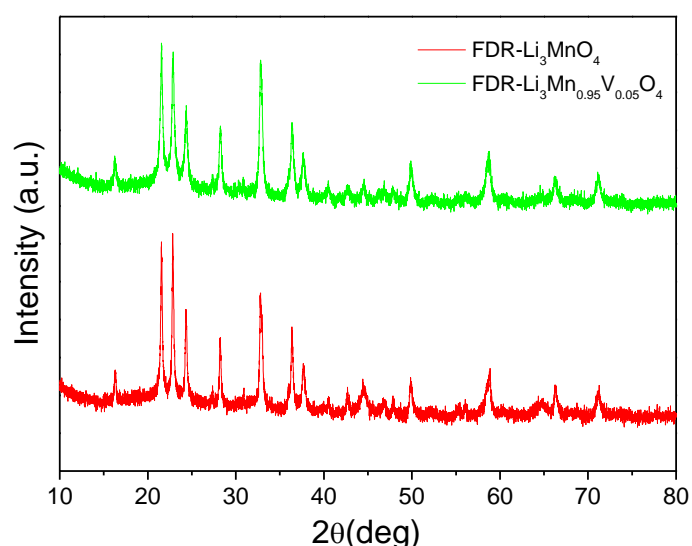


Figure 4.30: XDR pattern of FDR- Li_3MnO_4 (red) and FDR- $\text{Li}_3\text{Mn}_{0.95}\text{V}_{0.05}\text{O}_4$ (green) powder.

Le Bail fitting was carried out to study the influence of vanadium content on Li_3MnO_4 lattice parameters. A small contraction was observed along the a axis, compensated by an expansion along the b and c axes (Table 4.3). The vanadium, if incorporated in the structure, should lead to lattice expansion. Considering the increase in the background and the significant change in the b axis, the assumption was that the incorporation of vanadium in the Li_3MnO_4 structure occurred only partially (< 5 at.%).

Table 4.3: Le bail fitting results.

Samples	R_{wp} (%)	R_{exp} (%)	χ^2	a (Å)	b (Å)	c (Å)	Crystallite size (nm)
FDR- Li_3MnO_4	2.71	2.40	1.27	6.3074(2)	5.4212(2)	4.9306(2)	35.5(1)
FDR- $\text{Li}_3\text{Mn}_{0.95}\text{V}_{0.05}\text{O}_4$	2.25	1.73	1.69	6.3042(3)	5.4316(3)	4.9320(2)	20.7(1)

The main difference between the two compounds resided in the electrochemical properties.

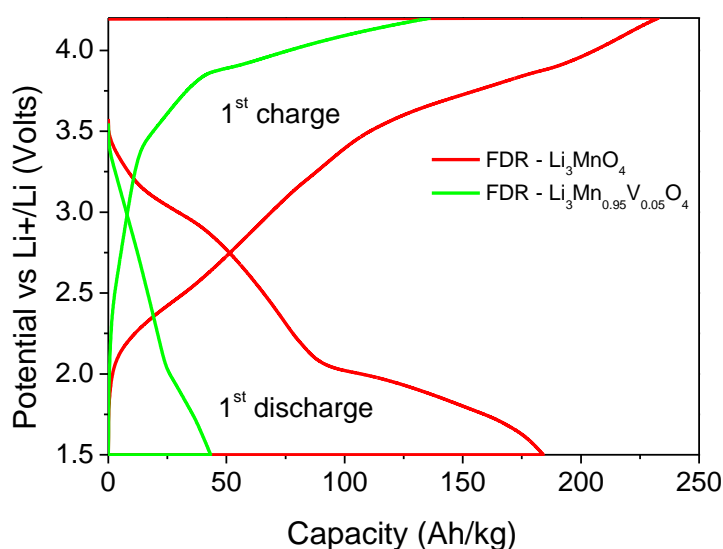


Figure 4.31: 1st cycle between 1.5-4.2 V at 50A/kg of FDR- Li_3MnO_4 (red), FDR- $\text{Li}_3\text{Mn}_{0.95}\text{V}_{0.05}\text{O}_4$ (green).

The vanadium containing compound showed a 1st discharge capacity of 45Ah/kg, in comparison with 185Ah/kg of the pristine Li_3MnO_4 (Fig.4.31). Even though the vanadium amount was very small, the influence on the discharge capacity was relevant.

In conclusion, in both attempts of vanadium doping (50 at% and 5 at%) the final result on the electrochemical properties was a significant capacity decrease. This was probable due to the formation of a nano-crystalline Li_3VO_4 phase which interacting with Li_3MnO_4 , shield the Mn activity at higher voltages.

Chapter 5

5. Manganese in square pyramidal coordination: h-LiMnBO₃

5.1 Introduction

Lithium metal oxides containing polyanion groups $(XO_m)^{n-}$, such as phosphate $(PO_4)^{3-}$ [122], silicate $(SiO_4)^{3-}$ [56], borates $(BO_3)^{3-}$ [123], are very attractive candidates as cathode materials for Li-ion batteries. Even though these units are not electro-active, they introduce several advantages especially as enhanced stability at higher cycling voltages [57] and voltage tuning due to the inductive effect of the polyanion group on the metal cation [124].

Among them, borates LiMBO₃ (M=Fe,Mn,Co) could be good alternatives to phosphates due to the lower weight of the $(BO_3)^{3-}$ group. In particular, LiMnBO₃ is a very promising cathode material because of its high theoretical capacity of 220 Ah/kg [69].

LiMnBO₃ has two polymorphs: hexagonal [125] and monoclinic [126] with theoretical cell voltage of 4.1 V and 3.7 V vs Li⁺/Li, respectively [69].

The hexagonal polymorph has a $[MnBO_3]_n^{n-}$ framework with MnO₅ square pyramids and BO₃ units. MnO₅ square pyramids shared two opposite edges of its square base with two adjacent pyramids forming chains along the [001] direction. The BO₃ groups link three chains via corner sharing. This framework creates channels along the [001] directions where Li atoms occupy tetrahedral sites. LiO₄ tetrahedra share two corners forming chains along [001] (Fig.5.1a) [125].

The monoclinic polymorph has a $[MnBO_3]_n^{n-}$ framework with MnO₅ trigonal bipyramids and BO₃ units. MnO₅ trigonal bipyramids shares two edges with adjacent bipyramids forming a single chain along the [-101] direction. The BO₃ groups link three chains via corner sharing. Li atoms reside in tetrahedral coordination [126] (Fig. 5.1b).

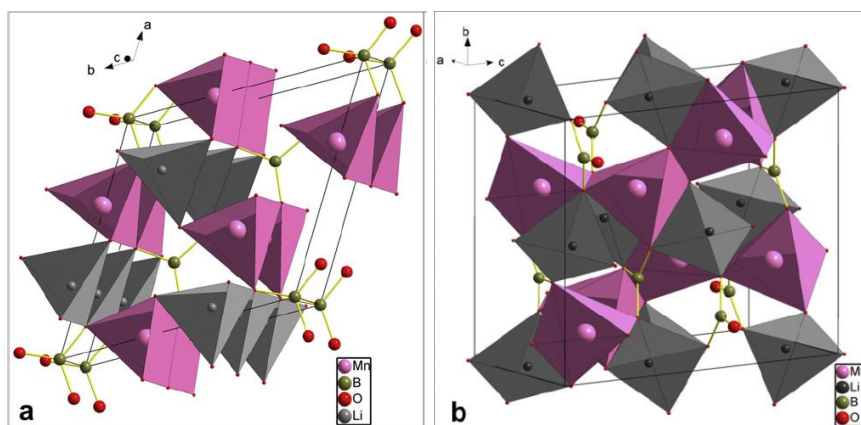


Figure 5.1: Crystal structure of (a) hexagonal and (b) monoclinic polymorph (adapted from [57]).

Similar to phosphates [127], lithium transition metal borates are considered to have intrinsically low ionic and electronic conductivity, which is believed to be the cause of the poor electrochemical performance. For this reason the synthesis of nanosized materials with carbon coating for increased electronic conductivity are compulsory to obtain decent capacities. Up to date, LiMnBO_3 is mainly fabricated through solid state reaction at 500°C to obtain the monoclinic phase and at $800\text{-}850^\circ\text{C}$ to obtain the hexagonal phase [69] under inert or reducing atmosphere. Two-step calcination processes were usually required together with intermediate ball-milling to reduce the particle size after the first calcination process. Recently LiMnBO_3 was also synthesized by sol-gel [57] and microwave synthesis [128]. The carbon-coated LiMnBO_3 was usually fabricated via the calcination of the mixture of LiMnBO_3 and carbon sources (i.e sucrose) under inert atmosphere to create a LiMnBO_3/C composite [129]. At present, crystalline monoclinic *m*- LiMnBO_3 was the most studied phase reaching a capacity of 150-160 Ah/kg for about 50 cycles. Crystalline hexagonal *h*- LiMnBO_3 instead showed very small capacity of about 50 Ah/kg (in both cases with carbon coating). *h*- LiMnBO_3 was synthesized as nano-crystalline material and it showed much higher capacity around 120 Ah/kg [57].

As shown in Chapter 4 for Li_3MnO_4 , FD synthesis was a technique which allowed obtaining nanocrystalline materials and lowering the reaction temperature due to better reagents mixing at nanoscopic level. In this chapter it will be described, how the use of this synthesis route enabled the synthesis of nanocrystalline FDR- LiMnBO_3 and FDR- $\text{LiMnBO}_3/\text{rGO}$ composite. Structural and morphological electrochemical characterization was carried out and electrochemical measurements were performed to study both materials as cathodes for Li-ion batteries.

5.2 FD synthesis of LiMnBO_3 and $\text{LiMnBO}_3/\text{rGO}$ composite

One of the main challenges in the synthesis of nanocrystalline materials by FD route was to find suitable precursors with similar and as low as possible decomposition temperatures. This opened up the possibility to low temperatures reactions and in consequence to smaller crystallite size. For the synthesis of LiMnBO_3 , lithium citrate tetrahydrate $\text{Li}_3(\text{Cit})\cdot 4\text{H}_2\text{O}$ as lithium source, manganese acetate tetrahydrate $\text{Mn}(\text{CH}_3\text{COO})_2\cdot 4\text{H}_2\text{O}$ as manganese source and boric acid H_3BO_3 as boron source were selected after a careful review of available precursors and their thermogravimetric data. $\text{Li}_3(\text{Cit})\cdot 4\text{H}_2\text{O}$ and $\text{Mn}(\text{CH}_3\text{COO})_2\cdot 4\text{H}_2\text{O}$ decompose around 250-320°C and H_3BO_3 around 200°C [130-132]. The expected reaction temperature was around 350°C-400°C.

The XRD patterns of the precursor FD mixture with and without GO after sublimation of the water are shown in Fig.5.2.

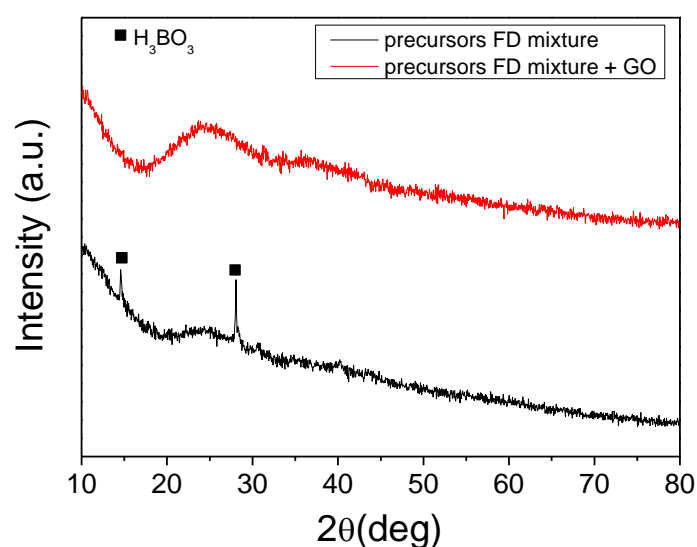


Figure 5.2: XRD patterns of the precursor FD mixture without GO (black), and with GO (red).

The FD mixture containing only the precursors showed two peaks assigned to H_3BO_3 triclinic phase (JCPDS-PDF 00-030-0199). The reflections of the Li and Mn-containing precursors were not visible indicating a good mixing at atomic scale. The FD mixture of the precursors with GO showed an amorphous XRD pattern with a broad hump around 25°. This was an indication for an even better precursors mixing in comparison to the mixture without GO.

In Fig.5.3 the XRD patterns of FDR-LiMnBO₃ and FDR-LiMnBO₃/rGO obtained after heating treatment of the FD mixture were shown.

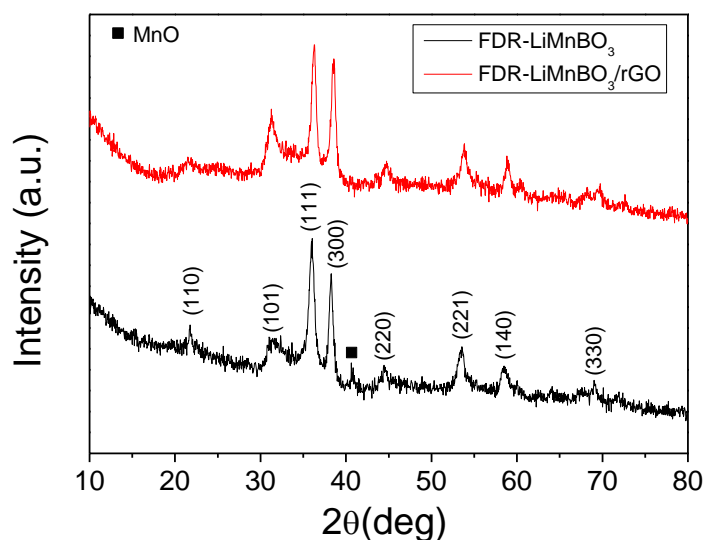


Figure 5.3: XRD pattern of FDR-LiMnBO₃ (black) and FDR-LiMnBO₃/rGO (red)

For both compounds, the diffraction peaks could be indexed with the hexagonal LiMnBO₃ structure (JCPDS-PDF 00-053-0371). The small impurity peak at 40.5° in FDR-LiMnBO₃ was attributed to MnO as decomposition product of manganese acetate in reductive atmosphere [131]. The peak broadening is an indication that both materials were composed of nano-sized crystallites. Williamson-Hall calculation was carried out to quantify their dimension. Results showed an average crystallite size of 10-15 nm for both compounds. Preferred orientation of the crystallite enhanced the peak intensity of the (111) and (300) peaks at $2\theta=35.9$ and 38.1 [57].

In contrast to the standard solid state route [58] which required 800°C to obtain the hexagonal phase, h-LiMnBO₃ was obtained at 300°C and 400°C by FD route with and without GO, respectively. The stabilization of the hexagonal phase at low temperature could be due to the good mixing of the reagents by FD synthesis as already shown before by sol-gel synthesis [57]. The lower temperature obtained using GO was probably due to the additional heat originated by the exothermic reduction reaction from GO to rGO in reducing atmosphere [133].

SEM analysis was carried out to study the morphology of the samples. Micrographs are shown in Fig.5.44. FDR-LiMnBO₃ (Fig.5.4a e Fig.5.4b) was composed of 50-80 nm round-shaped primary particles which formed agglomerates of around 500 nm. In FDR-LiMnBO₃/rGO (Fig.5.4c) the particles were embedded into graphene sheets.

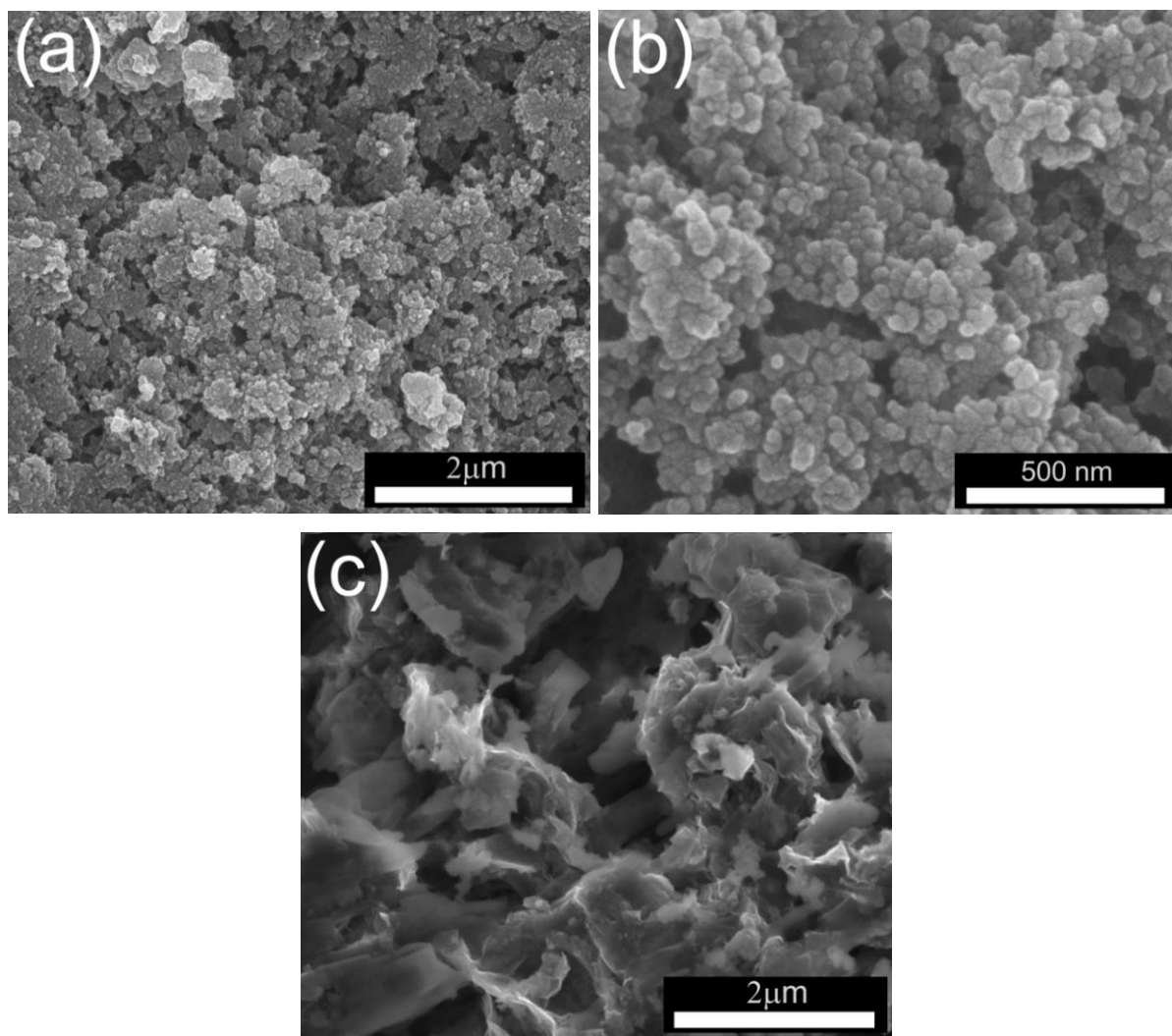


Figure 5.4: SEM micrographs of (a) FDR-LiMnBO₃, (b) higher magnification FDR-LiMnBO₃, and (c) FDR-LiMnBO₃/rGO.

TEM high resolution micrographs are shown in Fig.5.5. FDR-LiMnBO₃ was composed of superimposed crystalline domains in the order of 10 nm in agreement with XRD crystallite size calculations. In FDR-LiMnBO₃/rGO these crystalline domains have similar dimension and were interconnected with rGO sheets.

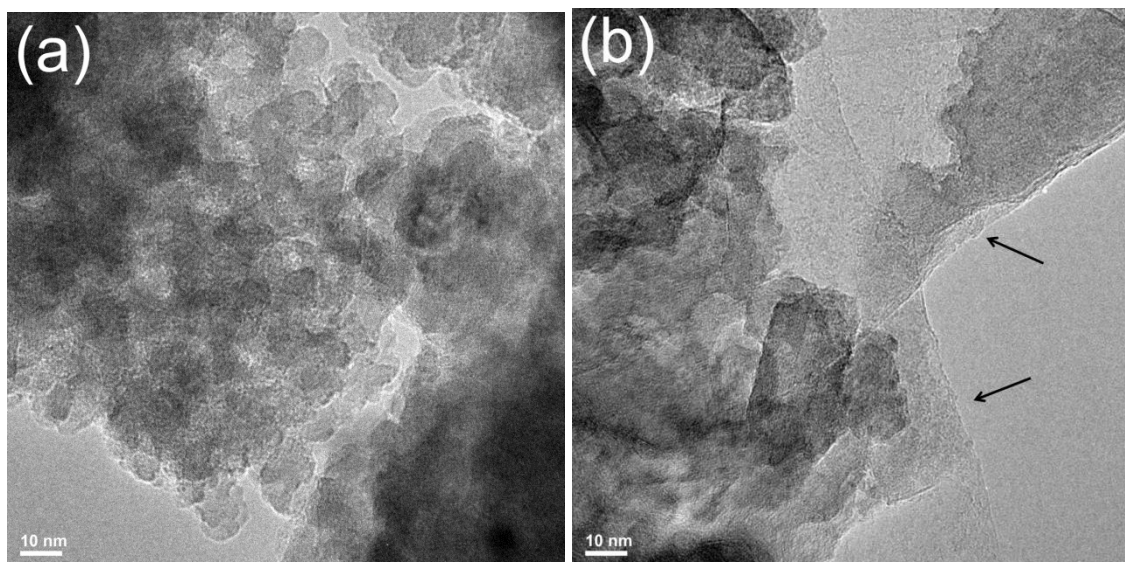


Figure 5.5: TEM micrographs of (a) FDR-LiMnBO₃, (b) FDR-LiMnBO₃/rGO.

The physicochemical characterization carried out showed that the approach to create an *in-situ* nanocrystalline composite material was successful. The good mixing of the precursors with GO was confirmed by XRD. The subsequent simultaneous crystallization of LiMnBO₃ and reduction of GO to rGO allowed creating a conductive network between the metal oxide particles and the rGO sheets as shown by electron microscopy.

Composites with rGO are usually made with a three steps process: 1) synthesis of the metal oxide 2) ball milling with GO and 3) reduction of GO to rGO. This is a very energy and time consuming method. In our case the composite material was obtained in only one-step method. Galvanostatic measurements were carried out to study the electrochemical performance of the synthesized materials and to evaluate the possible differences between them. In Fig.5.6, the 1st cycle voltage profiles of FDR-LiMnBO₃ and FDR-LiMnBO₃/rGO are shown. Both materials showed similar voltage shape, with no defined intercalation voltage plateau. During the first cycle FDR-LiMnBO₃ showed a charge and discharge capacity of 100 Ah/kg and 70 Ah/kg, respectively. These low capacities were probably the result of the low electronic and ionic conductivity of the material which hinders the lithium (de)intercalation. The synthesis of FDR-LiMnBO₃/rGO composite allowed creating a better conductive network and as consequence a charge capacity of 290Ah/kg and a discharge capacity of 120Ah/kg were obtained. Obviously, since the theoretical capacity of the material is 220Ah/kg, side reactions (i.e decomposition due to instability of the charged phase, oxidation of the electrolyte) were occurring during the initial charge which contributed to the total charge capacity.

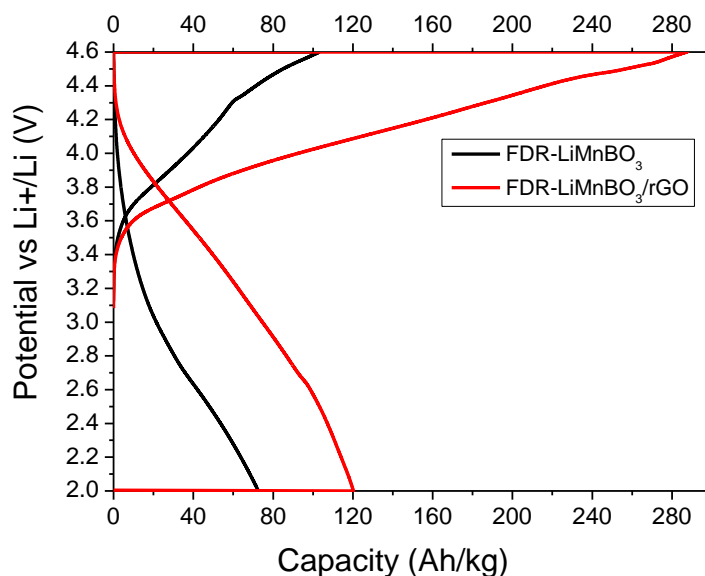


Figure 5.6: Charge and discharge profile for the 1st cycle between 4.6 V and 2.0 V at 10A/ kg of FDR-LiMnBO₃ (black) and FDR-LiMnBO₃/rGO (red).

The voltage profile of FDR-LiMnBO₃/rGO for the 1st, 2nd and 10th cycle is shown in Fig.5.7.

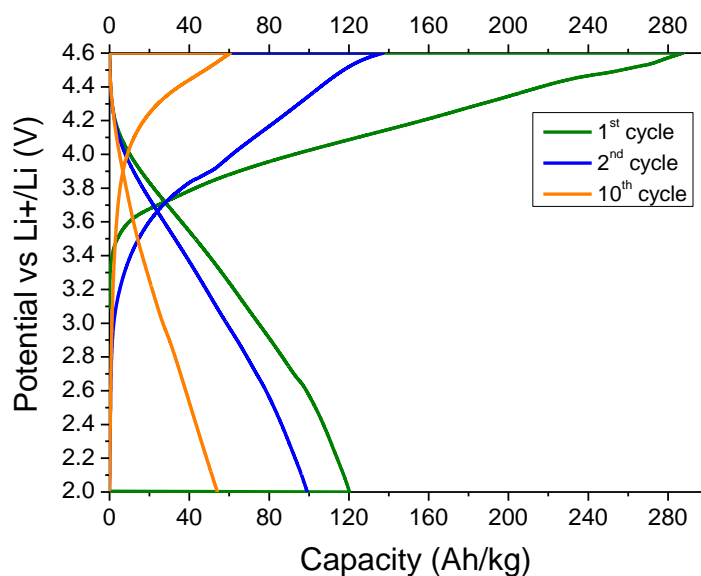


Figure 5.7: 1st, 2nd and 10th cycle between 4.6 V and 2.0 V at 10A/ kg of FDR-LiMnBO₃/rGO.

The lithium (de)intercalation is reversible during the following cycles and the amorphous-like voltage shape was recorded also for the 2nd and 10th cycle. The columbic efficiency increased in the following cycles indicating a lower extent of side reactions; however, the capacity decreased very fast during cycling. The discharge capacity vs cycle number is plotted in Fig.5.8.

The initial increase in discharge capacity recorded for FDR-LiMnBO₃/rGO vanished after a few cycles.

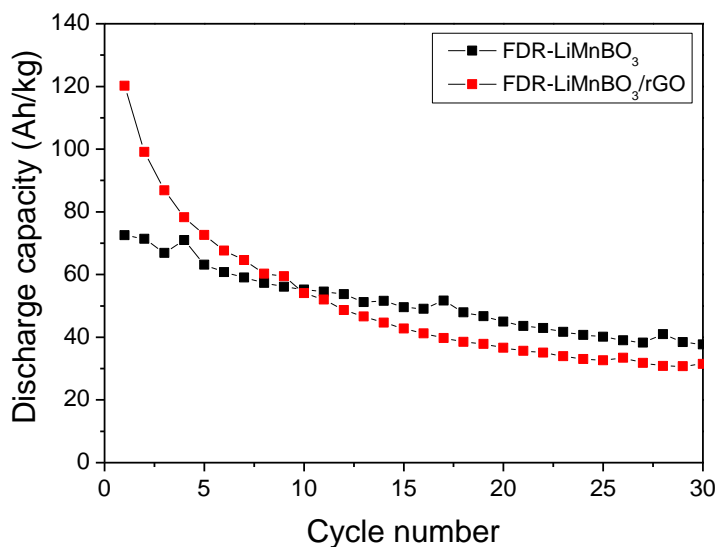


Figure 5.8: Discharge capacity vs cycle number of FDR-LiMnBO₃ (red) and FDR-LiMnBO₃/rGO (black) at 10Ah/kg.

One of the reasons of this strong capacity fading could be associated with amorphization of the material. XRD patterns were recorded after 30 cycles (Fig. 5 .9). Complete amorphization occurred for FDR-LiMnBO₃/rGO, and only two peaks with very low intensity were present between 35° and 40° for FDR-LiMnBO₃.

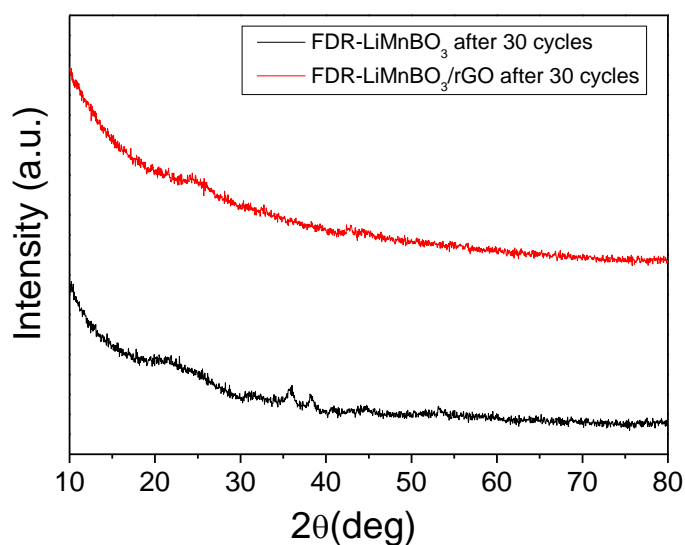


Figure 5.9. XRD patterns of FDR-LiMnBO₃ (black) and FDR-LiMnBO₃/rGO (red) after 30 cycles.

The overall characterization carried out on FDR-LiMnBO₃ and FDR-LiMnBO₃/rGO showed that the FD route can be applied also to borates compounds. Nanocrystalline materials can be obtained by selection of the right precursors. Looking at LiMnBO₃, a conductive network is necessary to obtain good capacities. We have shown that using a one-step synthesis route is possible to obtain a composite material between LiMnBO₃ and rGO. An improvement of 70% in capacity was obtained for FDR-LiMnBO₃/rGO in comparison to bare FDR-LiMnBO₃ in the first discharge. However, a strong capacity fading is still one of the main problems regarding this material. Doping with metal cations such as Co²⁺ or Ni²⁺ and single particle carbon coating could lead to better structural stability and higher capacity retention.

Concluding remarks

The topic of this doctoral thesis was the study of manganese-based cathode materials for Li-ion batteries. Globally, the following results have been achieved:

1) Ca_2MnO_4 was studied for the first time as cathode materials. A calcium extraction by acid treatment was designed to functionalize the surface of the particles and activate it for Li intercalation. The amount of lithium inserted in the acid-treated samples was a function of the amount of calcium extracted. On the basis of the extensive characterization carried out, a new bi-functional crystalline-amorphous structure was proposed. It was composed of an inner Ca_2MnO_4 crystalline bulk core whose aim was to improve the stability, and an outer Ca^{2+} containing $\text{MnO}_2 \cdot \text{H}_2\text{O}$ amorphous shell which gave rise to the electrochemical response. A considerable improvement of the capacity retention was recorded.

2) The freeze drying (FD) technique was applied for the first time to synthesize Li_3MnO_4 . The material synthesized by this synthesis route was very well characterized and compared with Li_3MnO_4 synthesized by a classical solid state reaction. The FD material showed modification in the micro- and nanostructure (particles and crystallite size) which were responsible for the higher capacity recorded during the initial cycles. However, the strong capacity fading over cycling was a trigger for a deeper study on the degradation mechanism. A post-mort analysis was carried out concluding that the material converts to amorphous MnO_2 .

3) Preliminary studies were carried out on LiMnBO_3 . The FD technique was applied for the synthesis of LiMnBO_3 for the first time as well. A nano-crystalline LiMnBO_3 and a $\text{LiMnBO}_3/\text{rGO}$ composite were obtained and characterized. The recorded capacities were very close to the state of the art.

Manganese, as it was shown in this thesis, has a very rich chemistry due to its many oxidation states and its many coordination geometries. However, there are two main drawbacks of Mn-based cathode materials that were tried to be addressed in this thesis: capacity and stability. Taking into account the materials analysed and the techniques used in this work, a lot can still be done to develop better materials and improve their properties.

First of all, the new concept developed for Ca_2MnO_4 can be eventually applied to stabilize other amorphous cathode and anode materials. Secondly, as we have seen in the previous chapters, the possibility to exploit redox couple with manganese oxidation state above Mn^{4+} can occur only in T_d coordination. In this case, a cationic substitution of Mn^{5+} by V^{5+} or P^{5+} with other synthesis techniques (es: USC in O_2) could lead to Li_3MnO_4 stabilization. Anionic

substitution could also be an option, the substitution of O^{2-} by N^{3-} or the incorporation of F^- could lead to the formation of compounds with Mn in high oxidation states. Then, the selection of different precursors for the FD synthesis of $LiMnBO_3$ could allow obtaining an higher reaction temperature and bigger crystallite size that in conjunction with cationic substitution of Mn^{2+} by Co^{2+} or Ni^{2+} could stabilize this material.

In conclusion, this thesis which was focused on almost unexplored materials for battery applications could be considered as pioneering research and an attempt to go beyond the common families of cathode materials. Hopefully, the results presented in this work will motivate also other researchers around the globe to follow this path and start studying new families of cathode materials for Li-ion batteries. This would lead to the development of low cost and environmental friendly materials with higher electrochemical performance.

References

- [1] A.M. Omer, Energy, environment and sustainable development, *Renewable and Sustainable Energy Reviews*, 12 (2008) 2265-2300.
- [2] REN21, *Renewables 2014 10 Year Report : the first decade*, in, 2014.
- [3] E.E. Paul Denholm, Brendan Kirby, and Michael Milligan, *The Role of Energy Storage with Renewable Electricity Generation*, in, 2010.
- [4] Wikipedia - The Free Encyclopedia, in.
- [5] I.E. Agency, *Global EV Outlook: Understanding the Electric Vehicle Landscape to 2020*, in, 2013.
- [6] M.Z. Jacobson, M.A. Delucchi, G. Bazouin, Z.A.F. Bauer, C.C. Heavey, E. Fisher, S.B. Morris, D.J.Y. Piekutowski, T.A. Vencill, T.W. Yeskoo, 100% clean and renewable wind, water, and sunlight (WWS) all-sector energy roadmaps for the 50 United States, *Energy Environ. Sci.*, (2015).
- [7] L.R.F. Allen J. Bard, *ELECTROCHEMICAL METHODS Fundamentals and Applications*, in: I. JOHN WILEY & SONS (Ed.), 2001.
- [8] P.F. Christine Lefrou, Jean-Claude Poignet, *Electrochemistry: The Basics, With Examples*, in: Springer (Ed.), 2012.
- [9] M. Armand, J.M. Tarascon, Building better batteries, *Nature*, 451 (2008) 652-657.
- [10] B.J. Landi, M.J. Ganter, C.D. Cress, R.A. DiLeo, R.P. Raffaele, Carbon nanotubes for lithium ion batteries, *Energy Environ. Sci.*, 2 (2009) 638-654.
- [11] G. Gritzner, G. Kreysa, G.S. Wilson, D. Landolt, V.M.M. Lobo, W. Plieth, M. Sluytersrehabach, K. Tokuda, C.P. Andrieux, Y.A. Chizmadzhev, B.E. Conway, J. Koryta, O.A. Petrij, D. Pletcher, M.J. Weaver, A.J. Arvia, T. Biegler, H.D. Hurwitz, D. Pavlov, G. Horanyi, S.K. Rangarajan, E. Gileadi, S. Trasatti, T. Watanabe, G.A. Wright, W. Paik, C. Gutierrez, D. Simonsson, M.L. Berkem, A.K. Covington, D. Drazic, NOMENCLATURE, SYMBOLS AND DEFINITIONS IN ELECTROCHEMICAL ENGINEERING, *Pure Appl. Chem.*, 65 (1993) 1009-1020.
- [12] G.I. Allen J. Bard, Fritz Scholz, *Electrochemical Dictionary*, in, Springer, 2012.
- [13] G.N. Lewis, F.G. Keyes, THE POTENTIAL OF THE LITHIUM ELECTRODE, *J. Am. Chem. Soc.*, 35 (1913) 340-344.
- [14] K. Brandt, Historical development of secondary lithium batteries, *Solid State Ion.*, 69 (1994) 173-183.
- [15] E. Peled, Film forming reaction at the lithium/electrolyte interface, *J. Power Sources*, 9 (1983) 253-266.
- [16] D. Aurbach, E. Zinigrad, Y. Cohen, H. Teller, A short review of failure mechanisms of lithium metal and lithiated graphite anodes in liquid electrolyte solutions, *Solid State Ion.*, 148 (2002) 405-416.
- [17] J.M. Tarascon, M. Armand, Issues and challenges facing rechargeable lithium batteries, *Nature*, 414 (2001) 359-367.
- [18] S. Basu, C. Zeller, P.J. Flanders, C.D. Fuerst, W.D. Johnson, J.E. Fischer, Synthesis and properties of lithium-graphite intercalation compounds, *Materials Science and Engineering*, 38 (1979) 275-283.
- [19] D. Guerard, A. Herold, Intercalation of lithium into graphite and other carbons, *Carbon*, 13 (1975) 337-345.
- [20] M.S. Whittingham, Lithium batteries and cathode materials, *Chem. Rev.*, 104 (2004) 4271-4301.
- [21] B. Scrosati, Lithium Rocking Chair Batteries: An Old Concept?, *J. Electrochem. Soc.*, 139 (1992) 2776-2781.
- [22] M. Winter, R.J. Brodd, What are batteries, fuel cells, and supercapacitors?, *Chem. Rev.*, 104 (2004) 4245-4269.
- [23] B. Xu, D.N. Qian, Z.Y. Wang, Y.S.L. Meng, Recent progress in cathode materials research for advanced lithium ion batteries, *Materials Science & Engineering R-Reports*, 73 (2012) 51-65.

- [24] M. Winter, J.O. Besenhard, M.E. Spahr, P. Novak, Insertion electrode materials for rechargeable lithium batteries, *Adv. Mater.*, 10 (1998) 725-763.
- [25] Lithium Batteries: Science and Technology., in: G.P. Gholam-Abbas Nazri (Ed.), Springer, 2009.
- [26] T.J. PATEY, Oxide Nanoparticles for Electrodes in Lithium-Ion Batteries, in: Dipl. Verf. -Ing. ETH Zürich, ETH Zurich, Zurich, 2009.
- [27] K. Mizushima, P.C. Jones, P.J. Wiseman, J.B. Goodenough, LIXCOO₂ "(OLESS-THANXLESS-THAN-OR-EQUAL-TO1) - A NEW CATHODE MATERIAL FOR BATTERIES OF HIGH-ENERGY DENSITY, *Mater. Res. Bull.*, 15 (1980) 783-789.
- [28] E. Antolini, LiCoO₂: formation, structure, lithium and oxygen nonstoichiometry, electrochemical behaviour and transport properties, *Solid State Ion.*, 170 (2004) 159-171.
- [29] I. Belharouak, Y.K. Sun, J. Liu, K. Amine, Li(Ni_{1/3}Co_{1/3}Mn_{1/3})O₂ as a suitable cathode for high power applications, *J. Power Sources*, 123 (2003) 247-252.
- [30] N. Yabuuchi, K. Yoshii, S.-T. Myung, I. Nakai, S. Komaba, Detailed Studies of a High-Capacity Electrode Material for Rechargeable Batteries, Li₂MnO₃-LiCo_{1/3}Ni_{1/3}Mn_{1/3}O₂, *J. Am. Chem. Soc.*, 133 (2011) 4404-4419.
- [31] C.S. Johnson, N. Li, C. Lefief, J.T. Vaughey, M.M. Thackeray, Synthesis, Characterization and Electrochemistry of Lithium Battery Electrodes: xLi₂MnO₃center dot(1-x)LiMn_{0.333}Ni_{0.333}Co_{0.333}O₂ (0 <= x <= 0.7), *Chem. Mat.*, 20 (2008) 6095-6106.
- [32] Z. Zhu, L. Zhu, Synthesis of layered cathode material 0.5Li₂MnO₃-0.5LiMn_{1/3}Ni_{1/3}Co_{1/3}O₂ by an improved co-precipitation method for lithium-ion battery, *J. Power Sources*, 256 (2014) 178-182.
- [33] S. Birgisson, K.M.O. Jensen, T.L. Christiansen, J.F. von Bulow, B.B. Iversen, In situ powder X-ray diffraction study of the hydro-thermal formation of LiMn₂O₄ nanocrystallites, *Dalton Transactions*, 43 (2014) 15075-15084.
- [34] Batteries for Sustainability, in: R.J. Brodd (Ed.), Springer, 2013.
- [35] M.M. Thackeray, W.I.F. David, P.G. Bruce, J.B. Goodenough, Lithium insertion into manganese spinels, *Mater. Res. Bull.*, 18 (1983) 461-472.
- [36] H.C. Le, N.D. Nguyen, S. Brutti, B. Scrosati, Synthesis, characterization and electrochemical properties of 4.8 V LiNi_{0.5}Mn_{1.5}O₄ cathode material in lithium-ion batteries, *Electrochim. Acta*, 55 (2010) 5110-5116.
- [37] N. Amdouni, K. Zaghib, F. Gendron, A. Mauger, C.M. Julien, Structure and insertion properties of disordered and ordered LiNi_{0.5}Mn_{1.5}O₄ spinels prepared by wet chemistry, *Ionics*, 12 (2006) 117-126.
- [38] Nanotechnology for Lithium-Ion Batteries, in: I.D. Yaser Abu-Lebdeh (Ed.), Springer, 2013.
- [39] V. Etacheri, R. Marom, R. Elazari, G. Salitra, D. Aurbach, Challenges in the development of advanced Li-ion batteries: a review, *Energy Environ. Sci.*, 4 (2011) 3243-3262.
- [40] R. Marom, S.F. Amalraj, N. Leifer, D. Jacob, D. Aurbach, A review of advanced and practical lithium battery materials, *J. Mater. Chem.*, 21 (2011) 9938-9954.
- [41] A.K. Padhi, K.S. Nanjundaswamy, J.B. Goodenough, Phospho-olivines as positive-electrode materials for rechargeable lithium batteries, *J. Electrochem. Soc.*, 144 (1997) 1188-1194.
- [42] V. Aravindan, J. Gnanaraj, Y.S. Lee, S. Madhavi, LiMnPO₄ - A next generation cathode material for lithium-ion batteries, *J. Mater. Chem. A*, 1 (2013) 3518-3539.
- [43] J.B. Goodenough, Y. Kim, Challenges for Rechargeable Li Batteries, *Chem. Mat.*, 22 (2010) 587-603.
- [44] C.K. Chan, H. Peng, G. Liu, K. McIlwrath, X.F. Zhang, R.A. Huggins, Y. Cui, High-performance lithium battery anodes using silicon nanowires, *Nat Nano*, 3 (2008) 31-35.
- [45] L. Kavan, J. Prochazka, T.M. Spitler, M. Kalbac, M.T. Zkalova, T. Drezen, M. Gratzel, Li insertion into Li₄Ti₅O₁₂ p(Spinel) - Charge capability vs. particle size in thin-film electrodes, *J. Electrochem. Soc.*, 150 (2003) A1000-A1007.
- [46] H. Li, X. Liu, T. Zhai, D. Li, H. Zhou, Li₃VO₄: A Promising Insertion Anode Material for Lithium-Ion Batteries, *Adv. Energy Mater.*, 3 (2013) 428-432.
- [47] A. Lewandowski, A. Świdarska-Mocek, Ionic liquids as electrolytes for Li-ion batteries—An overview of electrochemical studies, *J. Power Sources*, 194 (2009) 601-609.

- [48] P. Knauth, Inorganic solid Li ion conductors: An overview, *Solid State Ion.*, 180 (2009) 911-916.
- [49] A.H. Whitehead, M. Schreiber, Current Collectors for Positive Electrodes of Lithium-Based Batteries, *J. Electrochem. Soc.*, 152 (2005) A2105-A2113.
- [50] S.-T. Myung, Y. Hitoshi, Y.-K. Sun, Electrochemical behavior and passivation of current collectors in lithium-ion batteries, *J. Mater. Chem.*, 21 (2011) 9891-9911.
- [51] S.S. Zhang, A review on the separators of liquid electrolyte Li-ion batteries, *J. Power Sources*, 164 (2007) 351-364.
- [52] Y. Idemoto, T. Mochizuki, K. Ui, N. Koura, Properties, crystal structure, and performance of α -LiMnO₂ as cathode material for Li secondary batteries, *J. Electrochem. Soc.*, 153 (2006) A418-A424.
- [53] H. Xia, Z.T. Luo, J.P. Xie, Nanostructured LiMn₂O₄ and their composites as high-performance cathodes for lithium-ion batteries, *Progress in Natural Science-Materials International*, 22 (2012) 572-584.
- [54] Q. Zhang, J. Mei, X. Wang, J. Guo, F. Tang, W. Lu, Facile synthesis of spherical spinel LiMn₂O₄ nanoparticles via solution combustion synthesis by controlling calcinating temperature, *J. Alloy. Compd.*, 617 (2014) 326-331.
- [55] S.-M. Oh, S.W. Oh, S.-T. Myung, S.-M. Lee, Y.-K. Sun, The effects of calcination temperature on the electrochemical performance of LiMnPO₄ prepared by ultrasonic spray pyrolysis, *J. Alloy. Compd.*, 506 (2010) 372-376.
- [56] R.J. Gummow, Y. He, Recent progress in the development of Li₂MnSiO₄ cathode materials, *J. Power Sources*, 253 (2014) 315-331.
- [57] S. Afyon, D. Kundu, F. Krumeich, R. Nesper, Nano LiMnBO₃, a high-capacity cathode material for Li-ion batteries, *J. Power Sources*, 224 (2013) 145-151.
- [58] L. Chen, Y.M. Zhao, X.N. An, J.M. Liu, Y.Z. Dong, Y.H. Chen, Q. Kuang, Structure and electrochemical properties of LiMnBO₃ as a new cathode material for lithium-ion batteries, *J. Alloy. Compd.*, 494 (2010) 415-419.
- [59] D.H. Jang, Y.J. Shin, S.M. Oh, Dissolution of spinel oxides and capacity losses in 4V Li/Li_xMn₂O₄ cells, *J. Electrochem. Soc.*, 143 (1996) 2204-2211.
- [60] A. Yamada, Lattice Instability in Li(Li_xMn_{2-x})O₄, *J. Solid State Chem.*, 122 (1996) 160-165.
- [61] X. Li, Y. Xu, C. Wang, Suppression of Jahn–Teller distortion of spinel LiMn₂O₄ cathode, *J. Alloy. Compd.*, 479 (2009) 310-313.
- [62] K.Y. Chung, C.W. Ryu, K.B. Kim, Onset mechanism of jahn-teller distortion in 4 V LiMn₂O₄ and its suppression by Li_{0.05}Mn_{1.95}O₄ (M = Co, Ni) coating, *J. Electrochem. Soc.*, 152 (2005) A791-A795.
- [63] R.G. BURNS, MINERALOGICAL APPLICATIONS OF CRYSTAL FIELD THEORY, in, CAMBRIDGE UNIVERSITY PRESS, 1993.
- [64] E.A.K. James E. Huheey, Richard L. Keiter, Inorganic Chemistry, in, Harper Collins College Publisher.
- [65] Q. Liu, Y.X. Li, Z.L. Hu, D.L. Mao, C.K. Chang, F.Q. Huang, One-step hydrothermal routine for pure-phased orthorhombic LiMnO₂ for Li ion battery application, *Electrochim. Acta*, 53 (2008) 7298-7302.
- [66] F. Cheng, J. Zhao, W. Song, C. Li, H. Ma, J. Chen, P. Shen, Facile Controlled Synthesis of MnO₂ Nanostructures of Novel Shapes and Their Application in Batteries, *Inorg. Chem.*, 45 (2006) 2038-2044.
- [67] J.A. Saint, M.M. Doeff, J. Reed, Synthesis and electrochemistry of Li₃MnO₄: Mn in the +5 oxidation state, *J. Power Sources*, 172 (2007) 189-197.
- [68] D.M. Sherman, THE ELECTRONIC-STRUCTURES OF MANGANESE OXIDE MINERALS, *Am. Miner.*, 69 (1984) 788-799.
- [69] J.C. Kim, C.J. Moore, B. Kang, G. Hautier, A. Jain, G. Ceder, Synthesis and Electrochemical Properties of Monoclinic LiMnBO₃ as a Li Intercalation Material, *J. Electrochem. Soc.*, 158 (2011) A309-A315.
- [70] A. Sasmal, S. Saha, C.J. Gomez-Garcia, C. Desplanches, E. Garribba, A. Bauza, A. Frontera, R. Scott, R.J. Butcher, S. Mitra, Reversible switching of the electronic ground state in a pentacoordinated Cu(II) complex, *Chemical Communications*, 49 (2013) 7806-7808.

- [71] R. Robert, D. Logvinovich, M.H. Aguirre, S.G. Ebbinghaus, L. Bocher, P. Tomes, A. Weidenkaff, Crystal structure, morphology and physical properties of $\text{LaCo}_{1-x}\text{Ti}_x\text{O}_3$ \pm δ perovskites prepared by a citric acid assisted soft chemistry synthesis, *Acta Materialia*, 58 (2010) 680-691.
- [72] I.D. Fawcett, J.E. Sunstrom, M. Greenblatt, M. Croft, K.V. Ramanujachary, Structure, magnetism, and properties of Ruddlesden-Popper calcium manganates prepared from citrate gels, *Chem. Mat.*, 10 (1998) 3643-3651.
- [73] E. Krupicka, A. Reller, A. Weidenkaff, Morphology of nanoscaled LaMO_3 -particles (M=Mn, Fe, Co, Ni) derived by citrate precursors in aqueous and alcoholic solvents, *Crystal Engineering*, 5 (2002) 195-202.
- [74] L. Bocher, M.H. Aguirre, R. Robert, D. Logvinovich, S. Bakardjieva, J. Hejtmanek, A. Weidenkaff, High-temperature stability, structure and thermoelectric properties of $\text{CaMn}_{1-x}\text{Nb}_x\text{O}_3$ phases, *Acta Materialia*, 57 (2009) 5667-5680.
- [75] H.Y. Lee, J.B. Goodenough, Supercapacitor behavior with KCl electrolyte, *J. Solid State Chem.*, 144 (1999) 220-223.
- [76] F. Leroux, L.F. Nazar, 3-volt manganese dioxide: the amorphous alternative, *Solid State Ion.*, 100 (1997) 103-113.
- [77] A.A. Andriiko, A.Y. Shpak, Y.O. Andriyko, J.R. Garcia, S.A. Khainakov, N.Y. Vlasenko, Formation of spinel structured compounds in the lithium permanganate thermal decomposition, *J. Solid State Electrochem.*, 16 (2012) 1993-1998.
- [78] E.E. McCabe, C. Greaves, Synthesis and structural and magnetic characterization of mixed manganese-copper $n=1$ Ruddlesden-Popper phases, *Chem. Mat.*, 18 (2006) 5774-5781.
- [79] K.H. Lee, S.W. Kim, H. Ohta, K. Koumoto, Thermoelectric properties of layered perovskite-type $(\text{Sr}_{1-x}\text{Ca}_x)_3(\text{Ti}_{1-y}\text{Nb}_y)_2\text{O}_7$, *J. Appl. Phys.*, 101 (2007).
- [80] M.D. Carvalho, R.P. Borges, A.V. Girao, M.M. Cruz, M.E.M. Jorge, G. Bonfait, P. Dluzewski, M. Godinho, Electron doping of $\text{Ca}_4\text{Mn}_3\text{O}_{10}$ induced by vanadium substitution, *Chem. Mat.*, 17 (2005) 4852-4857.
- [81] K. Toda, S. Kurita, M. Sato, New layered perovskite compounds, LiLaTiO_4 and LiEuTiO_4 , *Journal of the Ceramic Society of Japan*, 104 (1996) 140-142.
- [82] K. Toda, M. Takahashi, T. Teranishi, Z.G. Ye, M. Sato, Y. Hinatsu, Synthesis and structure determination of reduced tantalates, $\text{Li}_2\text{LaTa}_2\text{O}_7$, $\text{Li}_2\text{Ca}_2\text{Ta}_3\text{O}_{10}$ and $\text{Na}_2\text{Ca}_2\text{Ta}_3\text{O}_{10}$, with a layered perovskite structure, *J. Mater. Chem.*, 9 (1999) 799-803.
- [83] C.R. Michel, R. Amigo, N. Casan-Pastor, Dramatic change in magnetic properties of manganates $\text{Ca}_{2-x}\text{Ln}_x\text{MnO}_4$ by low-temperature electrochemical oxidation in fused nitrates, *Chem. Mat.*, 11 (1999) 195-197.
- [84] S. Nishimoto, M. Matsuda, M. Miyake, Novel protonated and hydrated $n=1$ Ruddlesden-Popper phases, $\text{H}_x\text{Na}_{1-x}\text{LaTiO}_4 \cdot y\text{H}_2\text{O}$, formed by ion-exchange/intercalation reaction, *J. Solid State Chem.*, 178 (2005) 811-818.
- [85] S. Lin, Z. Huang, Y. Sun, X. Wang, R. Tang, S. Ma, X. Yang, Synthesis of $\text{Ca}_{1+x}\text{Mn}_x\text{O}_{1+3x}$ ($x = 1, 2, 3$) compounds with the Ruddlesden-Popper structures and extraction of their interlayer Ca^{2+} ions, *Journal of Beijing Normal University (Natural Science)*, 45 (2009) 370-374.
- [86] D.S. Alfaruq, M.H. Aguirre, E.H. Otal, S. Populoh, L. Karvonen, S. Yoon, Y. Lu, G. Deng, S.G. Ebbinghaus, A. Weidenkaff, Crystal growth and thermoelectric properties of $\text{CaMn}_{0.98}\text{Nb}_{0.02}\text{O}_{3-\delta}$, *J. Cryst. Growth*, 377 (2013) 170-177.
- [87] A. Nemudry, P. Weiss, I. Gainutdinov, V. Boldyrev, R. Schollhorn, Room temperature electrochemical redox reactions of the defect perovskite $\text{SrFeO}_{2.5+x}$, *Chem. Mat.*, 10 (1998) 2403-2411.
- [88] L. Karvonen, S.H. Yoon, P. Hug, H. Yamauchi, A. Weidenkaff, M. Karppinen, The $n=3$ member of the $\text{SrCoO}_{(3n-1)/n}$ series of layered oxygen-defect perovskites, *Mater. Res. Bull.*, 46 (2011) 1340-1345.
- [89] K.R. Poeppelmeier, M.E. Leonowicz, J.M. Longo, $\text{CaMnO}_{2.5}$ AND $\text{Ca}_2\text{MnO}_{3.5}$ - NEW OXYGEN-DEFECT PEROVSKITE-TYPE OXIDES, *J. Solid State Chem.*, 44 (1982) 89-98.

- [90] R.N. Reddy, R.G. Reddy, Synthesis and electrochemical characterization of amorphous MnO₂ electrochemical capacitor electrode material, *J. Power Sources*, 132 (2004) 315-320.
- [91] K. Ozawa, *Lithium Ion Rechargeable Batteries: Materials, Technology, and New Applications*, WILEY-VCH Verlag GmbH & Co, 2009.
- [92] C.H. Jiang, E. Hosono, H.S. Zhou, Nanomaterials for lithium ion batteries, *Nano Today*, 1 (2006) 28-33.
- [93] M. Galceran, M.C. Pujol, M. Aguiló, F. Diaz, Sol-gel modified Pechini method for obtaining nanocrystalline KRE(WO₄)₂ (RE = Gd and Yb), *J. Sol-Gel Sci. Technol.*, 42 (2007) 79-88.
- [94] R. Baddour-Hadjean, J.P. Pereira-Ramos, Raman Microspectrometry Applied to the Study of Electrode Materials for Lithium Batteries, *Chem. Rev.*, 110 (2010) 1278-1319.
- [95] G. Meyer, R. Hoppe, THERMAL-BEHAVIOR OF LiMnO₄. I. ALPHA-LiMnO₄ AND BETA-LiMnO₄, *Zeitschrift Fur Anorganische Und Allgemeine Chemie*, 424 (1976) 249-256.
- [96] O.A. Shlyakhtin, Y.S. Yoon, S.H. Choi, Y.J. Oh, Freeze drying synthesis of LiNi_{0.5}Mn_{0.5}O₂ cathode materials, *Electrochim. Acta*, 50 (2004) 505-509.
- [97] G. Sudant, E. Baudrin, B. Dunn, J.M. Tarascon, Synthesis and electrochemical properties of vanadium oxide aerogels prepared by a freeze-drying process, *J. Electrochem. Soc.*, 151 (2004) A666-A671.
- [98] Y.Q. Qiao, X.L. Wang, Y.J. Mai, X.H. Xia, J. Zhang, C.D. Gu, J.P. Tu, Freeze-drying synthesis of Li₃V₂(PO₄)₃/C cathode material for lithium-ion batteries, *J. Alloy. Compd.*, 536 (2012) 132-137.
- [99] O.A. Shlyakhtin, Y.J. Oh, Inorganic cryogels for energy saving and conversion, *J. Electroceram.*, 23 (2009) 452-461.
- [100] T. Le Mercier, J. Gaubicher, E. Bermejo, Y. Chabre, M. Querton, Morphology and electrochemical behavior of an ultrafine LiMn₂O₄ powder obtained by a new route, from freeze-dried precursors, *J. Mater. Chem.*, 9 (1999) 567-570.
- [101] H.S. Zhou, D.L. Li, M. Hibino, I. Honma, A self-ordered, crystalline-glass, mesoporous nanocomposite for use as a lithium-based storage device with both high power and high energy densities, *Angew. Chem.-Int. Edit.*, 44 (2005) 797-802.
- [102] M. Zhao, Y. Fu, N. Xu, G.R. Li, M.T. Wu, X.P. Gao, High performance LiMnPO₄/C prepared by a crystallite size control method, *J. Mater. Chem. A*, 2 (2014) 15070-15077.
- [103] W.P. Kilroy, S. Dallek, J. Zaykoski, Synthesis and characterization of metastable Li-Mn-O spinels from Mn(V), *J. Power Sources*, 105 (2002) 75-81.
- [104] C.N.R. Rao, D.D. Sarma, S. Vasudevan, M.S. Hegde, STUDY OF TRANSITION-METAL OXIDES BY PHOTOELECTRON-SPECTROSCOPY, *Proc. R. Soc. London Ser. A-Math. Phys. Eng. Sci.*, 367 (1979) 239-252.
- [105] M. Oku, X-RAY PHOTOELECTRON-SPECTRA OF KMNO₄ AND K₂MNO₄ FRACTURED IN-SITU, *J. Electron Spectrosc. Relat. Phenom.*, 74 (1995) 135-148.
- [106] S. Malmgren, K. Ciosek, M. Hahlin, T. Gustafsson, M. Gorgoi, H. Rensmo, K. Edström, Comparing anode and cathode electrode/electrolyte interface composition and morphology using soft and hard X-ray photoelectron spectroscopy, *Electrochim. Acta*, 97 (2013) 23-32.
- [107] K.P.C. Yao, D.G. Kwabi, R.A. Quinlan, A.N. Mansour, A. Grimaud, Y.-L. Lee, Y.-C. Lu, Y. Shao-Horn, Thermal Stability of Li₂O₂ and Li₂O for Li-Air Batteries: In Situ XRD and XPS Studies, *J. Electrochem. Soc.*, 160 (2013) A824-A831.
- [108] P. Verma, P. Maire, P. Novák, A review of the features and analyses of the solid electrolyte interphase in Li-ion batteries, *Electrochim. Acta*, 55 (2010) 6332-6341.
- [109] Y. Shao, G. Yin, J. Zhang, Y. Gao, Comparative investigation of the resistance to electrochemical oxidation of carbon black and carbon nanotubes in aqueous sulfuric acid solution, *Electrochim. Acta*, 51 (2006) 5853-5857.
- [110] K. Edström, T. Gustafsson, J.O. Thomas, The cathode–electrolyte interface in the Li-ion battery, *Electrochim. Acta*, 50 (2004) 397-403.
- [111] Gonzalez.F, W.P. Griffith, TRANSITION-METAL TETRA-OXO-COMPLEXES AND THEIR VIBRATIONAL-SPECTRA, *J. Chem. Soc.-Dalton Trans.*, (1972) 1416-&.

- [112] R.J. Smith, Y.R. Shen, K.L. Bray, The effect of pressure on vibrational modes in Li₃PO₄, *J. Phys.-Condes. Matter*, 14 (2002) 461-469.
- [113] T. Jawhari, A. Roid, J. Casado, Raman spectroscopic characterization of some commercially available carbon black materials, *Carbon*, 33 (1995) 1561-1565.
- [114] D.Y.W. Yu, K. Yanagida, Y. Kato, H. Nakamura, Electrochemical Activities in Li₂MnO₃, *J. Electrochem. Soc.*, 156 (2009) A417-A424.
- [115] S.S. Zhang, K. Xu, T.R. Jow, Understanding formation of solid electrolyte interface film on LiMn₂O₄ electrode, *J. Electrochem. Soc.*, 149 (2002) A1521-A1526.
- [116] Z.Q. Peng, S.A. Freunberger, L.J. Hardwick, Y.H. Chen, V. Giordani, F. Barde, P. Novak, D. Graham, J.M. Tarascon, P.G. Bruce, Oxygen Reactions in a Non-Aqueous Li⁺ Electrolyte, *Angew. Chem.-Int. Edit.*, 50 (2011) 6351-6355.
- [117] X. Jun John, Y. Hui, J. Gaurav, Y. Jingsi, Amorphous manganese oxide remains amorphous upon lithium intercalation and cycling, *Electrochemistry Communications*, 6 (2004) 892-897.
- [118] J.J. Xu, S. Passerini, B.B. Owens, W.H. Smyrl, Processing and properties of amorphous manganese dioxide formed by sol-gel procedures, in: G.A. Nazri, C. Julien, A. Rougier (Eds.) *Solid State Ionics V*, Materials Research Society, Warrendale, 1999, pp. 119-124.
- [119] L. Wu, D. Bresser, D. Buchholz, S. Passerini, Nanocrystalline TiO₂(B) as Anode Material for Sodium-Ion Batteries, *J. Electrochem. Soc.*, 162 (2015) A3052-A3058.
- [120] J.A. Chang, M. Vithal, I.C. Baek, S.I. Seok, Morphological and phase evolution of TiO₂ nanocrystals prepared from peroxotitanate complex aqueous solution: Influence of acetic acid, *J. Solid State Chem.*, 182 (2009) 749-756.
- [121] J. Liu, Q. Pan, MnO/C Nanocomposites as High Capacity Anode Materials for Li-Ion Batteries, *Electrochem. Solid-State Lett.*, 13 (2010) A139-A142.
- [122] W.-J. Zhang, Structure and performance of LiFePO₄ cathode materials: A review, *J. Power Sources*, 196 (2011) 2962-2970.
- [123] K.J. Lee, D.W. Kim, H.S. Hong, Preparation and Characterizations of Lithium Iron Borate Nano-sized Powders via Aerosol and Thermal Process, *Curr. Nanosci.*, 10 (2014) 168-170.
- [124] B.C. Melot, J.M. Tarascon, Design and Preparation of Materials for Advanced Electrochemical Storage, *Accounts Chem. Res.*, 46 (2013) 1226-1238.
- [125] V. Legagneur, Y. An, A. Mosbah, R. Portal, A.L. La Salle, A. Verbaere, D. Guyomard, Y. Piffard, LiMBO₃ (M = Mn, Fe, Co): synthesis, crystal structure and lithium deinsertion/insertion properties, *Solid State Ion.*, 139 (2001) 37-46.
- [126] O.S. Bondareva, M.A. Simonov, Y.K. Egorovtismenko, N.V. Belov, CRYSTAL-STRUCTURE OF LiZnBO₃ AND LiMnBO₃, *Kristallografiya*, 23 (1978) 487-490.
- [127] J. Molenda, A. Kulka, A. Milewska, W. Zajac, K. Swierczek, Structural, Transport and Electrochemical Properties of LiFePO₄ Substituted in Lithium and Iron Sublattices (Al, Zr, W, Mn, Co and Ni), *Materials*, 6 (2013) 1656-1687.
- [128] T. Ma, A. Muslim, Z. Su, Microwave synthesis and electrochemical properties of lithium manganese borate as cathode for lithium ion batteries, *J. Power Sources*, 282 (2015) 95-99.
- [129] Y.S. Lee, H. Lee, Improved lithium storage capacities of LiMnBO₃/C via simple high-energy milling, *Mater. Lett.*, 132 (2014) 401-404.
- [130] G.E. Tobon-Zapata, E.G. Ferrer, S.B. Etcheverry, E.J. Baran, Thermal behaviour of pharmacologically active lithium compounds, *J. Therm. Anal.*, 61 (2000) 29-35.
- [131] E.M. Diefallah, KINETIC-ANALYSIS OF THERMAL-DECOMPOSITION REACTIONS .6. THERMAL-DECOMPOSITION OF MANGANESE(II) ACETATE TETRAHYDRATE, *Thermochim. Acta*, 202 (1992) 1-16.
- [132] F. Sevim, F. Demir, M. Bilen, H. Okur, Kinetic analysis of thermal decomposition of boric acid from thermogravimetric data, *Korean J. Chem. Eng.*, 23 (2006) 736-740.
- [133] Z.L. Wang, D. Xu, Y. Huang, Z. Wu, L.M. Wang, X.B. Zhang, Facile, mild and fast thermal-decomposition reduction of graphene oxide in air and its application in high-performance lithium batteries, *Chemical Communications*, 48 (2012) 976-978.

Additional declaration

Chapter 2, chapter 3 and subchapter 4.1, 4.2 and 4.3 are based on the following published papers:

Y. Surace, M. Simoes, J. Eilertsen, L. Karvonen, S. Pokrant, A. Weidenkaff, Functionalization of $\text{Ca}_2\text{MnO}_{4-\text{delta}}$ by controlled calcium extraction: Activation for electrochemical Li intercalation, *Solid State Ion.*, 266 (2014) 36-43.

Y. Surace, M. Simões, L. Karvonen, S. Yoon, S. Pokrant, A. Weidenkaff, Freeze drying synthesis of Li_3MnO_4 cathode material for Li-ion batteries: A physico-electrochemical study, *J. Alloy. Compd.*, 644 (2015) 297-303.

Y. Surace, M. Simoes, J. Eilertsen, L. Karvonen, S. Pokrant, A. Weidenkaff, Activation of nano- Ca_2MnO_4 for electrochemical lithium intercalation, *MRS Spring 2015 proceeding*, Vol 1805/2015.

And on the following submitted paper:

Y. Surace, M. Simões, S. Pokrant, A. Weidenkaff, Capacity fading in Li_3MnO_4 : a post-mortem analysis.

Dübendorf, 13/11/2015

Yuri Surace

Curriculum Vitae

Yuri Surace

Nationality: Italian

Date of birth: 31.07.1988



Education

- 09.2012-10.2015 **Ph.D candidate**
Swiss Federal Labs for Materials Science and Technology (EMPA) (CH) and University of Stuttgart (Germany)
Thesis title: Manganese-based cathode materials for Li-ion batteries
Thesis supervisor: Prof. Dr. Anke Weidenkaff (University of Stuttgart) and Dr. Simone Pokrant (EMPA)
- 10.2009-05.2012 **Master degree in Materials Science and Engineering**
University of Calabria (Italy) with a final vote 110/110 with honors.
Thesis title: New luminescent platinum (II) complexes with tetradentate ligands.
Thesis supervisor: Prof. Dr. Mauro Ghedini and Dr. Nicolas Godbert (University of Calabria), Dr. J.A.Gareth Williams (University of Durham)
- 10.2006-12.2009 **Bachelor degree in Materials Science**
University of Calabria (Italy) with a final vote 110/110 with honors.
Thesis title: New electrochromic materials with cyclopentadienyl structure
Thesis supervisor: Prof. Dr. G.Chidichimo and Dr.Lucia Veltri (University of Calabria)
- 09.2001-07.2006 **High School Science Diploma**
Liceo scientifico "Michele Guerrisi" (Italy) with a final vote 94/100.

Publications

Y. Surace, M. Simoes, J. Eilertsen, L. Karvonen, S. Pokrant, A. Weidenkaff, Functionalization of $\text{Ca}_2\text{MnO}_{4-\delta}$ by controlled calcium extraction: Activation for electrochemical Li intercalation, *Solid State Ion.*, 266 (2014) 36-43.

Y. Surace, M. Simões, L. Karvonen, S. Yoon, S. Pokrant, A. Weidenkaff, Freeze drying synthesis of Li_3MnO_4 cathode material for Li-ion batteries: A physico-electrochemical study, *J. Alloy. Compd.*, 644 (2015) 297-303.

Y. Surace, M. Simoes, J. Eilertsen, L. Karvonen, S. Pokrant, A. Weidenkaff, Activation of nano- Ca_2MnO_4 for electrochemical lithium intercalation, MRS Spring 2015 proceeding, Vol 1805/2015.

Y. Surace, M. Simões, S. Pokrant, A. Weidenkaff, Capacity fading in Li_3MnO_4 : a post-mortem analysis, *submitted*

M. Simões, **Y. Surace**, S. Yoon, C. Battaglia, S. Pokrant, A. Weidenkaff, Hydrothermal vanadium manganese oxides: Anode and cathode materials for lithium-ion batteries, *J. Power Sources*, 291 (2015) 66-74.

J. Eilertsen, **Y. Surace**, S. Balog, L. Sagarna, G. Rogl, J. Horiky, M. Trottmann, P. Rogl, M.A. Subramanian, A. Weidenkaff, From Occupied Voids to Nanoprecipitates: Synthesis of Skutterudite Nanocomposites in situ, *Zeitschrift für anorganische und allgemeine Chemie*, 641 (2015) 1495-1502.

Contributions to conferences

Materials Research Society (MRS) Spring meeting, San Francisco (CA), United States, April 6-10, 2015 – Poster contribution

65th Annual Meeting of International Society of Electrochemistry (ISE), Lausanne, Switzerland, August 31-September 5, 2014 – Oral contribution

Gordon Research Conference: Batteries, Ventura (CA), United States, March 9-14, 2014 – Poster Contribution

European Material Research Society (E-MRS) Spring Meeting, Strasburg, France, May 27-31, 2013 – Poster Contribution

Workshop

Powder Diffraction School (Modern Synchrotron Methods), PSI (Paul Scherrer institute), Villigen, Switzerland, July 1-4, 2014